# BIODEGRADABLE, THERMALLY RESPONSIVE HYDROGELS FOR MYOCARDIAL INFARCTION TREATMENT

by

**Yang Zhu**

B.S. Material Science, Zhejiang University, 2009

M.S. Polymer Materials, Zhejiang University, 2012

Submitted to the Graduate Faculty of

Swanson School of Engineering in partial fulfillment

of the requirements for the degree of

Doctor of Philosophy

University of Pittsburgh

2017

UNIVERSITY OF PITTSBURGH

SWANSON SCHOOL OF ENGINEERING

This dissertation was presented

by

Yang Zhu

It was defended on

February 20, 2017

and approved by

Eric J. Beckman, PhD, Professor, Department of Chemical and Petroleum Engineering

Kang Kim, PhD, Associate Professor, Departments of Medicine and Bioengineering

Bing Wang, MD, PhD, Associate Professor, Department of Orthopaedic Surgery

Kimimasa Tobita, MD, Professor, Department of Developmental Biology

Dissertation Director: William R. Wagner, PhD, Professor, Departments of Surgery, Bioengineering, and Chemical and Petroleum Engineering

**BIODEGRADABLE, THERMALLY RESPONSIVE INJECTABLE HYDROGELS FOR MYOCARDIAL INFARCTION TREATMENT**

Yang Zhu, PhD

University of Pittsburgh, 2017

Myocardial infarction (MI) is one of the leading causes of human mortality and morbidity. Aimed at preventing post-MI pathological left ventricular remodeling, which leads to end-stage heart failure, intramyocardial biomaterial injection was developed and has been rapidly advancing as a strategy to provide mechanical support to the ventricular wall. Various material candidates have been evaluated in clinical and preclinical trials and have presented promising therapeutic outcomes. This growing body of research has stimulated efforts to optimize material properties, identify key mechanistic factors, and implement safer, more adaptable delivery methods.

We previously invented a series of poly(N-isopropylacrylamide) (polyNIPAAm) based thermally responsive injectable hydrogels which could become hydrophilic and be absorbed in vivo as labile hydrophobic polyester side chains are removed. With advantageous mechanical properties, these hydrogels has shown beneficial effects in small and large animal models of MI. At the same time, there is considerable room for improvement in material design. Hydrogel degradation rates could not be precisely manipulated across a wide range. High viscosity and sol-gel transition of hydrogel solutions below body temperature prohibited catheter based delivery.

The bioactivity of the synthetic hydrogels was low, not specifically incorporating activity designed to mitigate adverse responses of MI and the injected hydrogel itself.

Modifications were made on the previous hydrogel platform. We employed the concept of "acid-catalyzed degradation" documented in polyester based scaffold materials and developed an innovative strategy of tailoring the degradation rate of the hydrogel. This allowed tuning hydrogel degradation time from days to months. By copolymerization with more hydrophilic monomers, injectability of the hydrogels through catheters was substantially increased. Patterned subxiphoid transepicardial injections on a beating porcine heart were achieved facilitated by a miniature robotic delivery device. Scavengers for reactive oxygen species were incorporated into the platform design, producing an antioxidant hydrogel which significantly mitigated infarction/reperfusion injury in rat hearts and reduced ventricular cell apoptosis. In a parallel study a connective porous structure was generated in the injected hydrogel and decellularized porcine urinary bladder components were added. Cell infiltration into these hydrogels was greatly increased, and macrophages were polarized towarding a more constructive phenotype.

**TABLE OF CONTENTS**

## LIST OF TABLES

## LIST OF FIGURES

# PREFACE

Cardiovascular disease is a worldwide issue. It poses heavy burdens on patients, families and communities. At the first time I learned about the concept of intramyocardial biomaterial injection for treat MI from Dr. Wagner, I realized that this is the field I can make my minute contribution to with my background. It will be naive to think that our designs are destined to be widely adopted in the future. However, if our research can be a reference for the research field in developing a practical therapy beneficial to the patients, then our efforts will not be in vain.

This dissertation describes the projects and major results of my PhD study, which embodies the coordinated, highly professional inputs from many collaborators from different specialties. Therefore I would like to take the opportunity to extend my appreciation to the people who have been so crucial to the accomplishments of this work and my progresses.

I would like foremost to thank Dr. William Wagner for being a dedicated advisor and mentor. He sets a great example for an intelligent, earnest and down-to-earth researcher and team leader. The most impactful and enlightening knowledge among all that he has patiently taught me is his way of thinking as a successful scientist. This will be an invaluable asset for my career development combined with other experiences he generously passed me.

I am genuinely grateful to my committee members Dr. Eric Backman, Dr. Kang Kim, Dr. Bing Wang and Dr. Kimimasa Tobita for their unreserved direct support on experiment implementation and thoughtful guidance throughout my research. Their visionary insights greatly increased the depth of the study.

Special thanks are attributed to the talented surgical team, without them none of the animal studies would be possible. Dr. Hongbin Jiang, Dr. Tomo Yoshizumi, Dr. Yasumoto Matsumura, Dr. Hideyoshi Sato and Dr. Takafumi Uchibori contributed their unparalleled expertise to surgeries, data collection and analysis. Staffs from UPMC, McGowan Institute and the university ensured the progress of our research and reduced the suffering of the experiment animals.

I owe big gratitude to Dr. Devin Nelson and Dr. Zuwei Ma, who shared their precious understanding and technical details on polymer synthesis and characterization gained from their years of thinking and practice working on this project. Dr. Sang-ho Ye, Dr. Yi Hong, Dr. Jian Wu and Dr. Jianjun Guan also provided useful suggestions on polymer design with their abundant knowledge in polymer materials. Thanks also goes to Dr. Cameron Riviere, Dr. Nathan Wood and the rest of the HeartLander team from Carnegie Mellon University, who showed me the power and possibilities of robotics technologies beyond my imagination. Dr. Murugesan Velayutham, Dr. Kevin Hitchens, Ms. Lesley Foley, Dr. Daewoo Park's untiring work ethics and expertise in nondestructive tracking and imaging has been an indispensable booster to bring hydrogel characterization to a different level. In addition, I am very grateful to Dr. Stephen Badylak, Dr. Rocky Tuan, Dr. Bryan Brown and their lab members for their generosity on experiment materials, technical support and more preciously, their advices on fabricating more bioactive hydrogels. Leah Fuhrman, Gabriela Nogueira and Abhinav Garg contributed their highly efficient work to the study, your assistance is greatly appreciated.

My colleagues and friends from the Wagner lab and the Department of Bioengineering have made me feel welcome and confident about life and research in Pittsburgh. I cannot express enough thanks to our lab managers Vera Kucharski, Nancy Briones and Lisa Barry. They are the

Captains of logistics of the lab. It has always been exciting and happy experiences whether it is discussing experiments or having random conversations with Dr. Xinzhu Gu, Dr. Antonio D'Amore, Dr. Jun Fang, Zhongwei Mao, Yingqi Chen, Xiguang Yang, Giorgio Menallo, Dima Denisenko and Zheni Xu. It is a great pleasure to me to work with Dr. Venkat Shankarraman, Dr. Megan Jamiolkowski, Dr. Hirokazu Sakaguchi, Richard Hoff, Dr. Nicholas Amoroso, Dr. Kazuhiro Nonaka, Samuel Luketich, Drake Pedersen, and Dr. Huili Fu.

Words cannot express my deepest gratitude to my family for their unconditional love and support. My dear wife Tanchen has always been the greatest supporter for me in pursuit for my career. Coming to Pittsburgh, a city thousands of miles away from home was never an easy decision. Tanchen showed greater courage compared to mine and has been the harbor of my soul during the first two years when I was apart from family. The sacrifice you have made to join me is so tremendous that I do not know whether I will ever be able to repay, even though you never asked me to. Thank you to my parents for raising me as the person I am today. Your everlasting understanding, support and care meant so much to me. Thank you to my parents-in-law for the firm trust in Tanchen and me. My grandparents and all my in-laws, thank you for being the biggest fans and consistently believing me doing something great. I'll try my best to explain what I have done during my PhD study and what I have learned from my life in US.

Thank you everyone for making this dissertation possible. Please consider it as a report, a gift from me and a new start of my life.

Funding for this research was provided by the Commonwealth of Pennsylvania, McGowan Institute of Regenerative Medicine, and National Institutes of Health grants #HL105911 and HL078839.

# 1.0 INTRODUCTION

## 1.1 SIGNIFICANCE

Cardiovascular diseases (CVD) are one of the leading causes of mortality worldwide. In 2012, CVD accounted for 17.5 million deaths around the world [1]. Among CVD, myocardial infarction (MI) and other types of ischemic heart diseases (IHD) are a principal source of mortality [2]. The concept of intramyocardial biomaterial injection therapy was introduced and has been widely investigated during the past decade as a mechanical strategy to reduce left ventricular (LV) wall stress by mechanical load shielding, increasing LV wall thickness and decreasing the ventricle radius, thereby moderating the pathological LV remodeling process (**Figure 1-1**). In 2004, Christman et al. reported that direct injection of fibrin glue into the infarcted myocardium preserved cardiac function, decreased infarct size and increased neovasculature formation [3, 4]. Two years later, Wall et al. described the mechanical contribution of injectates in reducing LV wall stress and improving ejection fraction using finite element modeling. The injection of biomaterials into a thinned ventricular wall increases the wall thickness, thus reducing the myofiber stress, and if the injectate is properly distributed, normalizes the stress in the LV [5]. The early experimental data and the computational model laid the foundation for many subsequent investigations into cardiac wall injection therapy as a potential means for improving functional outcomes in post-MI patients.

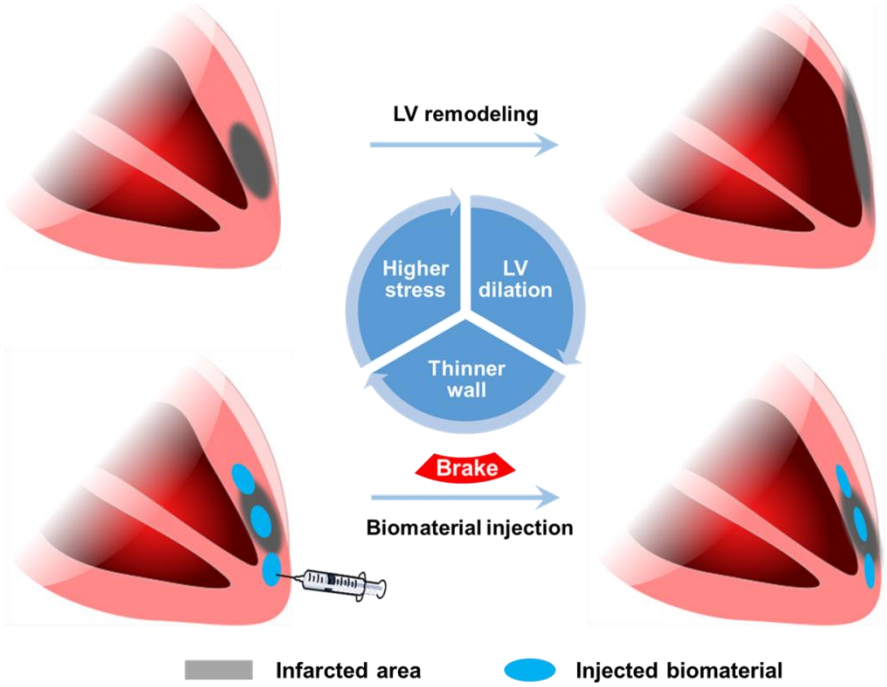


**Figure 1-1.** Ventricular remodeling and intramyocardial biomaterial injection therapy.

The concept of intramyocardial biomaterial injection therapy began to capture the attention of the broader biomaterials community in the first five years after solidification of the concept, with early progress being well-summarized and highlighted by several groups in 2011 [6-8]. A variety of biomaterials including naturally derived hydrogels, synthetic hydrogels, self-assembly peptides and microparticles have been shown to have therapeutic effects in animal models [6-8]. Among all candidate injectate materials, alginate hydrogel was the first to reach phase I clinical trials beginning in 2008 [9]. In the past five years, research and developments in the field have built momentum and significant progress has been made in virtually all aspects of the therapy, bringing this approach closer to the bedside. More biomaterials have entered pre-clinical and clinical trials. More sophisticated models for the mechanical and biological effects of biomaterial injection have been introduced. An array of designed, injectable biomaterials with specific

functionalities introduced have been reported. Optimization of parameters in the injection procedure has been stressed, and more options in minimally invasive injection procedures have been explored.

The collective effort of the community could be assembled at this point into a long-term vision for the implementation of this promising biomaterial-based intervention: (1) imaging of the patient's heart provides data for personalized finite element model construction, emphasizing the spatial distribution of the infarct; (2) a bioactive, bulking material capable of positively influencing post-MI remodeling events is selected; (3) an injection plan with parameters guided by personalized cardiac modeling to achieve optimized mechanical and biological effects is developed; and (4) the patient receives the minimally invasive procedure to precisely deliver the biomaterial and is treated with a complementary pharmaceutical regimen to further facilitate an optimal chronic outcome. In this review, we summarize the progress in the field in the past five years that would contribute to meeting the elements that comprise this vision.

## 1.2 CLINICAL TRIALS AND LARGE ANIMAL STUDIES

### 1.2.1 PRESERVATION-1 trial

As noted above, alginate was the first biomaterial evaluated in clinical trials. IK-5001, an alginate hydrogel (1% sodium alginate plus 0.3% calcium gluconate) developed by Leor et al. and BioLineRX (Jerusalem, Israel) was shown to have therapeutic benefit in terms of reduced LV enlargement and increased scar thickness in a preclinical (porcine) infarction/reperfusion model in 2009 and soon entered a phase I clinical trial (NCT00557531) [9, 10]. In the first-in-

man study, 27 patients with moderate-to-large ST-segment-elevation MI and successful revascularization were enrolled and had IK-5001 injected within 7 days after infarction through the infarct-related coronary artery using an infusion catheter with percutaneous radial artery access [11]. In the earlier porcine model, IK-5001 was shown to diffuse through the vasculature and gel in the infarcted myocardium [10]. Six months follow up showed the safety of the intracoronary hydrogel injection approach [11].

Following the phase I trial, a larger scale PRESERVATION-1 trial (NCT01226563) investigating the effectiveness of IK-5001 for prevention of ventricular remodeling and congestive heart failure was initiated [12-14]. The long-term results were recently reported with the conclusion that intracoronary injection of IK-5001 prevented neither LV remodeling compared to saline control nor the occurrence of heart failure [15]. 303 patients with large ST-elevation myocardial infarction (STEMI) were enrolled and randomized 2:1 to receive a 4 mL injection of alginate or saline in the infarct artery 2 to 5 days following MI. At 6 and 12 months, LV end-diastolic volume index increased for both groups without statistical differences. In addition, no differential improvements were observed in secondary endpoints for the hydrogel group [15]. The lack of clinical efficacy following encouraging porcine model data might be attributable to larger infarction sizes in patients, which would decrease the likelihood of delivery across the entire infarction region. It would be interesting to know how the delivered hydrogel was distributed with respect to the varied infarcts in the patient group and whether LV wall thickening was observed. Additionally, the degradation rate of the injected material was unknown. There are also conceptual concerns associated with the intracoronary delivery method. Infusion of the hydrogel precursor into the coronary arteries might be expected to be

accompanied by the risks of hydrogel occluding smaller vessels and remote embolization. Such effects may be sub-clinical and obviate mechanical benefits provided by the hydrogel myocardial placement.

### 1.2.2 **AUGMENT-HF trial**

An alternative alginate-based strategy has been pursued by Lee et al. and LoneStar Heart (Laguna Hills, USA). Different from the IK-5001 studies, open chest surgeries were employed to directly inject alginate based Algisyl-LVR (a mixture of a $Na^{+}$-alginate component and a $Ca^{2+}$-alginate component consisting of water insoluble particles in water plus 4.6% mannitol) to infarcted canine hearts instead of with a minimally invasive approach [16]. Algisyl-LVR injection significantly increased ejection fraction (EF) and reduced LV end-diastolic and end-systolic volumes (EDV and ESV) compared to the saline injection control [16, 17]. First-in-man evaluation of the safety and feasibility of Algisyl-LVR injection therapy was initiated in 2009 (NCT00847964) [18, 19]. Six patients with ischemic (n=4) and nonischemic (n=2) dilated cardiomyopathy in the uncontrolled pilot study received individual injections of 0.25-0.35 mL Algisyl-LVR at 10-15 locations at the LV midventricular level, halfway between the LV apex and base starting at the anteroseptal groove and ending at the posteroseptal groove. These injections were performed under direct visualization during a coronary artery bypass grafting or valve surgery and the procedure was shown to be safe and tolerable [18]. Improvements in EDV, ESV and EF were observed as early as 3 days following surgery for all patients [18]. In addition, magnetic resonance imaging (MRI) was performed to facilitate reconstruction of patient specific LV geometry in a FE model [20]. Output from the model showed an increase in the volumetric-averaged wall thickness for all patients and a 35% decrease in myofiber stress [21]. Expanding

from this pilot study, the multicenter AUGMENT-HF trial (NCT01311791) enrolled 78 patients with advanced heart failure (LVEF≤35%, peak $VO_2$ of 9.0-14.5 mL/min/kg), randomizing them to an experimental group receiving Algisyl-LVR injections in addition to standard medical therapy or to a control group receiving standard medical therapy alone [22]. Over the 12 month follow up, mean peak $VO_2$ and mean 6 min walk distance gradually increased in patients injected with Algisyl-LVR while these parameters worsened in the control group [22]. Despite favorable trends in EF shortly after injection [18], LV end-diastolic diameter (EDD), LV end-systolic diameter (ESD), and LV mass observed over time for the Algisyl-LVR group, none of these parameters varied significantly between the treatment groups [22].

Apart from the positive outcomes of the AUGMENT-HF trial, the delivery method (sternotomy or thoracotomy) excludes patients receiving exclusively percutaneous coronary interventions (PCI). On the other hand, the material strength (authors did not specify) of Algisyl-LVR is 3-5 kPa [21], which is less than normal myocardium and stiffer fibrotic tissue, leaving considerable room for improvements in creating a mechanical shielding effect. In addition, although the relatively simple composition of the alginate hydrogels are attractive from a regulatory perspective, the bioactivity of such hydrogels is limited, suggesting another direction for improving therapeutic outcomes.

### 1.2.3 **Phase I trial of extracellular matrix hydrogel (VentriGel)**

A hydrogel (VentriGel) derived from decellularized porcine myocardial tissue has been developed by Christman et al. and Ventrix, Inc (San Diego, CA) and is recruiting patients for phase I clinical trial (NCT02305602) [23-25]. The uncontrolled study will evaluate the safety and feasibility of trans-endocardially delivered VentriGel in patients with LVEF of 25-45%

secondary to MI. Primary endpoints will be serious adverse events in the 6 months after injection, and secondary endpoints will be efficacy indicators including ESV, EDV, EF and scar mass [24]. Unlike the aforementioned PRESERVATION-1 and AUGMENT-HF trials, patients will receive VentriGel injection via a MyoStar catheter and NOGA mapping will guide injections that will occur 60 days to 3 years after MI. This population will thus represent infarcts that are in the chronic stage and will be the first clinical trial to evaluate the efficacy of injection therapy in this later period. The use of a gel derived from decellularized cardiac tissue provides a means to deliver structural and functional molecules secreted by the resident cells of a specific tissue source and preserved in the subsequent processing steps [26]. These types of materials have been derived from numerous tissue sources and shown to provide therapeutic effects in a broad variety of tissue engineering and regenerative medicine applications [27], [28]. VentriGel injection into porcine myocardial infarcts has been associated with improvements in cardiac function, ventricular volumes, global wall motion scores, and blood vessel formation, while not exhibiting damage to peripheral tissues, nor disrupting cardiac rhythm [29, 30]. The safety and efficacy of the endomyocardial delivery method using arterial access were also confirmed in this model.

### 1.2.4 **Large animal studies**

During the last 5 years, more materials have been evaluated in preclinical trials. Aside from the aforementioned alginate based hydrogels and ECM hydrogel, hyaluronic acid (HA) based materials and calcium hydroxyapatite microspheres are the most extensively studied. Polypeptide and synthetic hydrogels have enriched the variety of biomaterials that have reached the stage of large animal studies. A summary of recent large animal studies are presented in **Table 1.**

**Table 1-1.** Representative recent large animal studies.

| Material | Species | MI Model | Injection time | Injection volume | Observation time | Cardiac function | Reference |
|---|---|---|---|---|---|---|---|
| Modified HA | Yorkshire pigs, 65-70 kg | Permanent ligation of proximal LCx | 60 min after | 30 * 200 μL | 8 weeks | Improved EF,FAC | 31 |
| Modified HA | Yorkshire pigs, 25 kg | Permanent ligation of OM1 and OM2 | Immediately after | 9 * 100 μL | 2 weeks | No functional improvement | 32 |
| Modified HA | Yorkshire pigs, 40-50 kg | Permanent ligation of LCx and OM branches | 30 min after | 20 * 300 μL | 12 weeks | Improved EF, ESV | 33 |
| Modified HA | Dorset sheep, 35−40 kg | Permanent ligation of the LAD and DB | 30 min after | 20 * 300 μL | 8 weeks | No improvements in EF, only one hydrogel group improved ESV | 34 |
| Modified HA | Dorset sheep, 45 kg | Permanent ligation of OM branches | 30 min after | 16 * 300 μL | 8 weeks | Improved EF, ESV | 35 |
| Calcium hydroxyapatite microspheres | Sheep, 35-40 kg | Permanent ligation of LAD and DB | Within 3 h | 20 * 130 μL | 8 weeks | Improved EF, greater infarct blood flow | 36 |
| Calcium hydroxyapatite microspheres | Yorkshire pigs, 37.2±1.2 kg | Permanent ligation of LCx or its branches | 30 min after | 20 * 150 μL | 4 weeks | Improved EF, ESV, EDV | 37 |
| Calcium hydroxyapatite microspheres | Yorkshire pigs, 25 kg | Permanent ligation of OM1 and OM2 | Immediately after | 20 *150 μL | 3 weeks | Improved EF | 38 |
| Calcium hydroxyapatite microspheres | Sheep, 35-40 kg | Permanent ligation of LAD and DB | Within 60 min | 1.3 mL (n=6) or 2.6 mL (n=5) | 8 weeks | EDV decreased with 2.6 mL injection but not with 1.3 mL | 39 |
| VentriGel (ECM) | Yucatan mini pigs, 45-50 kg | Percutaneous coil embolism infarct of LAD | 2 weeks after | 14 to 15 * 250 μL | 3 months | Improved EF, FAC | 30 |
| VentriGel (ECM) | Yucatan mini pigs, 28-40 kg | Percutaneous coil embolism infarct of LAD | 2 weeks after | 15 * 250 μL | 1-2 h | Not reported | 29 |
| Particulate ECM | Jersey calves, 65-95 kg | Polystyrene latex microspheres embolization of LAD and/or LCx | 30 days after | 9-11 mL | 60 and 90 days | Improved EDP, ESV, EDV; n=2 for each group | 42 |
| Algisyl-LVR (Alginate) | Canine | Polystyrene latex microspheres embolization of LAD and LCx | 2 weeks after | 7 injections, total 1.8 to 2.1 mL | 17 weeks | Improved EF, ESV, EDV | 17 |
| Modified PEG | Goat, 70 kg | 75 min occlusion of proximal LCx | 4 weeks after | 10 * 200 μL | 4 weeks | Not reported | 40 |
| PDGF binding peptide | Mini pigs, 5 months old | Permanent occlusion of LAD | Immediately after | 40 * 50 μL | 12 weeks | Improved EDP and -dP/dt | 41 |

LAD: left anterior descending artery; LCx: left circumflex artery; OM: obtuse marginal artery; DB: diagonal branches; PEG: polyethylene glycol; PDGF: platelet-derived growth factor.

The porcine model is one of the more frequently utilized large animal models and is attractive in that the coronary artery system is very similar to that of humans [43, 44], with the right-side dominant manner in which the blood is supplied to the coronary artery system. Also, the conduction system is similar to 90% of the human population [43]. Since there is little collateral blood supply, a distinct infarct is easier to create, whereas in other animal models such as dogs the collateral circulation makes such infarcts difficult to achieve [44]. However, there are several differences between the porcine model and the clinical situation that need to be considered when analyzing the results in large animal studies. First, the infarctions are usually created with ligations or intra-arterial occlusions in young, otherwise healthy animals, lacking the underlying chronic cardiovascular disease (e.g. arteriosclerosis and hypertension) and other co-morbidities present in the target clinical population. Secondly, the majority of the reported

large animal studies did not involve a reperfusion or revascularization process (**Table 1**). The priority for MI patients is to reestablish the blood supply to the endangered myocardium. Skipping the reperfusion process not only skips the observation period afterwards, more importantly it excludes the reperfusion injury from the animal models, whereas reperfusion injury is a substantial complicating factor defining the extent of an infarct and efficacy of later interventions [45-47]. Finally, over 60% of the studies listed in **Table 1** delivered the hydrogel within 60 min after infarct creation. This time frame is not realistic for the majority of patients suffering MI and at risk for ischemic cardiomyopathy.

## 1.3 MECHANISMS OF BIOMATERIAL INJECTION THERAPY AND INFLUENCE OF INJECTION PARAMETERS

Initiated by the mechanical analysis of Wall et al., the discussion of the mechanical effect of ventricular wall biomaterial injection has been the focus of mechanistic studies [5, 48]. In the last 5 years, substantial progress has been made in the areas of personalized mechanical analysis supported by advanced imaging techniques, understanding the influence of material distribution and modulus on the mechanical properties of the LV, and additional biological effects from injected biomaterials beyond wall thickening and stiffening.

### 1.3.1 Computational mechanical simulation base on imaging derived models

Due to the complexities and limitations in collecting real-time, in vivo measurements, computational modeling has become a dominant tool in characterizing the mechanical impact of

hydrogel injection. In a study combining experimentation and modeling, Kichula et al. validated the LV stiffening and fiber stress relieving effect predicted by FE models with biaxial testing [49]. Early computational efforts employed simplified cardiac geometries better suited for addressing the general phenomena driving injection therapy [48]. More recently, imaging techniques, particularly MRI, have facilitated the development of case-specific construction of FE models with increasing detail.

Wenk et al. generated the contour points for an FE model from real-time 3D echocardiography of sheep with anteroapical infarcts at the end of diastole and systole [50]. Dorsey et al. developed FE models specific to experimental pigs in a 12 week study and achieved serial, non-invasive estimation of infarct material properties [33]. Global LV structure and function were assessed by cine MRI, and infarct expansion was visualized by late-gadolinium enhancement (LGE) MRI. Tissue strain was assessed from passive wall motion given by epicardial tagging, and was used to calculate the physical properties of infarcted myocardium through an FE model [33].

With patient-specific MRI data from the AUGMENT-HF trial, Lee et al. described a protocol to build an FE model of the LV which captured the contraction-dilation movements and ED and ES pressures [20]. The contour was derived by digitizing the endocardial and epicardial surfaces, as shown in **Figure 1-2**. Material properties as model parameters were adjusted to match the computed EDV and ESV with the imaged volumes [20]. The fiber stress calculated from the model was shown to decrease as a result of hydrogel injection, accompanied by improved cardiac function, increased wall thickness and reversed remodeling (**Figure 1-2)** [20, 21]. In this study, predefined myofiber directions were assigned to the model to generally mimic cardiac anatomy. Recognizing the significant and sensitive influence of myofiber orientation on

LV mechanics, a diffusion tensor magnetic resonance imaging (DTMRI) based approach was recently described to derive patient-specific myofiber orientation. Toussaint et al. acquired 2D Diffusion Tensor Images in healthy volunteers and proposed a dense approximation scheme of the complete 3D cardiac fiber architecture of the LV that was validated using *ex vivo* hearts [51]. This method is expected to capture local fiber disarray for individual patient infarct regions, which could facilitate the incorporation of the first patient-specific fiber orientation into the patient's in silico reconstructed LV geometry [48, 51].

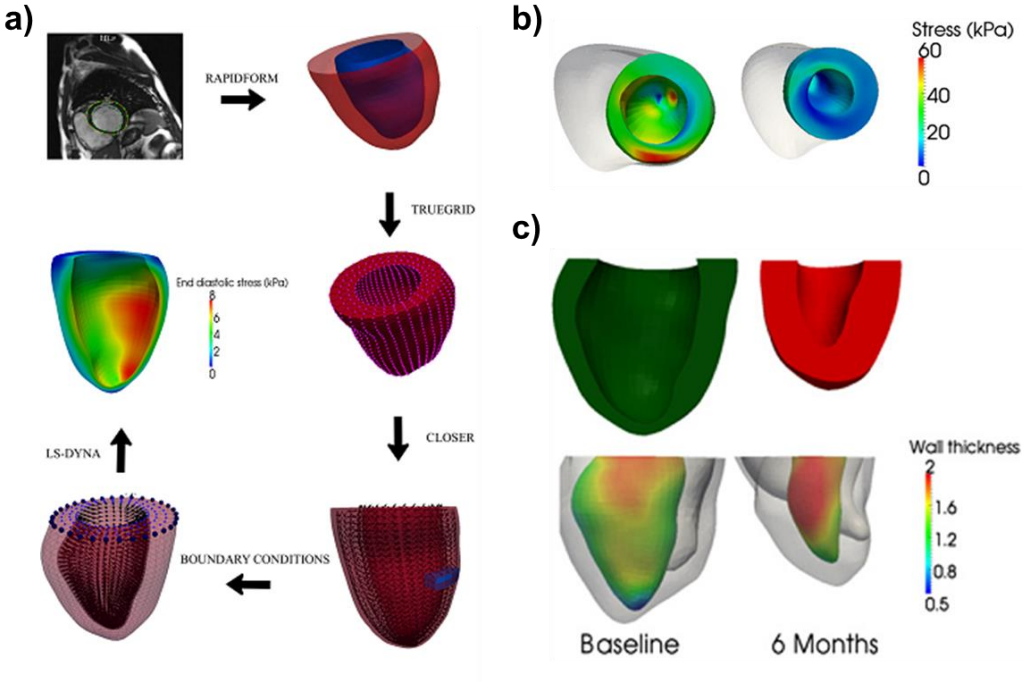


**Figure 1-2.** (a) Steps involved in the quantification of left ventricular wall stress from MRI characterization to FE calculation [20]. (b) Calculated end-systolic regional myofiber stress distribution of a patient at baseline (left) and 6 months after surgery (right) [21]. LV epicardium is displayed in white. (c) Top: cross-section view of LV at baseline (left) and 6 months (right). Bottom: measured regional LV wall thickness based on the MRI-reconstructed LV of the same patient in (b) [21]. Wall thickness unit: cm.

### 1.3.2 **Influence of biomaterial properties and injection parameters**

In addition to acquiring accurate, patient-specific geometric and mechanical cardiac representations, studying the influence of biomaterial properties and injection parameters has been another important research direction to understand the mechanical effects of biomaterial injection. Based on the aforementioned patient-specific modeling study in the AUGMENT-HF trial which demonstrated the stress-relieving effect of hydrogel injection, Lee et al. analyzed potential residual strains and stresses introduced by the same treatment with a modified patient-specific computational model [52]. The simulation showed that the residual stress can lead to more heterogeneous regional myofiber stress and strain fields. Hydrogel injection lowered the stress and stretch in the lateral regions between the injection sites, while above and below the injection site the stress and stretch were increased [52]. This result also highlighted the regional complexity that can result from biomaterial injection beyond broadly described wall thickening and stiffening.

As biomaterial viscosity, gelation mechanisms, injection locations and LV myocardium conditions vary, the distribution of an injected biomaterial may differ markedly, resulting in distinct geometric and mechanical impact on the LV. For example, computational models in a canine infarction model showed that a striated hydrogel distribution was superior to a bulk distribution in terms of reducing wall stress, while the latter was more effective when the hydrogel was delivered later in the remodeling period to the dilated LV wall, where the local tissue would be stiffer and thinner [53]. Similarly in a human MRI derived model, a striated distribution exhibited a greater impact on wall stress and strain at the acute stage while a bulk distribution benefited the fibrotic stage more (**Figure 3a,b**) [54]. In a rat in vivo model, bulk distribution of a degradable PEG hydrogel was achieved as injected 1 week after MI, which

showed significant improvements in scar thickness and cardiac functions compared to the striated distribution associated with injection immediately after MI (**Figure 3c,d**) [55]. However, since the hydrogel was delivered at different time points, the differences in functional outcomes cannot be attributed to intramyocardial distribution of the biomaterial alone, as is discussed below.

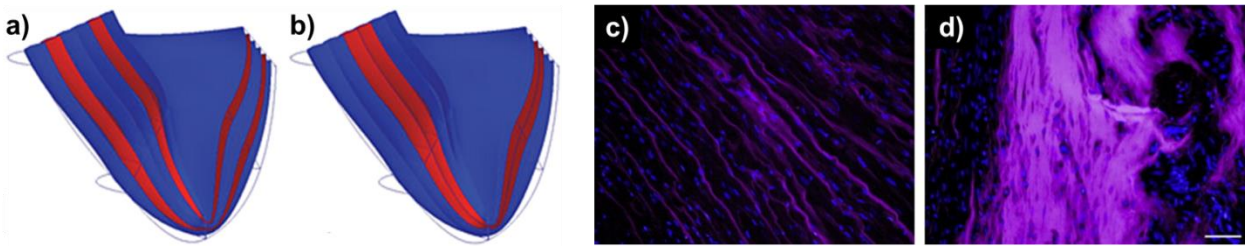


**Figure 1-3.** Biomaterial distribution in silico and in vivo. (a,b) Cross-sectional apical view of infarcted region with different injectate distributions [54]: (a) layered injectate in fibrotic infarct represented as transmural layers (red); (b) bulk injectate in fibrotic infarct represented as transmural layers. (c,d) Alexa Fluor 660 labelled PEG hydrogel (purple) distribution in infarcted hearts [55]. Hydrogel injected (c) immediately after infarction, and (d) 7 days after infarction. Scale bar = 50 μm.

In addition to biomaterial distribution, the total volume of biomaterial injected affects the observed mechanical changes. Computational simulations by Wall et al. showed that a biomaterial injection corresponding to a 4.5% increase in LV wall volume reduced post-MI border zone fiber stresses and positively affected EF and global function, whereas smaller volume changes (0.5% to 1.5%) did not have such an effect [5]. In a sheep model Dixon et al. found that 1.3 mL microparticle injection did not favorably impact the post-MI remodeling process, in contrast with functional improvements observed in animals receiving 2.6 mL injections [39]. As the peak LV mass for adult males and females are 200 and 145 g respectively,

and decrease with age, [56, 57] the minimum effective injection volume can be predicted to be 5-8 mL based on the model of Wall et al [5]. Therefore, the less-than-expected effects of the PRESERVATION-1 trial (injection volume = 4 mL) and AUGMENT-HF trial (injection volume <5 mL) may potentially be attributed to inadequate injection volumes. Wise et al. evaluated the influence of hydrogel injectate volumes in an FE model of rat infarcts. The results showed that the therapeutic effects of hydrogel injection, including ventricular function and wall mechanics, increases with injection volume, but this benefit is limited or decreases at higher levels, indicating the existence of a threshold or an optimal volume [58].

In addition to material choice and injection parameters such as material distribution and volume, the timing of biomaterial delivery post-MI is a critical factor, as well. Key events including myocyte apoptosis and necrosis, acute and chronic inflammation, and fibrosis in LV remodeling occur consecutively after MI, continuously reshaping the local mechanical and biological environment [59]. Therefore the influence of injected biomaterials is superimposed on highly dynamic remodeling processes and would be expected to exert different effects based upon when the intervention is applied. A positive functional effect from alginate hydrogel injection on LV remodeling in rats has been observed in both recent and older infarcts (1 and 8 w post-MI), as a general model of patients at differing stages of remodeling following MI [60]. Kadner et al. compared the efficacies of injecting a matrix metalloproteinase (MMP)-sensitive PEG hydrogel immediately or 1 w after MI in rats. Immediate delivery resulted in the diffusion of hydrogel through the myocardium, while delayed injections resulted in the formation of a bulk hydrogel pocket. Also of note, the hydrogel degraded much faster when delivered immediately after MI compared to 1 w post-MI, another result of the differing physical and biological LV wall milieu. These differences are intertwined with the findings that beneficial functional effects were

observed only in the 1 w group [55]. Yoshizumi et al. tested three injection time points in a rat model: immediately after MI, 3 d post-MI, and 2 w post-MI corresponding to the beginnings of the necrotic, fibrotic and chronic remodeling phases. The best therapeutic outcomes were found when the PNIPAAm-based hydrogel was injected 3 days after MI and this outcome was related to fluctuations in neutrophil and macrophage infiltration and inflammatory signals [61]. This study also implied the existence of an optimal window for biomaterial injection.

### 1.3.3 **Biological response induced by injection therapy**

Recent research reports have also focused on the biological response to biomaterial injection therapy. As the injected biomaterials alter the local mechanical environment for the preexisting and post-MI recruited cells, these cells translate the mechanical inputs to downstream biological signals. In addition, the injected biomaterials and their degradation products could, for instance, shift the pH and ion balance in the niche, and influence the inflammatory, fibrotic and foreign body responses. Some biomaterials with inherent bioactivity such as the ECM-derived hydrogels, may induce desirable post-injection therapeutic outcomes. Histological evidence of increased vascularization, reduced inflammation and mitigated scar formation due to biomaterial injection has been extensively reported across studies involving various types of biomaterials [60-65]. For instance, Zhao et al. showed that functional improvements following post-MI injection of a hydrogel derived from small intestine ECM were associated with recruitment of c-kit-positive cells, myofibroblasts, and macrophages [66].

In an ovine MI model, Dixon et al. examined the influence of calcium hydroxyapatite (CHAM) injection on matrix synthetic and proteolytic pathways. Downregulation of MMP-13, MMP-7 and collagen was found in the CHAM injection group compared with MI only controls,

suggesting that the favorable therapeutic effect with CHAM injection was partly due to alteration of MMP/TIMP (tissue inhibitors of MMPs) profiles [39]. Wassenaar et al. attempted to better understand the effects of ECM-derived hydrogel injection treatment on local cellular response. Over 2000 genes were analyzed with a whole transcriptome microarray 3 d and 1 w after injection to identify potential pathways linked to the previously reported beneficial outcomes [30, 67]. Principal component analysis and pathway analysis showed that alterations in pathways associated with the inflammatory response (**Figure 1-4**), cardiomyocyte apoptosis, infarct neovascularization, cardiac hypertrophy and fibrosis, metabolic enzyme expression, cardiac transcription factor expression, and progenitor cell recruitment all may have contributed to cardiac functional improvement [67]. Suarez et al. explored the influence of biomaterial injection on action potential propagation across the heart [68]. PEG hydrogels were injected into healthy and infarcted rat hearts as a model material and were found to delay action potential propagation across the LV epicardium compared to saline injection and sham controls [68]. In addition, it was found that a highly diffused hydrogel does not alter action potential propagation, while a hydrogel that did not spread as extensively would reduce gap junction densities and may create a substrate for arrhythmias [68].

Despite the aforementioned progress, the links between the mechanical effects of biomaterial injection and histological and functional improvements are still weak and incomplete. The key components corresponding to each bioactive injectate are yet to be identified. It is well known that the renin-angiotensin system (RAS) is an essential regulator of cardiac functions, and that high mechanical load induces elevation of angiotensin II (Ang II), a factor that plays an important role in ventricular remodeling (**Figure 1-5**) [59, 69-71]. Pathologically high Ang II levels lead to adverse post-MI responses including high oxidative

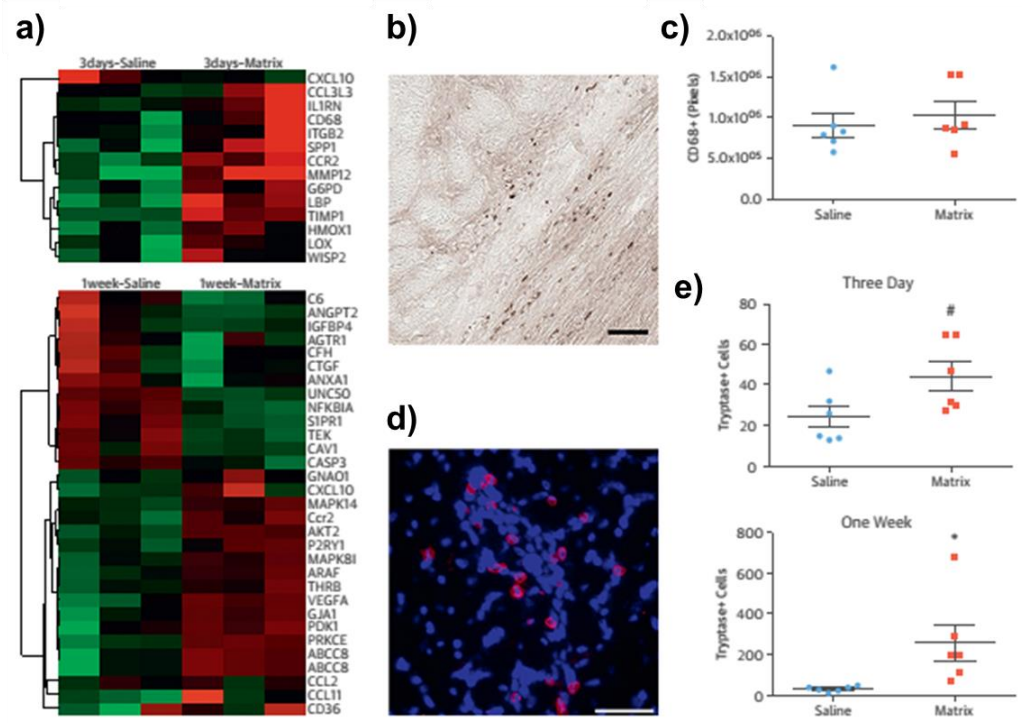


**Figure 1-4.** (a) Expression of genes (red = upregulated; green = downregulated) involved in inflammation at 3 d and 1 w. (b) CD68 staining for macrophages in a myocardial matrix-injected infarct 3 d after injection, visualized by 3,3'diaminobenzidine (brown). (c) Quantification of CD68 staining in the infarct wall 3 d after injection. (d) Tryptase+ (red) cells in myocardial matrix injected heart at 1 w after injection; nuclei (blue). (e) Quantification of all tryptase+ mast cells in the infarct wall 3 d and 1 w after injection. Scale bar = 50 μm. #$p$=0.052. *$p$<0.05. [67]

stress, inflammation and fibrosis, therefore administration of Ang II blocker or angiotensin converting enzyme inhibitor has shown beneficial effects in MI treatment [72, 73]. Thus the RAS and Ang II could be the key to establishing a link between the mechanical effect of biomaterial injection and related pathological responses. For ECM-derived biomaterials, identifying key components could facilitate the enhancement of corresponding benefits. For example, Okada et al. evaluated 2 forms of porcine-derived small intestinal submucosa (SIS) hydrogels as injectates for MI treatment and found that the level of basic fibroblast growth factor may partly explain the differential efficacies [74].

### 1.3.4 **Prediction of therapeutic outcome**

Progress in mechanistic studies of biomaterial injection therapy may facilitate outcome prediction and personalized designs for future patients. Although the problem is complex,

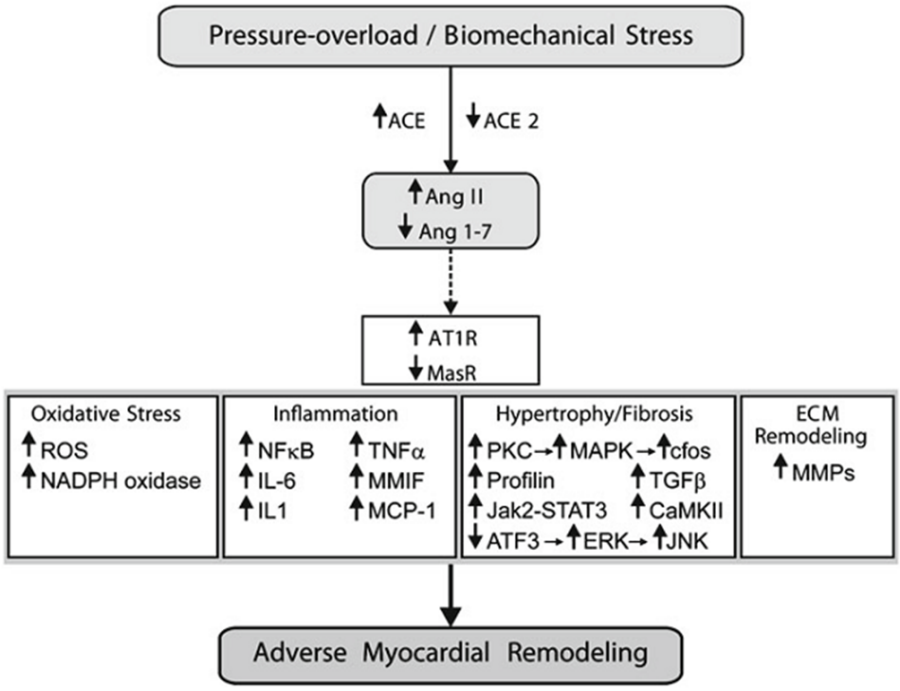


**Figure 1-5.** Pressure-overload-induced Ang II signaling pathways which result in adverse myocardial remodeling. Solid line: enzymatic pathway; broken line: peptide agonist interacting with its key receptor; Bold line: stimulatory effect. ACE: angiotensin-converting enzyme; AT1R: Ang II type 1 receptor; ATF3: Activating transcription factor 3; CaMKII $Ca^{2+}$/calmodulin-dependent protein kinases II; ERK: extracellular signal-regulated kinase; IL-6: interleukin-6; JAK2-STAT: Janus Kinase 2-signal transducer and activator of transcription system; JNK: C-jun-N-terminal kinase; MAPK: mitogen-activated protein kinase; MasR: Ang 1–7 receptor; MCP-1: monocyte chemoattractant protein 1; MMIF: macrophage migration inhibitory factor; MMP: matrix metalloproteinase; NADPH: nicotinamide adenine dinucleotide phosphate; NFκB: nuclear factor kappa-light-chain-enhancer of activated B cells; PKC: protein kinase C; ROS: reactive oxygen species; TGF-β1: transforming growth factor-β1; TNF-α: tumor necrosis factor-α. [59]

computational models might serve as valuable indicators in clinical planning. Modeling would start with a detailed description of the LV geometry, and possibly regional cell metabolism and systemic levels of humoral factors known to influence the remodeling outcome (e.g. Ang II). Patient-specific myofiber orientation could be incorporated into the geometric model and would influence the mechanical model and gel diffusion. This information would depend upon advancing DTMRI technology. Sirry et al. developed an imaging-based method to construct detailed cardiac architectures of the heart after biomaterial injection by combining the digitized distribution of injected biomaterial in a representative infarcted heart with the geometry of the heart being treated [75]. Histological sections of infarcted rat hearts that were injected with PEG hydrogel were used to reconstruct the hydrogel distribution first. Subsequently, cardiac MRI data of a second heart were collected to create an end-diastolic biventricular geometry and further adjusted to overlay the hydrogel geometry, which generated the predicted computational model of the cardiac wall post-injection [75]. Finally, the model might depict the long-term mechanical and biological effects of the injection therapy by incorporating predicted outcomes from local inflammation, fibrosis and biomaterial degradation on the local geometry and mechanics to influence cardiac output. For instance, to predict scar structure following MI, Rouillard et al. coupled an agent-based model that predicts the integration of physiological cues by fibroblasts to a finite-element model that simulates local mechanics [76]. As the local mechanics at any given time point were predicted based on collagen fiber structure, which can be linked to fibroblast activity, the coupled model captured the dynamic interplay between scar deformation, mechanical loading, and scar material properties [76].

## 1.4 NEW MATERIALS

Biomaterial injection therapy for the cardiac wall continues to focus broadly on two putative modes of action, mechanical and biological. Material design to enhance or add to these properties has been the subject of extensive investigation, together with strategies to create materials that open new possibilities for delivery and retention in the infarcted tissue. One driving force behind the development of such materials has been the debate as to whether mechanical effects from biomaterial injection alone are sufficient for cardiac functional benefit [15, 32, 77]. Although a lack of observed beneficial effect may be due to a variety of reasons, the design of biomaterials with specific mechanical and biological functionalities, and coordinated interaction with the post-MI remodeling process, is of growing interest.

### 1.4.1 **Electroactive materials**

Synchronized electrical signal transduction is essential for normal myocardial contraction. As noted previously, an injected hydrogel with minimal interstitial spreading may delay LV activation upon injection and reduce gap junction density, possibly resulting in an arrhythmia [68]. Therefore, efforts have been made to fabricate conductive injectable biomaterials for MI treatment. Mihic et al. grafted polypyrrole (PPy) to nonconductive chitosan to create a semiconductive PPy-chitosan hydrogel, as shown in **Figure 1-6a** [78]. In a rat MI model, PPy-chitosan injection improved conduction as indicated by a decreased QRS interval and increased transverse activation velocity compared to saline or chitosan controls. The material conductivity also contributed to improved cardiac function in comparison with the chitosan group, in addition to the therapeutic effect from chitosan injection [78]. Cui et al. synthesized a conductive poly N-

isopropylacrylamide (NIPAAm)-based biodegradable thermoresponsive hydrogel by covalently attaching electroactive tetraaniline (TA) to a sidechain of the copolymer (**Figure 1-6b)** [79]. Under pulsed electrical stimulation this hydrogel supported cell proliferation and differentiation of H9c2 cells, especially when doped with HCl, and the TA component endowed antioxidant activity to the hydrogel [79]. However, this study did not report cardiac injection data. Baei et al. incorporated gold nanoparticles into chitosan to generate electroactive hydrogels (**Figure 1-6c**) [80], which represents a facile strategy of adding conductive particulates (e.g. metallic particles, carbon nanotubes, graphene nanosheets) to nonconductive hydrogel substrates to create conductive injectable biomaterials. For example, Annabi et al. introduced a highly elastic and conductive hydrogel based on recombinant human tropoelastin and graphene oxide nanoparticles. The composite hydrogel electrically connected explanted abdominal muscles in vitro and supported the growth and maturation of cardiomyocytes [81].

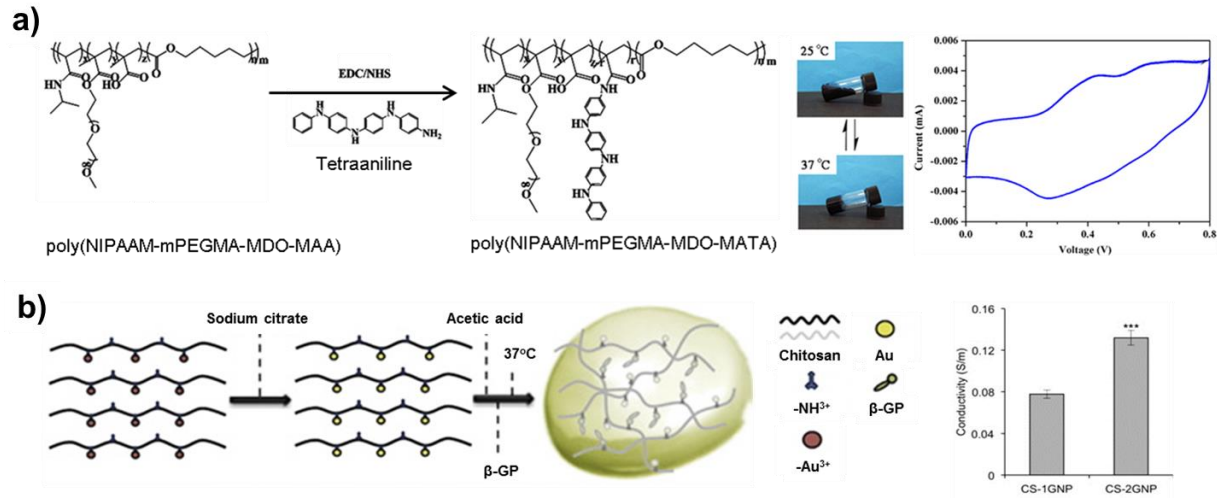


**Figure 1-6.** Examples for conductive injectable biomaterials. (a) Preparation of electroactive tetraaniline-containing thermosensitive (PN-TA) hydrogels. Cyclic voltamogram of the PN-TA2 copolymer in 1.0 M HCl electrolyte solution [79]. (b) Preparation conductive gold nanoparticle-chitosan thermosensitive (CS-GNP) hydrogels; four-point probe conductivity of CS hydrogel that contained different concentrations of gold nanoparticles (n = 3, ***$p$<0.001) [80].

### 1.4.2 **Injectable biomaterials incorporated with bioativities**

A separate focus for adding functionality to injectable biomaterials has been the covalent attachment of bioactive cues or moieties capable of binding bioactive signals. Reis et al. conjugated a chitosan-collagen hydrogel with QHREDGS, an angiopoietin-1-derived peptide that supports cardiomyocyte survival and binds to integrins [82]. The peptide functionalized hydrogel was retained in the myocardium for more than 2 weeks and increased the proportion of cardiac troponin-$T^+$ cells (cardiomyocytes) compared to controls. Cardiac function and scar formation were improved compared with peptide-free hydrogel and MI only controls [82]. Lin et al. injected platelet-derived growth factor-BB (PDGF-BB) binding peptide nanofibers 1 month after infarction in a porcine model [41]. Three months after injection, myofibroblast replenishment was promoted, LV remodeling was positively influenced and cardiac diastolic function was improved [41]. A glutathione containing chitosan hydrogel was developed by Li et al., which showed antioxidant properties and corresponding cardiomyocyte protection against reactive oxygen species in vitro [83]. In vivo influence on cardiac functions awaits evaluation.

Rocca et al. have fabricated a gelatinized alginate hydrogel with uniform capillary-like channels and directly injected this hydrogel into the antero-septal wall at the infarct border zone [84]. Cardiac function was improved compared to saline injection control in a rat injection trial. In addition, the injected hydrogel was vascularized and populated by $CD68^+$ macrophages. These macrophages largely showed an M2-like phenotype as marked by CD206 expression, suggesting a constructive remodeling response [84]. Similar local tissue responses have been observed in disease models treated with decellularized matrix materials [26, 28, 85]. Along these lines,

Johnson et al. have extracted hydrogel material from human myocardial matrix, which has similar in vitro physical properties to porcine myocardial derived hydrogels. In vivo therapeutic effects are yet to be determined [86].

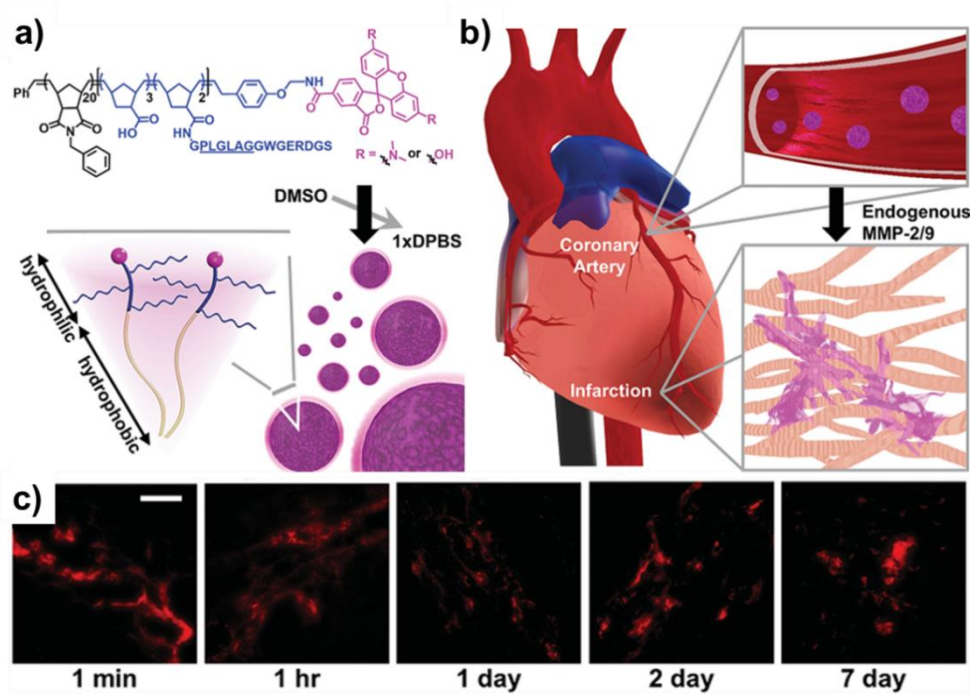


**Figure 1-7.** (a) Diagram of a dye-labeled brush peptide-polymer amphiphile (PPA) containing an MMP-2 and MMP-9 specific recognition sequence (underlined). PPAs self-assemble into nanoparticles through hydrophobic-hydrophilic interactions when dialyzed into aqueous buffer. (b) Nanoparticles freely circulating in the bloodstream (not to scale) upon systemic delivery. Nanoparticles enter the infarct tissue through the leaky MI vasculature, and up-regulated MMPs within the infarct induce the formation of an aggregate-like scaffold. (c) Retention of MMP pretreated responsive nanoparticles and clearance of non-responsive nanoparticles in healthy myocardium. Rhodamine-labeled, responsive particles were observed at the site of injection up to 7 d post-injection. [87]

### 1.4.3 New in situ crosslinking strategies

Despite the high targeting efficacy achieved in the aforementioned studies and the attractiveness of a peripheral injection approach, the mechanical effect for such approaches tends to be weakened as the particles do not crosslink to form a more mechanically robust network [88-91]. However, in situ crosslinking in the myocardium could remedy the defect. Nguyen et al. designed nanoparticles which passively accumulate to the infarcted area through the EPR effect and respond to local enzymatic stimuli (MMPs), resulting in the decomposition of the nanoparticles and subsequent transformation into a network embedded in the myocardium, as shown in **Figure 1-7** [87]. Two days after tail vein injection in a rat MI model, the responsive nanoparticles could be found in the infarct and borderzone, but not the remote myocardium. The polymer was observed 28 d after injection, demonstrating long-term LV retention [87]. The crosslinked network could theoretically lower local mechanical stress, especially during ventricular dilation. However, by principle responsive nanoparticles can only reach preexisted tissue intervals, thus crosslinked hydrogel can only be deposited in the existing available space, possibly resulting in insignificant wall thickening effect. On the contrary, biomaterials injected directly through a needle into the myocardium are propelled by the pressure in the syringe or catheter, leading to the expansion of tissue intervals as the biomaterial squeezes through, which ensures thicker ventricular wall. Despite the less thickening effect of in situ crosslinking nanoparticles, wall stress reduction can be enhanced by incorporating material-tissue crosslinking mechanisms to unite the material network with local myocardium. Besides circulating nanoparticles, novel in situ gelation mechanisms have been adopted in many recent hydrogel designs to create mechanically stronger, diffused gelation networks at injection sites. Bastings et al. developed supramolecular ureido-pyrimidinone (UPy) modified PEG hydrogels

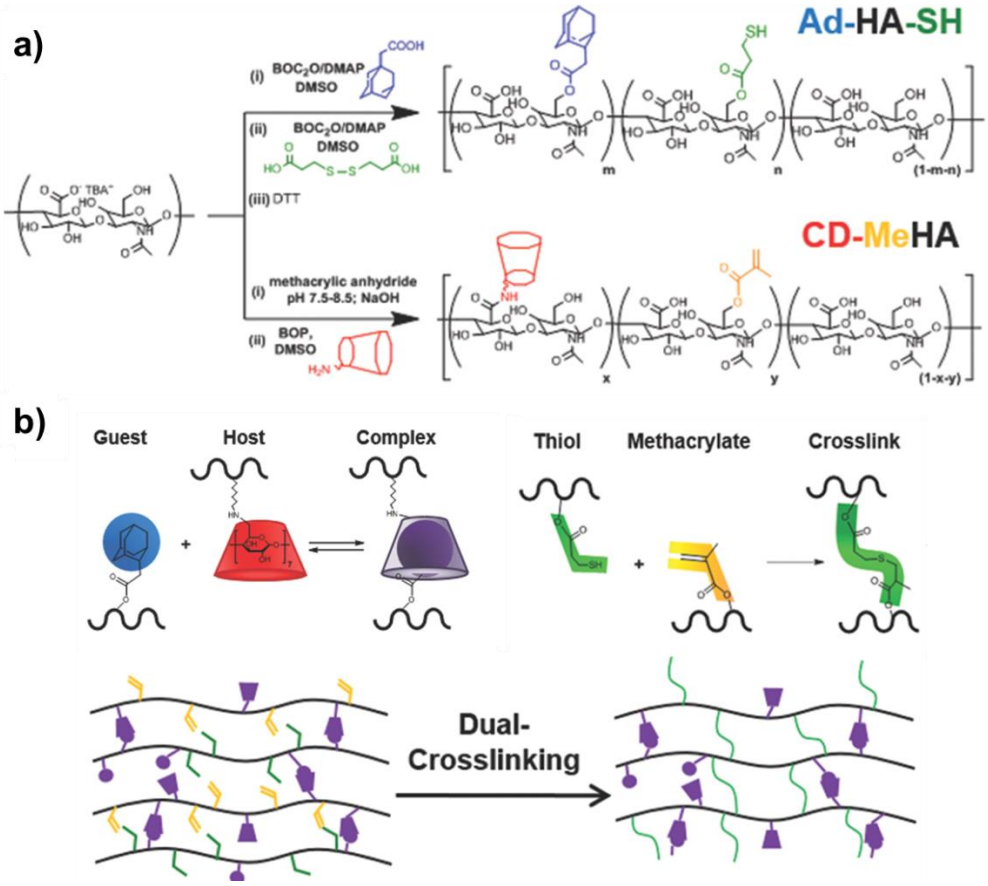


**Figure 1-8.** Synthesis of guest Michael-donor (Ad-HA-SH, Ad: adamantine) and host Michael-acceptor (CD-MeHA, CD: β-cyclodextrin, MeHA: methacrylated HA) macromers. (B) Schematic of dual-crosslinking hydrogel formation: interaction of Ad (guest) and CD (host) in formation of a reversible guest-host complex crosslink; addition of thiol and methacrylate in formation of a covalent crosslink. [92]

which remained a low viscosity fluid at high pH (>8.5), but underwent sol-gel transition in the infarcted myocardium with its lower pH [40]. The pH responsiveness allowed catheter-based delivery in a porcine MI model that showed the safety of the delivery method [40]. Xu et al. developed a two component system consisting of thiolated collagen (Col-SH) and oligo(acryloyl carbonate)-b-poly(ethylene glycol)-b-oligo(acryloyl carbonate) (OAC-PEG-OAC) copolymers, which gels under physiological conditions via Michael-type addition [93]. The mechanical

strength, gelation time and degradation rate can be tuned by the concentration and ratio of the two components, and degree of substitution for Col-SH. The hydrogel significantly improved cardiac function and reduced infarct size in a 28 d study employing a rat infarction model [93]. Bai et al. employed an aldehyde-amine reaction to crosslink oxidized alginate with collagen upon intramyocardial injection. Compared with a calcium-crosslinked alginate hydrogel, the crosslinked alginate/collagen hydrogel reduced matrix metalloprotease activity and achieved a smaller expansion index [94]. Rodell et al. developed an alternative to photo-crosslinkable methacrylated HA hydrogels by substituting the photo-crosslinking with a host-guest assembly method (**Figure 1-8**) [95]. Adamantine and β-cyclodextrin were attached to HA respectively to form a two-component hydrogel system. The host-guest interaction renders the hydrogel shear-thinning and provides injectability while maintaining stability [95]. This hydrogel was shown to improve cardiac function in a rat MI model [96]. Additionally, Rodell et al. combined thiol-ene Michael addition with the host-guest assembled hydrogel to further increase hydrogel modulus and stability. The dual-crosslinked hydrogel exhibited an enhanced therapeutic outcome compared with hydrogel crosslinked by sole host-guest assembly in both rat and ovine model [35, 92]. The shear-thinning property also facilitated percutaneous delivery via endocardial injection under fluoroscopic and echocardiographic guidance in sheep [35].

### 1.4.4 **Injectate modulus and degradation rate**

To achieve a more comprehensive and deeper understanding of the influence of specific biomaterial parameters on injection therapy, there has been an increasing focus on modulating injectate properties such as modulus and degradation rate, while maintaining the same material platform. Ren et al. synthesized polyNIPAAm based hydrogels with fast and slow degradation by

copolymerization with differing ratios of dextran-PCL containing macromonomer. A rat MI model showed that myocardial contractility was greater with the slower degrading hydrogel (50% weight loss in 30 days) compared with the faster degrading version (50% weight loss in 3 days) [97]. Based on another previously proven effective hydrogel, Zhu et al. introduced an auto-catalyzing strategy to modulate the degradation rate of polyNIPAAm based thermally responsive hydrogels which allowed the hydrogel to decompose on a tunable time scale from days to months [98, 99]. Varying the crosslinking density and hydrolytic stability of crosslinkers, Tous et al. fabricated two degradable HA hydrogels (50% weight loss in ~20 and 60 days) and two hydrolytically stable hydrogels with different modulus (low: ~7 kPa; high: ~35−40 kPa). Results from an ovine MI model indicated that all hydrogels resulted in better cardiac output compared to the MI control group, and the stiffer, stable hydrogels were more effective in limiting expansion of LV volume [34]. The typical moduli range for investigated injectable hydrogels varies from 1 Pa to 100 kPa [62, 86, 100], thus the conclusion derived above was comparing materials on the relatively stiff end of the range and may have limited applicability to softer materials. At the lower end of the stiffness range, the moduli of extracellular matrix based hydrogels have been increased by crosslinking, yet the influence on injection therapy is yet to be determined [101, 102].

### 1.4.5 **Injectate distribution**

Once injected, the distribution assumed by the biomaterial may also be an important factor in achieving a maximal therapeutic effect. This is illustrated by computational models [53, 54], as discussed above. In concert with imaging, injection pattern planning may be pursued prior to surgery, but material design will influence the spread of the injectate once infused into the

cardiac wall. Direct injection of microparticles into the cardiac wall leads to injectate pocket formation regardless of particle geometry (microrods, microcube, microspheres) whereas nanoparticles quickly diffuse through the myocardium [37, 103, 104]. For hydrogel materials, viscosity and gelation time are the major determining factors of distribution. For example, less viscous, slow gelling ECM hydrogels diffuse to distal tissue while more viscous, rapid gelling alginate and HA hydrogels tend to form hydrogel "islands" upon injection [17, 30, 34]. Zhu et al. increased the hydrophilicity of a polyNIPAAm based hydrogel by incorporating a higher percentage of N-vinylpyrrolidone monomer in the polymer backbone, obtaining a low viscosity, slower gelling version. While the relatively hydrophobic hydrogel formed isolated masses in the myocardium, higher hydrophilicity allowed the hydrogel to diffuse through the tissue before gelling [105].

### 1.4.6 **Visualizating of injected biomaterials**

Visualization of injected biomaterial in vivo could provide important information on hydrogel distribution and degradation, which could be useful for evaluating the relationship between injection therapy delivery strategy and the efficacy of the treatment. In small animal models visualization has been achieved by quantum dots for fluorescent imaging, radionuclide imaging and computed tomographic (CT) imaging [104, 106, 107]. In addition, optoacoustic imaging could be a potential tool to not only follow the location and amount of injectate in vivo, but also to provide a noninvasive method to measure the mechanical strength of the injected material and the myocardium [108, 109]. However, imaging depth and scanning area are relatively limited for fluorescent and optoacoustic imaging [110] and repeated radiation exposure by CT might be a

concern for patients. The injectates would also need to be radio-opaque or otherwise labeled for these methods. For extracting patient cardiac geometric and functional information, and establishing case-specific computational models, MRI has become a leading imaging tool in preclinical studies [49]. Dorsey et al. covalently attached an arginine-based peptide to HA hydrogel, which resulted in a 2-fold enhancement in signal strength in chemical exchange saturation transfer MRI and allowed discrimination between different hydrogel materials and surrounding tissue based on their chemistry [111]. Combining material design with the versatility of MRI techniques can be foreseen to provide attractive levels of patient-specific, real-time visualization for cardiac injection therapy.

## 1.5 INJECTION METHODS

As discussed above, injection parameters including volume, distribution and timing may have great impact on the outcome of injection therapy. In addition, the mechanisms and time course for an injectate to "set up" in situ varies with injectate chemistry. Chemical crosslinking, shear-thinning polymers, temperature-driven phase change, pH or ionically driven gelation, have all been employed, while other materials are not designed to undergo any substantial change in mechanical properties [6, 40, 95]. Depending on whether injection occurs in an open surgical field, through a minimally invasive, remote approach, or intravascularly, concerns and constraints on the hydrogel design arise. Risks to the patient associated with the errant delivery of a gelling material into the blood stream (embolic damage) are a clear concern. Further, the ease and precision of the delivery mechanism will have direct impact on the adoption and

efficacy of the therapy. Injection methods that can leverage current surgical and minimally-invasive technologies may lower the translational barrier and be adopted with a lower complication risk.

### 1.5.1 **Direct epicardial injection**

Direct epicardial injection of biomaterial into the LV wall through sternotomy or thoracotomy is the easiest method to control and is theoretically compatible with all types of injectates. As the surgical field is exposed to the clinician, pre-determined injection locations and volumes can be easily achieved and improvised. The precision of direct injection can hardly be challenged by other methods. Another derivative advantage is that the delivery pathway and time spent by a biomaterial in this pathway is minimized. This parameter may be important with materials that rely upon phase change or chemical reaction that may be initiated during the delivery process.

The AUGMENT-HF trial has proven the safety and feasibility of direct cardiac wall injections in MI patients receiving CABG. CorMatrix (Roswell, GA) has developed a porcine ECM delivery system composed of a multi-needle syringe assembly, an automated injection controller, and a portable ultrasound tissue depth measurement system, as shown in **Figure 1-9**. Slaughter et al.demonstrated the feasibility of gas propelled injections in a bovine model of chronic ischemic cardiomyopathy, as well as the ability to control injection volume (0.1–1.0 mL) and penetration depth (3–5 mm) under regulated injection pressure into the target region [112]. However, due to the open-chest requirement for direct injection approaches, the patient population suitable for such an approach is limited. In the AUGMENT-HF trial, patients received injection therapy immediately following coronary artery bypass grafting (CABG)

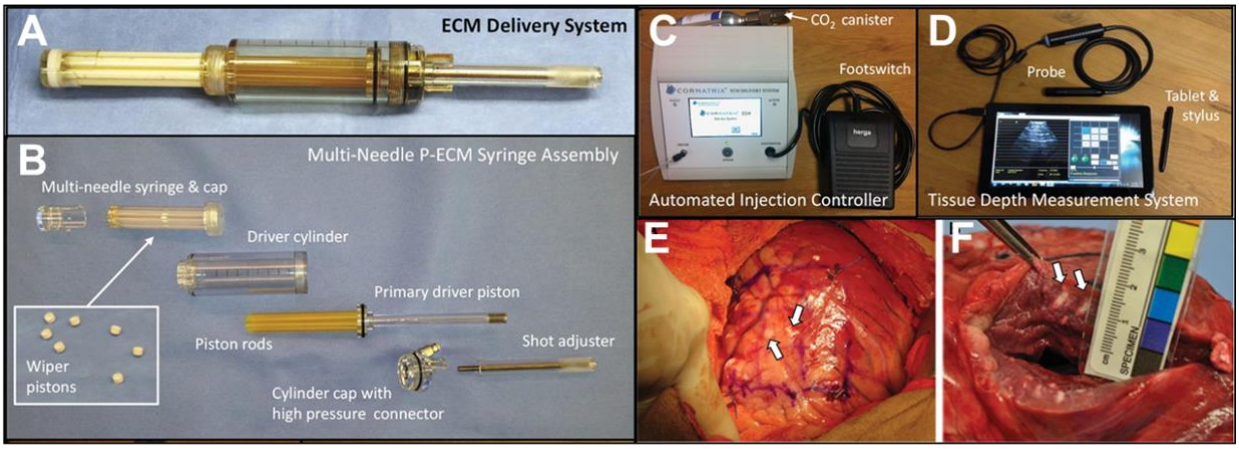


**Figure 1-9.** ECM delivery system component design and ECM intramyocardial injection. (A) Assembled ECM delivery system loaded with 8.4 mL ECM. (B) Exploded view of multi-needle ECM syringe with wiper pistons shown in inset. (C) Automated injection controller with disposable $CO_2$ canister and pneumatic footswitch pedal. (D) Tissue depth measurement system tablet for real-time cardiac imaging for targeting delivery of ECM. (E) In vivo ECM injection sites (white arrows) in bovine LV lateral wall epicardium. (D) Close-up photo of ECM material with measured penetration distance.

surgery, thus a separate sternotomy or thoracotomy was not required. For patients undergoing percutaneous revascularization procedures, a subsequent open-chest procedure would not be an attractive option. A related constraint of an open chest approach is that the injection therapy would likely need to be performed at the time of CABG and could not be optimized to some earlier or later time point.

### 1.5.2 **Minimally invasive approaches**

For patients not receiving CABG or where injection therapy could not be performed in conjunction with this surgery, minimally invasive delivery approaches are highly favored. A

variety of systems have been developed in recent years to facilitate fluid or cell delivery to the cardiac wall [114-116]. These technologies provide the framework to achieve minimally invasive biomaterial injection therapy. Ota et al. developed a novel miniature robotic device (HeartLander) that can navigate on the surface of the beating heart and make guided injections [117]. Zhu et al. delivered a polyNIPAAm-based biodegradable thermally responsive hydrogel into the LV wall of a live porcine heart using HeartLander. Through a small subxiphoid incision, the HeartLander crawler approached the LV, went under the pericardium and used an applied vacuum to anchor on the epicardium (Figure 9A, B). Guided by a real-time tracking system, the crawler moved on the beating heart through "release-re-position-anchor" cycles (Figure 9C) and could navigate to the planned injection sites. Cooled by a fluid sheath around the catheter, the hydrogel was kept in the liquid phase prior to the injections. Four injections in the planned square layout were made, as shown by photoacoustic imaging (Figure 9D, E) [106]. The HeartLander delivery system was considered suitable for a wide variety of injectable biomaterials.

As described above, PCI procedures including intra-arterial infusion and endocardial injections have been employed in clinical and preclinical trials [15, 29, 30, 35]. PCI is widely employed in coronary artery stent placement and other therapies, thus the technical challenges for clinicians mastering this approach would be minimized. A potential drawback is the theoretical risk of biomaterial regurgitation or leakage into the vascular system, causing remote embolization. For intra-arterial infusion, where the presumption is that the material will cross only into the infarcted region and gel there, there is also concern for undesired gelling to occur in non-targeted tissues. For these two administration routes biomaterials with fast solidification kinetics would appear to be a greater risk of forming a mechanically stable embolus. On the other hand, as the intravascular injection route requires long catheters to run through the

vasculature, biomaterials that employ thermally-triggered gelling are less compatible due to concerns of material solidification in the catheter and occlusion of the lumen. For injectable biomaterials that actively or passively target the infarcted myocardium, intravenous injections have been employed in animal models [88, 89, 91]. Intravenous injection is the least invasive delivery method, although there are considerable limits in terms of the volumes and spatial control over the injectate is ultimately delivered to the LV wall.

## 1.6 LIMITATIONS AND CHALLENGES

Our lab previously developed PNIPAAm-based thermally responsive hydrogels (poly(NIPAAm-co-HEMA-co-MAPLA), poly(NIPAAm-co-AAc-co-HEMAPTMC)) which presented therapeutic effects in small animal and large animal myocardial infarction models [113, 114]. In a rat chronic infarction model, the LV wall was injected with the poly(NIPAAm-co-AAc-co-HEMAPTMC) hydrogel. LV cavity area and contractility were preserved at 8 week endpoint. Tissue ingrowth in the hydrogel injected area was observed accompanied with a thicker LV wall and higher capillary density for the hydrogel versus PBS group. In addition, smooth muscle cells with contractile phenotype were identified [114]. Preliminary experiments of poly(NIPAAm-co-HEMA-co-MAPLA) injection in the porcine MI model also exhibited improved cardiac functions compared to PBS control.

However, the polyNIPAAm-based hydrogels has room for improvements shared by some other injectable biomaterials. As shown in **Figure 1-10**, injected poly(NIPAAm-co-HEMA-co-MAPLA) in isolated sites can be found in LV wall 8 w after infarction while not occupied by infiltrated cells. A separate study has shown the importance of injection time, as myocardial

infarction is a highly dynamic process. By principle, the mechanical support weakens as the injected hydrogel weakens, while cell penetration and tissue integration are not initiated prior to hydrogel degradation. Therefore, the degradation rate of injectates (which decides how long the material stays in the LV) may also greatly influence the remodeling process, especially after the acute physiological reactions, which is not fully understood in the field. To study such influence on the platform of polyNIPAAm-based hydrogels, a strategy needs to be developed to modulate the degradation rate while keeping other key physical properties (especially mechanical strengths) unchanged. **Figure 1-10** showed no significant hydrogel degradation in the LV wall. Thus the focus of modulation on degradation rate would be accelerating it.

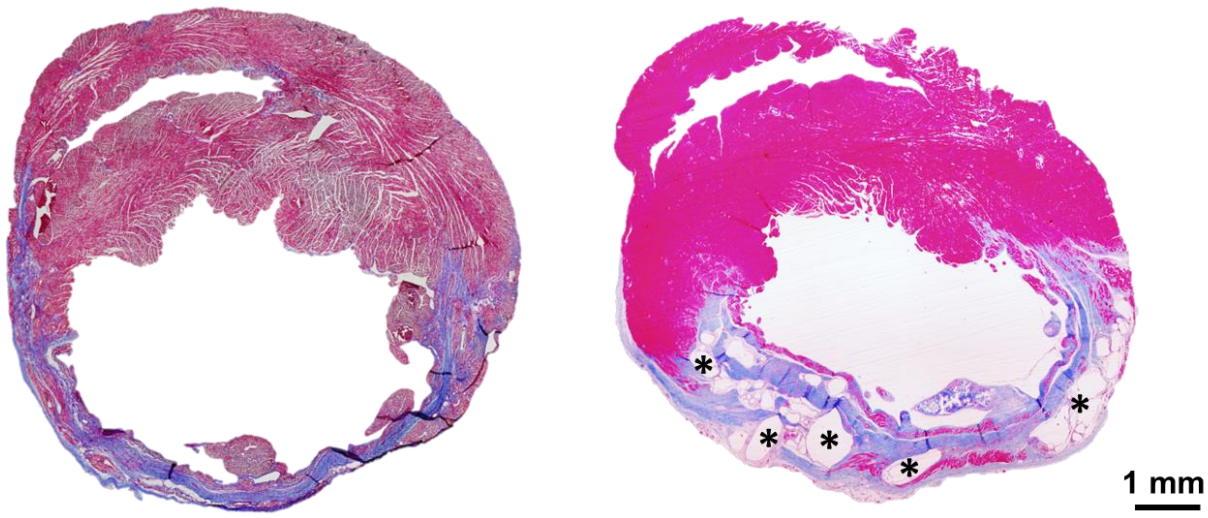


**Figure 1-10.** Infarcted rat hearts 8 weeks after PBS injection (left) and poly(NIPAAm-co-HEMA-co-MAPLA) injection (right). The LV wall was significantly thicker in the hydrogel treated group. *: hydrogel residues.

In addition to slow degradation, cell infiltration and tissue integration are also inhibited by the nonporous nature of gelled polyNIPAAm-based hydrogels. Different from cell infiltration channels generated during degradation, cells can theoretically migrate through preexisted pores

to facilitate tissue integration with the injected material. The challenge is to incorporate porous structure into the thermally responsive hydrogel before injection or shortly after gelation, while maintaining sufficient mechanical support. No strategies of generating porous structures in injectable thermally responsive hydrogels have been introduced before.

On the other hand, unlike their naturally derived counterparts, the polyNIPAAm-based hydrogels are not incorporated with designed bioactivities (e.g. anti-inflammatory effect) besides mechanical support. Growth factors and drugs have been added to non-bioactive biomaterials and improved corresponding functional outcomes [115, 116]. Foreign body responses were observed encapsulating the hydrogel residues in LV wall, which is another typical phenomenon in intramyocardial biomaterial injection therapy. Prolonged foreign body response could induce inflammation and fibrosis. Recent studies have demonstrated that foreign body response could be modulated by biomaterials to favor tissue regeneration and constructive remodeling [117-119]. Extracellular matrix products have been used in intramyocardial biomaterial injection therapy and shown positive effects [30, 67]. However, ECM gel was mechanically weak. Therefore there is room for designing to improve the bioactivity of the polyNIPAAm-based hydrogels, and maintain the mechanical benefits rendered by the injectates.

Last but not least, in previous animal studies, the polyNIPAAm-based hydrogels were directly injected into the myocardium, which did not exhibit the advantage of injection therapy – minimally invasiveness. A robotic injection device (HeartLander) was developed to minimally invasively deliver the hydrogel through a subxiphoid, transepicardial pathway. However, poly(NIPAAm-co-HEMA-co-MAPLA) frequently clotted the sheath of HeartLander in preliminary tests. It is mainly due to the low transition temperatures of current polyNIPAAm-

based hydrogels (below 20 $^{o}$C), thus the hydrogels have a high tendency of gelling. In addition, current version of HeartLander lacks cooling components to keep the hydrogel solutions at liquid phase. In order to achieve minimally invasive delivery with HeartLander, modifications on both hydrogel and the injection device need to be made. The hydrophilicity of polyNIPAAm-based hydrogels needs to be increased to raise the transition temperature, hence lowering the gelling tendency. Additionally, a cooling mechanism needs to be incorporated into HeartLander to provide a low temperature environment.

## 1.7 OBJECTIVES

As discussed above, intramyocardial biomaterial injection is a promising therapy for myocardial infarction in terms of preventing pathological LV remodeling and preserving cardiac functions. The development of biomaterial injection as a potential standard clinical option is at a critical stage as fastest teams have been testing candidate materials in clinical trials and more injectable material systems are expected to enter clinical trial phase in the near future. The success of intramyocardial biomaterial injection requires collective efforts of material design, effectiveness modeling, imaging and minimally invasive delivery. Among the essential components, biomaterial is the core as it ultimately determines the therapeutic outcome.

Previous clinical trials using alginate hydrogels did not show significant functional improvements, which may be partly due to the low modulus. PolyNIPAAm-based biodegradable thermally responsive hydrogels are mechanically strong, biocompatible and presented positive effects in treating MI animals including in the porcine model. As discussed in the previous section, current version of polyNIPAAm-based hydrogels including poly(NIPAAm-co-HEMA-

co-MAPLA) have limitations including hindered tissue integration, chronic foreign body response, lack of bioactivity and feasibility for minimally invasive delivery. These issues are also associated with other types of injectable biomaterials. As synthetic biomaterials, the limitations of polyNIPAAm-based hydrogels could be mediated by improving material design, which is expected augment the functional outcome and increase the opportunity for clinical translation. The overall objective of this work is to design new polyNIPAAm-based hydrogels on current poly(NIPAAm-co-HEMA-co-MAPLA) platform aiming at mitigating previously described issues and investigate the efficacy of the hydrogels in small and large animal models.

### 1.7.1 Objective 1: To tailor the degradation rates of thermally responsive hydrogels by varying the autocatalytic potential

As discussed above, slow degradation hindered cell infiltration and tissue integration within injected poly(NIPAAm-co-HEMA-co-MAPLA) hydrogel in vivo. Therefore, in the first specific aim of this research, a fourth monomer, methacrylic acid (MAA) was added to the copolymer to derive poly(NIPAAm-co-HEMA-co-MAPLA-co-MAA) with different ratio of MAA (pNHMMj, where j represents the feed ratio of MAA as explained in Chapter 2). We hypothesize that the MAA residues in the hydrogel would release proton and lower local pH, and the acidic environment would accelerate the degradation of MAPLA sidechains, which generates LA segments and in turn autocatalyze hydrogel degradation just as external protons. The degradation rate of pNHMMj hydrogels will be characterized in vitro and in a rat hindlimb muscle injection model. This innovative strategy for modulating hydrogel degradation rate only requires a small

amount of MAA and should not significantly influence other physical properties of hydrogel, which also mean that the pNHMMj hydrogels are appropriate candidate to study the effect of hydrogel degradation rate on the therapeutic outcomes of LV injections.

### 1.7.2 **Objective 2: To tailor the hydrophilicity of thermally responsive hydrogels to couple the hydrogels with robotic system for minimally invasive delivery**

Preliminary tests of delivering poly(NIPAAm-co-HEMA-co-MAPLA) hydrogel with HeartLander device ended up with the thermally responsive hydrogel occluding the device catheter. In the second part of the research, we focused on decreasing the inclination of poly(NIPAAm-co-HEMA-co-MAPLA) solution transiting to hydrogels. The corresponding hypothesis is that by increasing the hydrophilicity of copolymer, the viscosity of polymer solution at liquid phase (below transition temperature) would decrease, accompanied by the raise of transition temperature. As a result, the hydrogel solution could be injected more smoothly with less incidences of occlusion. Our design is to replace HEMA with more hydrophilic VP (N-vinylpyrrolidone) residues in the copolymer to derive poly(NIPAAm-co-VP-co-MAPLA). At the same time, a cooling sheath will be added to current HeartLander device in order to keep the hydrogel below transition temperature. The compatibility between poly(NIPAAm-co-VP-co-MAPLA) hydrogels and the robotic injection device will be evaluated on an ex vivo heart, followed by subxiphoid transepicardial injection attempts in a living porcine model. Subxiphoid transepicardial hydrogel delivery pathway has not been reported before and poly(NIPAAm-co-VP-co-MAPLA) hydrogels will be the first synthetic hydrogel to be minimally invasively injected to provide mechanical support to LV wall.

### 1.7.3 Objective 3: To improve therapeutic function of thermally responsive injectable hydrogels by incorporating a reactive oxygen species scavenger

By providing mechanical support to the LV wall, poly(NIPAAm-co-VP-co-MAPLA) hydrogel presented beneficial effect in preserving cardiac function and maintaining LV geometry. However, there is still considerable room for improvements, not only in optimizing mechanical factors, but also in the aspect of incorporating greater bioactivities into the hydrogel. Cells, genes, drugs and other forms of bioactive reagents have been used and studied in clinical conditions and shown positive effect in treating MI. Additionally, the thermally responsive gel forms an isolated mass in the tissue, which could serve as an ideal reservoir for loaded reagents. In this part of research, we aim at lowering the level of reactive oxygen species (ROS) generated as a result of infarction/reperfusion. Pathologically high ROS concentration leads to cell death, inflammation and fibrosis. We design to covalently attach a ROS scavenger, 4-amino-TEMPO, to the sidechain of poly(NIPAAm-co-VP-co-MAPLA-co-MANHS) (MANHS: methacrylic acid N-hydroxysuccinimide ester), deriving poly(NIPAAm-co-VP-co-MAPLA-co-MATEMPO) (pNVMT). Chemical reactions that produce ROS and cell culture under oxidative stress will be used to evaluate the ROS scavenging effect of pNVMT. The capability of pNVMT to protect the ischemic heart will be characterized in a rat infarction/reperfusion model. We expect that by combining mechanical support with ROS scavenging effect, pNVMT will perform better than the single factors working alone.

### 1.7.4 **Objective 4: To fabricate porous injectable hydrogel for faster cell infiltration and pro-M2 macrophage polarization**

Same as other biomaterial implants, injected hydrogel in the LV myocardium induces foreign body response, which recruits a variety of cells including macrophages. Recent studies showed that macrophages have different but interchangeable phenotypes which are closely linked to the roles they play in foreign body responses. M1 phenotype is related to inflammatory responses, and M2 phenotype is characteristic in more constructive repairing processes. Our hypothesis is that by modulating macrophage polarization inclining to M2 phenotype, better therapeutic outcome could be achieved. Therefore, we plan to add components from decellularized porcine urinary bladder (UBM digest) to our synthetic hydrogel, as UBM digest has been shown to promote M2 polarization of macrophages. On the other hand, as our injectable hydrogels are biodegradable, cells will slowly migrate into the gel injection sites. The current designs, even with MAA as an autocatalyzer for hydrogel degradation, do not allow cell infiltration and tissue integration prior to an adequate level of degradation. If we can positively induce the behavior of infiltrated cells, it may be more desirable to initiate cell infiltration before a significant amount of hydrogel mass loss. Inspired by porogen leaching method of creating porous structure in scaffold implants in vitro, we plan to mix sacrificial porogen particles prior to injections, thus leaving connective pores in the gel mass and hypothetically provide channels for cell migration shortly after injection. We expect the design combining both characteristics would accelerate the integration between material and tissue bed, and promote a more constructive foreign body response. A rat hindlimb muscle injection model would be employed to provide preliminary data for future porcine studies. The innovative method of fabricating porous injectable hydrogels may be transferred to other hydrogel systems and a wider spectrum of medical applications.

# 2.0 TAILORING THE DEGRADATION RATES OF THERMALLY RESPONSIVE HYDROGELS BY VARYING THE AUTOCATALYTIC POTENTIAL

## 2.1 INTRODUCTION

(Note: This chapter was previously published as: Y Zhu, H.B. Jiang, S.H. Ye, T. Yoshizumi, W.R. Wagner. Tailoring the degradation rates of thermally responsive hydrogels designed for soft tissue injection by varying the autocatalytic potential, Biomaterials. (2015) 484-493.)

Appropriate degradation behavior is essential for obtaining desired therapeutic outcomes in intramyocardial biomaterial injection for MI treatment [120-122]. Biomaterial degradation theoretically should be aligned with the pace of cell infiltration and neo-tissue formation to allow the structural and functional integration of myocardium with tissue developed in the injection site. Thermally responsive hydrogels have been widely studied for their amenability to minimally invasive delivery in the realms of drug delivery, embolization therapy, cell delivery vehicles, tissue fillers and wound dressings [123-125]. More recently, intramyocardial injection therapy has been pursued using mechanically strong thermally responsive hydrogels to inhibit pathological ventricular dilatation after myocardial infarction, a major contributor to morbidity

and mortality in ischemic cardiomyopathy [6-8]. As with other biomaterial applications where temporary mechanical support is the objective, the degradation behavior of thermally responsive hydrogels becomes a critical design consideration.

In seeking to control the degradation rate for a thermally responsive hydrogel that would be used in intramyocardial injection, several other design criteria must be considered. Basic requirements are acceptably low levels of cytotoxicity of the polymer and degradation products and adequate thermal response to allow needle-based injection and stiffening in situ. When tuning the degradation rate, one would ideally not impair the thermal sensitivity of the system or substantially alter the mechanical properties in the fluid or hydrogel state.

Polyesters, widely used as biodegradable polymers in general, have been utilized as a hydrophobic component in thermally responsive hydrogels to trigger dissolution and absorption of the hydrogels upon ester cleavage [126-128]. Polyester materials degrade faster under low pH conditions due to catalyzed hydrolysis [129]. The accumulation of acidic degradation products can lead to an autocatalytic effect, accelerating the hydrolysis of ester bonds [130-132]. It was anticipated that the autocatalysis effect could be employed to tune degradation rates across wide ranges. Thus, in this study the amount of acid in a thermally responsive copolymer backbone was varied to modulate the degradation rate of a poly(N-isopropylacrylamide) based hydrogel, poly(NIPAAm-co-HEMA-co-MAPLA) (pNHM, copolymerized with N-isopropylacrylamide (NIPAAm), 2-hydroxyethyl methacrylate (HEMA) and methacrylate-polylactide (MAPLA)) [113]. The pendant hydrophobic MAPLA sidechains become acidic units upon hydrolysis, resulting in a higher transition temperature and eventual solubility of the copolymer, without backbone cleavage. Different molar ratios of methacrylic acid (MAA) were incorporated into the copolymer to obtain poly(NIPAAm-co-HEMA-co-MAPLA-co-MAA) (pNHMMj). The effect of

MAA on hydrogel degradation was studied as well as its effect on thermal and mechanical behavior. The cytotoxicity of pNHMMj hydrogels and their degradation products were evaluated and an in vivo degradation study of pNHMMj hydrogels was performed in a rat hindlimb injection model.

## 2.2 MATERIALS AND METHODS

### 2.2.1 Materials

All chemicals were purchased from Sigma-Aldrich unless otherwise stated. N-isopropylacrylamide (NIPAAm) was purified by recrystallization from hexane and vacuum-dried. 2-Hydroxyethyl methacrylate (HEMA) was purified by vacuum distillation. Lactide, benzoyl peroxide (BPO), sodium methoxide ($NaOCH_3$), methacryloyl chloride, methacrylic acid (MAA) and other solvents were used as received.

### 2.2.2 Synthesis of methacrylate polylactide (MAPLA)

The synthesis of methacrylate polylactide was performed as previously described [113]. Briefly, $NaOCH_3$/methanol was added to a lactide/dichloromethane solution to synthesize polylactide (HO-PLA-OCH3) through ring-opening polymerization. MAPLA was synthesized by dropping methacryloyl chloride into a HO-PLA-$OCH_3$/dichloromethane solution containing triethylamine. Dichloromethane was removed by rotary evaporation and the product was purified by flash chromatography to obtain MAPLA with yields of ~60%.

### 2.2.3 **Synthesis of poly(NIPAAm-co-HEMA-co-MAPLA-co-MAA)**

Poly(NIPAAm-co-HEMA-co-MAPLA-co-MAA) (pNHMMj) copolymers were synthesized from NIPAAm, HEMA, MAPLA and MAA by free radical polymerization. The feed ratios of NIPAAm, HEMA, MAPLA and MAA were 80/(10-j)/10/j, where j = 0, 0.5, 1, 2, 5, 10 **(Scheme 2-1)**. Monomers (0.066 mol) were dissolved in 180 mL of 1,4-dioxane containing 0.23 g BPO. The polymerization was carried out at 75°C for 20 h under argon protection. The copolymer was precipitated in hexane and further purified by precipitation from THF into diethyl ether and vacuum-dried, with yields of ~80%. Fluorescently labeled copolymers were synthesized using the same reaction conditions with fluorescein O-methacrylate added at a feed ratio of an additional 2%, with all of the other monomer molar ratios remaining constant and j=0. Fluorescently labeled hydrogels used in the in vivo study were prepared by dissolving 14.25 wt% unlabeled copolymer with 0.75 wt% labeled copolymer in PBS.

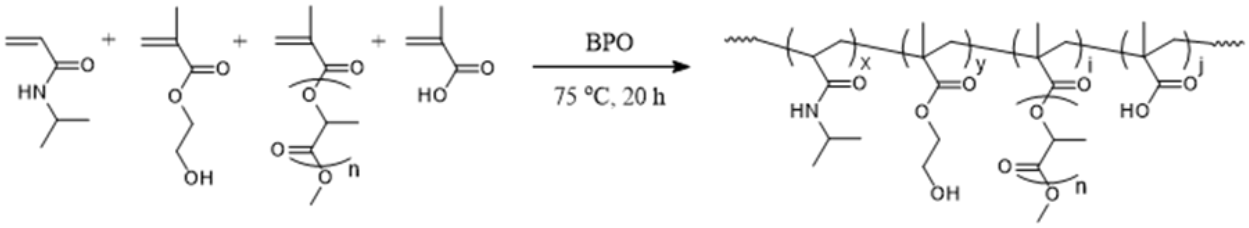


| MAA feed ratio (%) | Feed ratio (%) | | | |
|---|---|---|---|---|
| | NIPAAm | HEMA | MAPLA | MAA |
| 0 | 80 | 10 | 10 | 0 |
| 0.5 | 80 | 9.5 | 10 | 0.5 |
| 1 | 80 | 9 | 10 | 1 |
| 2 | 80 | 8 | 10 | 2 |
| 5 | 80 | 5 | 10 | 5 |
| 10 | 80 | 0 | 10 | 10 |

**Scheme 2-1.** (a) Synthesis of poly(NIPAAm-co-HEMA-co-MAPLA-co-MAA). (b) Feed ratio of monomers.

### 2.2.4 **Characterization**

$^{1}$H NMR spectra of pNHMMj were recorded with a 600 MHz Bruker spectrometer using CD3Cl as a solvent. Molecular weight of the copolymers was determined by gel permeation chromatography (GPC, Waters Breeze System, Waters 1515 HPLC Pump, Waters 2414 differential refractometer). The copolymers were dissolved in THF at a concentration of 1 mg/mL and the GPC analysis was performed at 35°C. A poly(methyl methacrylate) standard kit (Fluka, ReadyCal Set $M_p$ 500-2700000) was used for molecular weight-elution volume calibration.

Rheology studies were conducted on a TA Instruments rheometer (AR2000) to observe viscosity changes in the hydrogels during the temperature induced sol-gel transition. The polymer solutions (15 wt% in PBS) were placed between two parallel plates. With a temperature sweep from 5 to 35°C and a heating rate of 5°C /min, the shear storage modulus G' and the loss modulus G" were collected as a function of temperature at a fixed strain of 2% and a frequency of 1 Hz.

To measure the mechanical properties of the hydrogels, samples were incubated in a 37°C water bath for 24 h to reach a stable water content, and then the solid hydrogels were cut into rectangular strips 1 mm thick, 4 mm wide, and 25 mm long and then loaded in a water bath equilibrated to 37 °C. An ElectroForce 3200 Series II (Bose, Minnesota, US) equipped with a 2.5 N load cell was utilized to record the tensile stress-strain curve immediately after the samples were taken out of the water bath.

Hydrogel degradation was quantified by mass loss measurements. Hydrogels with known initial dry masses (~60 mg) were immersed into 6 mL of PBS at 37°C. At predefined time points over a 28 week period the hydrogels (n=3 each) were lyophilized and the relative mass loss was

recorded. The pH of the supernatant during degradation was measured with an Accumet pH meter (Fisher Scientific, Waltham, MA). To compare the relative pH inside pNHMMj hydrogels, polymers were dissolved in PBS containing 2.5 μM LysoSensor Yellow/Blue DND-160 pH-sensitive dye (Life Technologies, Grand Island, NY, US). After gelation, the excess fluid was removed and replaced with PBS. The hydrogels were allowed to stabilize for 1 d before being placed in a plate reader with excitation at 360 nm and emission intensities at 440 nm and 540 nm measured for the hydrogel surface and cross sections (cut and exposed). The cross sections were used to semi-quantitatively determine whether there was detectably lower pH in the hydrogel interior.

### 2.2.5 **Cytotoxicity of degradation products**

The cytotoxicity of the pNHMMj degradation products was assessed by measuring the relative metabolic activity of rat vascular smooth muscle cells (SMCs) cultured in Dulbecco's modified Eagle medium (DMEM) (Gibco, Life technologies) with 10% fetal bovine serum (FBS), 1% penicillin/streptomycin, and supplemented at 10% with hydrogel degradation solution, as previously described [62, 113]. The hydrogel degradation solution was prepared from incubation of the hydrogel in PBS. Culture medium with PBS added at 10% was used as a negative control. SMCs were seeded at an initial density of 30000/cm$^2$ and their metabolic activity was measured (n=6 each) using an MTS assay kit (Promega CellTiter 96 Cell Proliferation Assay). To qualitatively verify the results of the above test, cells were also observed under fluorescence microscopy after live/dead staining with a Promokine Live/Dead Cell Staining Kit.

### 2.2.6 **Viability of cells encapsulated in pNHMMj hydrogels**

SMCs labeled with the live cell marker CellTracker Red CMTPX (Life Technologies, Grand Island, NY) were suspended in PBS at a density of $2\times10^7$/mL. A total of 0.25 mL of this cell suspension was then added into 1 mL of the hydrogel solutions at 4°C. The mixture was thoroughly mixed before being transferred into a 37°C water bath for gelation. The supernatant was removed and replaced with culture medium (DMEM supplemented with 10% FBS, and 1% penicillin/streptomycin). The medium was changed every 3 d. After 1 and 7 d of culture, samples were taken out and cut into 100 μm thick sections and observed directly under fluorescence microscopy (Eclipse Ti-U, Nikon Instruments). At 7 d another set of samples were cooled at 4°C to release the encapsulated cells and these released SMCs were then cultured on TCPS for an additional 7 d to qualitatively assess their ability to proliferate. In a separate set of experiments, unstained SMCs were encapsulated as described above and upon recovery from the hydrogels by cooling at 1 and 4 d were stained with trypan blue solution and the percentages of live cells were calculated by manual counting of multiple microscopic fields for 3 independent samples for each hydrogel type.

### 2.2.7 **In vivo hydrogel injection studies**

Adult female Lewis rats weighing 160−210 g were utilized in a protocol that followed the National Institutes of Health guidelines for animal care and that was approved by the University of Pittsburgh's Institutional Animal Care and Use Committee. Anesthesia was induced with 3.0% isoflurane inhalation with 100% oxygen followed by 1.5-2% isoflurane with 100% oxygen during procedure. Dermatotomy was performed to expose the inner thigh muscles on both legs.

Single injections of 200-250 uL of hydrogel (fluorescently labeled or unlabeled) were made approximately 3 mm deep in the muscle bed. For each hydrogel, 6 injections in 6 legs were made (4 labeled, 2 unlabeled). Inner thigh muscles from 2 legs of the labeled groups were excised 3 min after injection. The muscles were incised to expose the hydrogels, and images were taken with a Dino-Lite (AM4113T-GFBW, AnMo Electronics, New Taipei City, Taiwan) under brightfield and fluorescence mode. After 21 d, rats were sacrificed and the inner thigh muscles encompassing the hydrogels were excised, images taken and the tissue was fixed in 10% formaldehyde for 3 d before embedding. H&E staining (for unlabeled hydrogels) and immunohistochemical staining (with labeled hydrogels) with monoclonal antibodies against CD68 (1:100, Abcam) was performed. Nuclei were stained with 40',6-diamidino-2-phenylindole (DAPI; 1:10000, Sigma). Microscopic images were taken under fluorescence microscopy and assessed with ImageJ.

### 2.2.8 **Statistical analyses**

For the paired comparisons of **Figure 2-2**, a paired t-test was employed. Where three or more groups were being compared, one-way ANOVA was employed with Tukey's test applied for specific comparisons. Results are presented as the mean with standard deviation. Statistical significance was defined as $p < 0.05$.

## 2.3 RESULTS

### 2.3.1 MAA content in the pNHMMj hydrogels

The incorporation of MAA into the hydrogels was confirmed by NMR as the -COO**H** peak appeared at ~12 ppm on the $^{1}$H spectrum, as shown in **Figure 2-1a**. The content of MAA in the copolymer calculated with peak areas shows a linear increase with the MAA feed ratio, (**Figure 2-1b**) although this content is ~40% lower than the MAA feed ratio in the reaction system. This result was also confirmed with minor discrepancies from the NMR results by titrating the -COOH groups in the copolymer with HCl/NaOH for protonation/deprotonation (**Figure 2-1b**). GPC results showed that the molecular weights $M_w$ of the pNHMMj copolymers were all between 22000 and 26000 g/mol.

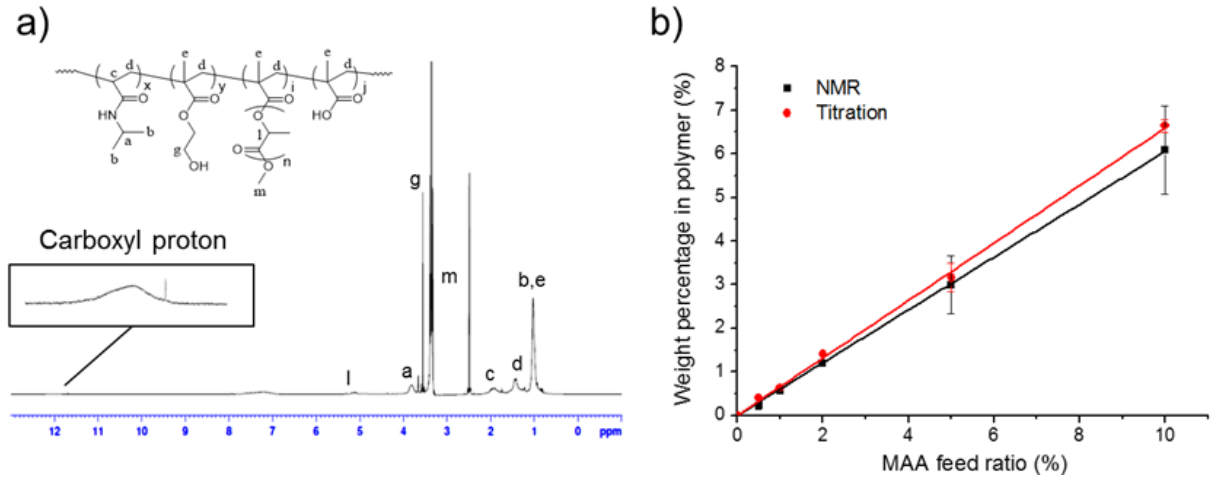


**Figure 2-1.** (a) $^{1}$H NMR spectra of pNHMM2. (b) MAA weight percentages in copolymers as determined by NMR and acid titration.

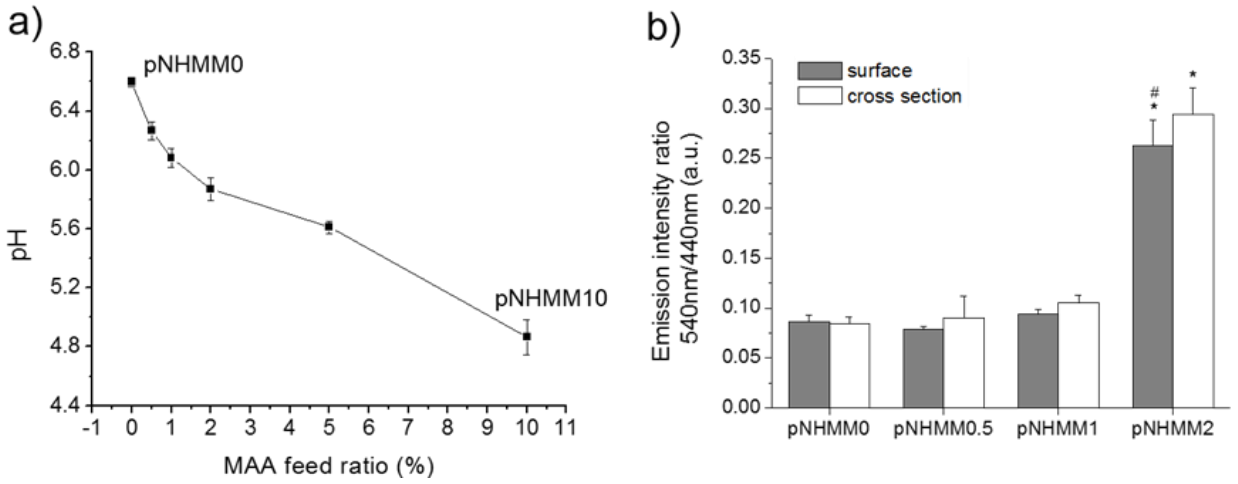


**Figure 2-2.** (a) pH of supernatants of pNHMMj hydrogels after gelation. (b) Fluorescent emission intensity ratio between 540 nm and 440 nm of pNHMMj hydrogels mixed with LysoSensor pH-sensitive dye, excited at 360 nm. A higher ratio reflects a lower pH. Data of pNHMM5 and pNHMM10 were not available due to fast degradation. * and # indicate significant differences between and within groups, respectively. * Significant differences compared to pNHMM0, pNHMM0.5, pNHMM1, $p$ <0.05. * Significant differences within pNHMM2 group, $p$ <0.05.

### 2.3.2 **Degradation and dissolution of pNHMMj hydrogels**

The pH of the supernatant solution after gelation of the pNHMMj polymers in PBS buffer (15 wt% of copolymers) showed that with increased MAA content in the copolymer, the more acidic the initial degradation environment was for PLA side chains in this limited volume system, **Figure 2-2**. Measured immediately after changing PBS, the supernatant pH for all pNHMMj increased, and showed no significant difference compared to the pH of PBS. After stabilization for 24 h to allow diffusion, the supernatant pH of pNHMM0, pNHMM0.5 and pNHMM1 remained above 7.3, whereas the pH for pNHMM2 dropped below 7.1 (**Figure 2-3**, pNHMM5 and pNHM10 degraded too quickly for this measurement). After another cycle of PBS change and measurement after another 4 d, the pNHMM2 continued to be able to reduce the pH versus the

other hydrogels. On the other hand, after gelation and placement in fresh PBS, followed by 24 h stabilization, the pH was lower in and on the surface of pNHMM2 hydrogel compared to pNHMM0, pNHMM0.5 and pNHMM1, as indicated by a pH-sensitive dye (LysoSensor, whose emission intensity ratio between 540 nm and 440 nm increases as pH decreases). In addition, the pH of the interior of the pNHMM2 hydrogel was lower than the pH on the surface. No significant differences were found among the other 3 polymer types (data not available for pNHMM5 and pNHMM10 due to rapid degradation).

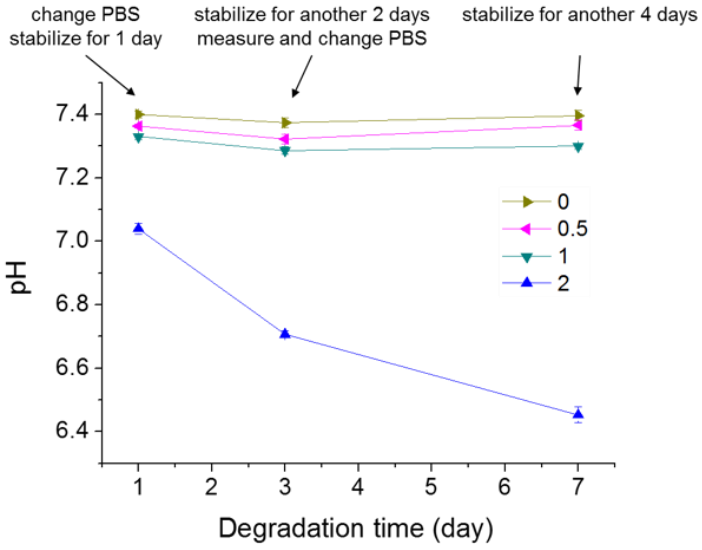


**Figure 2-3.** Change of supernatant pH during degradation of pNHMMj hydrogels in PBS.

The degradation rate increased significantly as MAA was added in increasing proportion into the polymer backbone, as shown by the weight loss profile of the hydrogels in PBS (**Figure 2-4)**. Without MAA, pNHMM0 needed over 5 mo to lose 50% weight in PBS, and the same loss required about 2 mo, 1 mo, 1 wk and 1 d for MAA containing copolymers with the MAA feed ratio at 0.5% (pNHMM0.5), 1% (pNHMM1), 2% (pNHMM2), 5% (pNHMM5) and 10%

(pNHMM10), as shown in **Figure 3b**. The temporal weight loss profiles of the pNHMMj hydrogels share a similar shape, which begins with a slow weight loss stage, followed by an abrupt decrease in remaining weight. Furthermore, when incubated in PBS solution at pH 9.5, the abrupt weight loss for MAA10 was postponed for 1 d (**Figure 2-5**). Since pNHMM5 and pNHMM10 hydrogels were considered to degrade too quickly for potential in vivo applications, hydrogels with less MAA were selected as candidates for further evaluation.

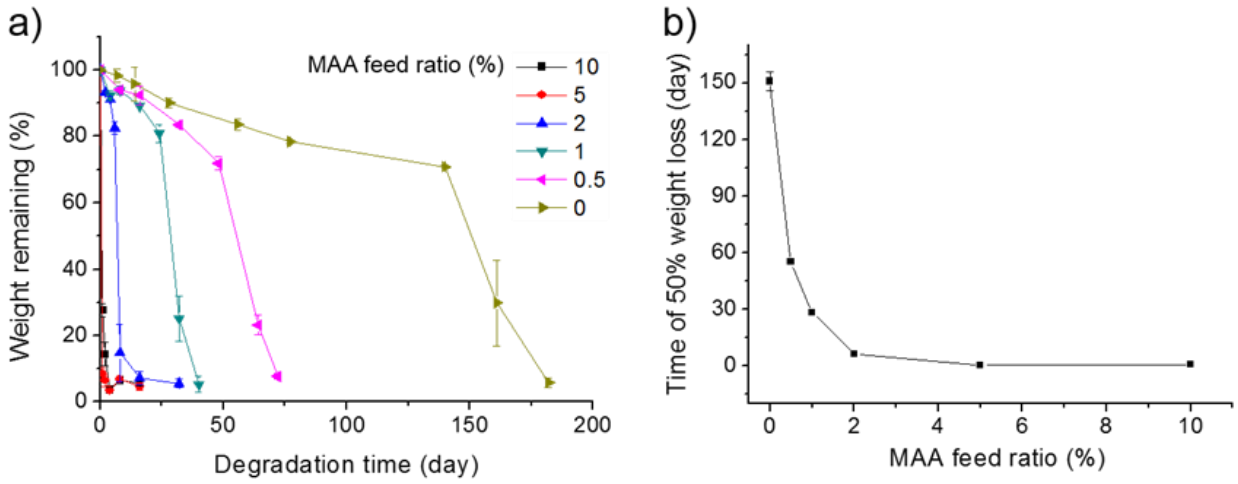


**Figure 2-4.** (a) Weight loss profiles of pNHMMj hydrogels. (b) Time for 50% weight loss derived from (a).

### 2.3.3 Thermal and mechanical behavior of pNHMMj hydrogels

The transition temperature of MAA hydrogels in PBS did not shift significantly as the MAA content in the polymer backbone was increased. As shown in **Figure 2-6a**, the rapid increase in shear modulus G' of pNHMM0, pNHMM0.5, pNHMM1 and pNHMM2 occurred within 17.5±2.5°C, which represents the sol-gel transition as temperature rises. Accompanying this mechanical transition the copolymers were observed to become optically opaque and form white gels. The abrupt increase in shear modulus or viscosity required only a few sec at 37°C, hence

when pNHMMj hydrogels were injected into PBS at 37°C, the response was rapid. As shown in **Figure 2-6b**, solution pH did not significantly affect the transition temperature of pNHMMj hydrogels, especially in the weak acidic range.

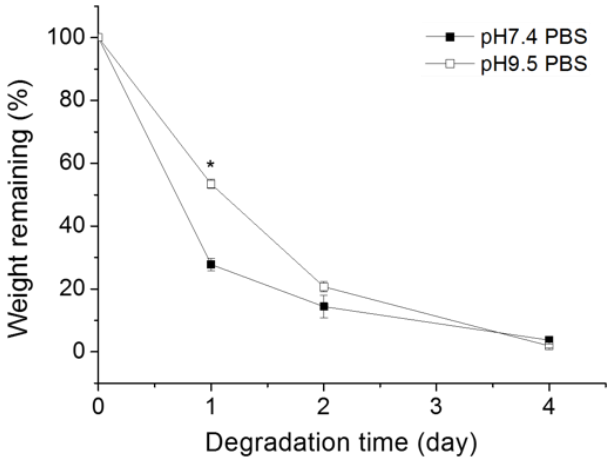


**Figure 2-5.** Weight loss of pNHMM10 incubated in regular PBS (pH 7.4) and basic PBS (pH 9.5, mediated by NaOH). * Significant difference, $p < 0.05$.

The Young's modulus of pNHMMj hydrogels were all above 200 kPa and did not vary significantly with increasing MAA content (**Figure 2-7**), indicating that the degradation or absorption rate for the hydrogels was decoupled from their initial mechanical stiffness in tension when the MAA content was low.

### 2.3.4 **Cytocompatibility of pNHMMj hydrogels and their degradation product**

As shown in **Figure 2-8a-d**, round single cells were evenly distributed when SMCs were encapsulated within the hydrogels. Using trypan blue to quantify viability, one day after

encapsulation, over 85% cells were alive in pNHMM0, pNHMM0.5, pNHMM1 gels, while less than 70% cells survived in pNHMM2 (**Figure 2-8i**). Viability was ~85% in pNHMM0, pNHMM0.5, pNHMM1 gels 4 d after encapsulation, while viability was less than 60% in pNHMM2 (**Figure 2-8i**). Qualitatively assessing cells stained with a viability marker at the time of encapsulation showed that after 1 and 7 d culture, viable cells remained spread throughout the hydrogels (**Figure 2-8e-h**). Cells isolated at 7 d and cultured on TCPS for 7 d qualitatively showed an ability to proliferate (**Figure 2-9**).

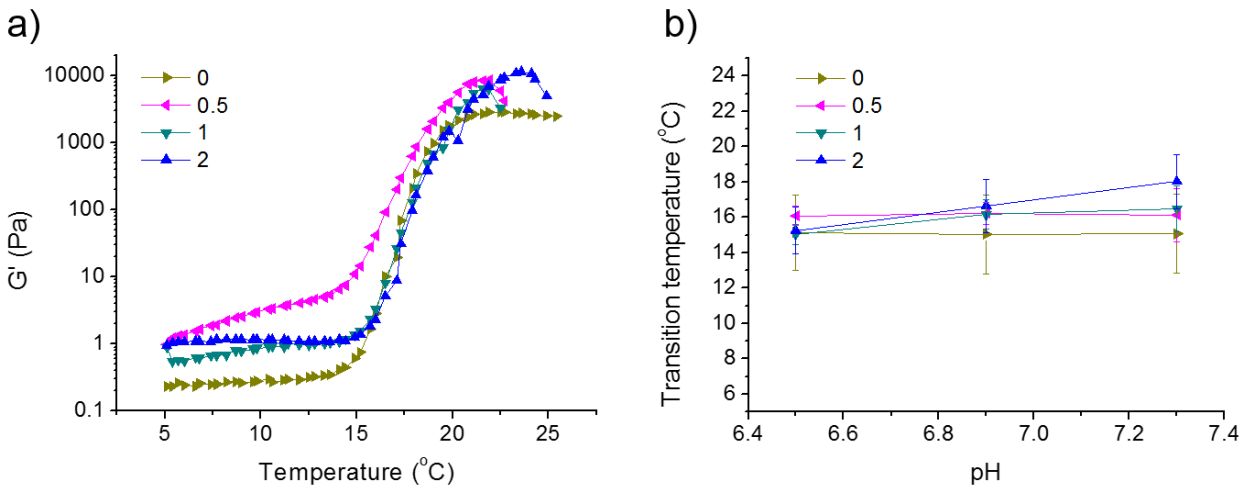


**Figure 2-6.** Transition temperature of pNHMMj hydrogels. (a) Temperature sweep of shear modulus (G') of pNHMMj hydrogels. (b) Transition temperature dependence on pH.

The cytotoxicity of the degradation products of pNHMMj hydrogels were also tested. Live/dead staining showed that rSMC proliferation was not impeded by any of the copolymer degradation products: overall metabolic activity of the cultures during the 7 d increased, suggesting cell proliferation, and few dead cells were observed after recovery and culture on

TCPS (**Figure 2-10a-o**). Slightly different from the findings from the encapsulation experiment, degradation products of the pNHMM2 hydrogel did not show higher cytotoxicity compared to its counterpart pNHMMj hydrogels (**Figure 2-10p**).

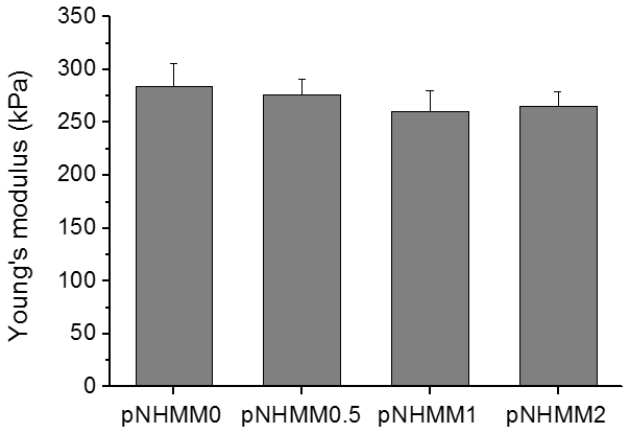


**Figure 2-7.** Young's modulus of pNHMMj hydrogels.

### 2.3.5 **In vivo degradation**

In vivo degradation and absorption of hydrogels was tested in rat hindlimb muscles. Hydrogels solidified immediately upon being injected into the muscles and formed distinct volumes, displacing the muscle tissue, as shown in the left columns of **Figure 2-11**. Fluorescent imaging revealed that the hydrogels formed well-defined regions, with minimal diffusion into the tissue. This effect was also demonstrated on immunohistochemical staining sections obtained from tissue immediately after injection (data not shown). After 21 d, the boundaries between injected hydrogels and the leg muscles were more diffuse compared to the time right after injection, particularly for pNHMM1 and pNHMM2, as shown in the right columns of **Figure 2-11**.

Fluorescent signals could still be observed, showing that the hydrogels were not completely absorbed. However, the fluorescence intensities were weaker in all four groups compared to the initial status. Unabsorbed hydrogels could be identified in immunohistochemical sections in all four groups as irregularly shaped regions encompassed by dense cell populations (**Figure 2-12a**). For most of the polymers these regions of injection had minimal or no fluorescence, while for the pNHMM0 group this region was seen to have higher green fluorescence in large, continuous

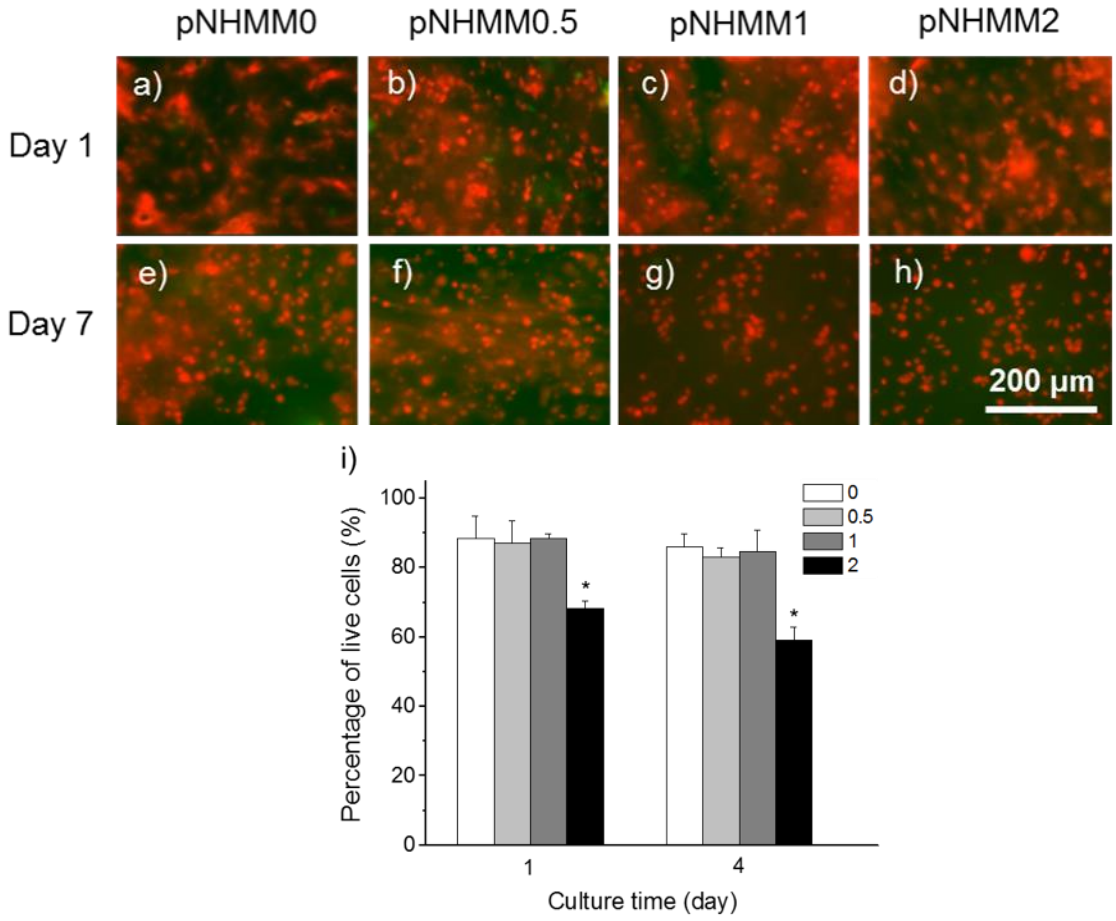


**Figure 2-8.** Viability of SMCs encapsulated in pNHMMj hydrogels. (a-h) live SMCs (red) stained with CellMarker in pNHMMj hydrogels 1 d and 7 d after encapsulation. Green: Fluorescein labeled hydrogels. (i) Percentage of live SMCs after 1 d and 4 d encapsulation in pNHMMj hydrogels, determined by trypan blue staining. * Significant differences, $p$ <0.05.

areas. The dense cell populations surrounding the polymers were CD68 positive and identified as macrophages (**Figure 2-12a,b**). For pNHMM0, pNHMM0.5 and pNHMM1 hydrogels, macrophages encompassed the materials, however, did not appear to infiltrate into the polymer. For the pNHMM2 group, macrophages infiltrated into the injection site, separating the remaining hydrogel volumes. Similar observation could be made on H&E stained sections. Macrophages gathered and formed capsules around injected hydrogels as shown in **Figure 2-12c**. Macrophages can be found in some regions of unabsorbed pNHMM2 hydrogel, migrating from the border zone. This was not observed with the other 3 polymer types.

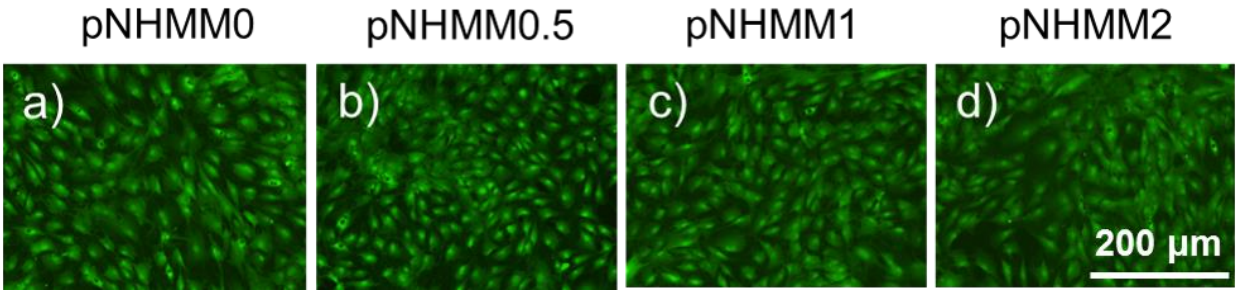


**Figure 2-9.** (a-d) SMCs cultured for another 7 d after retrieving from inside pNHMMj hydrogels and seeding on TCPS.

## 2.4 DISCUSSION

Different strategies have been reported to modulate the degradation of thermally responsive hydrogels. For poly(ethylene glycol)-poly(ε-caprolactone)-poly(ethylene glycol) (PEG-PCL-PEG), poly(ethylene glycol)-poly(lactide-co-glycolide)-poly(ethylene glycol) (PEG-PLGA-PEG) and similar block copolymer systems, changing the molecular weight of individual blocks and

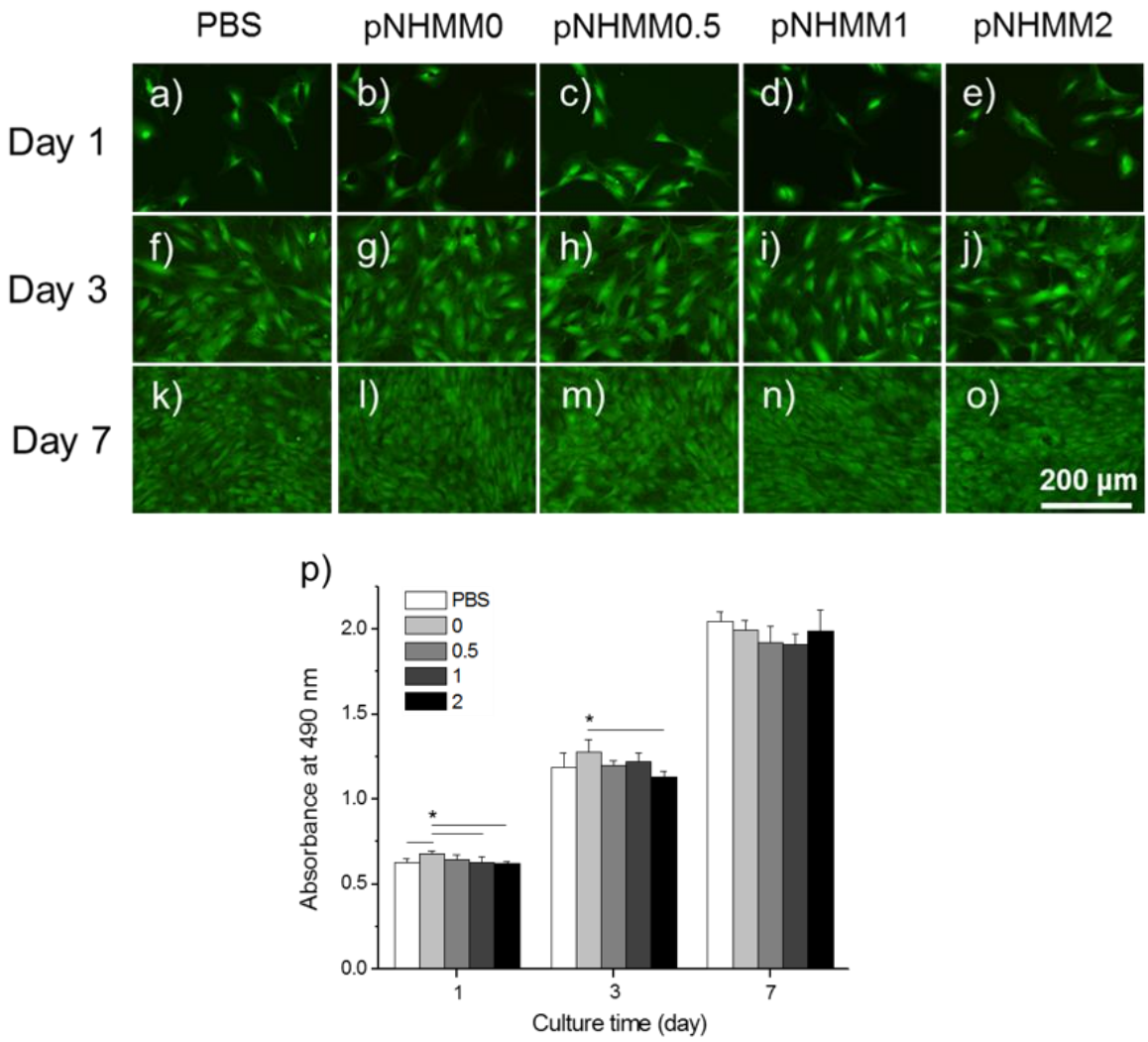


**Figure 2-10.** Cytotoxicity of degradation products of pNHMMj hydrogels. SMCs proliferation 1 d (a-e), 3 d (f-j), 7 d (k-o) after seeding determined by live/dead staining. (p) MTS assay of the SMCs cultured in the same conditions. * Significant differences, $p$ <0.05.

the molecular weight ratio between hydrophobic and hydrophilic blocks results in changes in degradation rate [133, 134]. For thermally responsive systems that employ crosslinking, adjusting the crosslinking density is effective [135]. In poly(N-isopropylacrylamide) based hydrogels, the content of hydrolytic pendant groups has been shown to have a significant

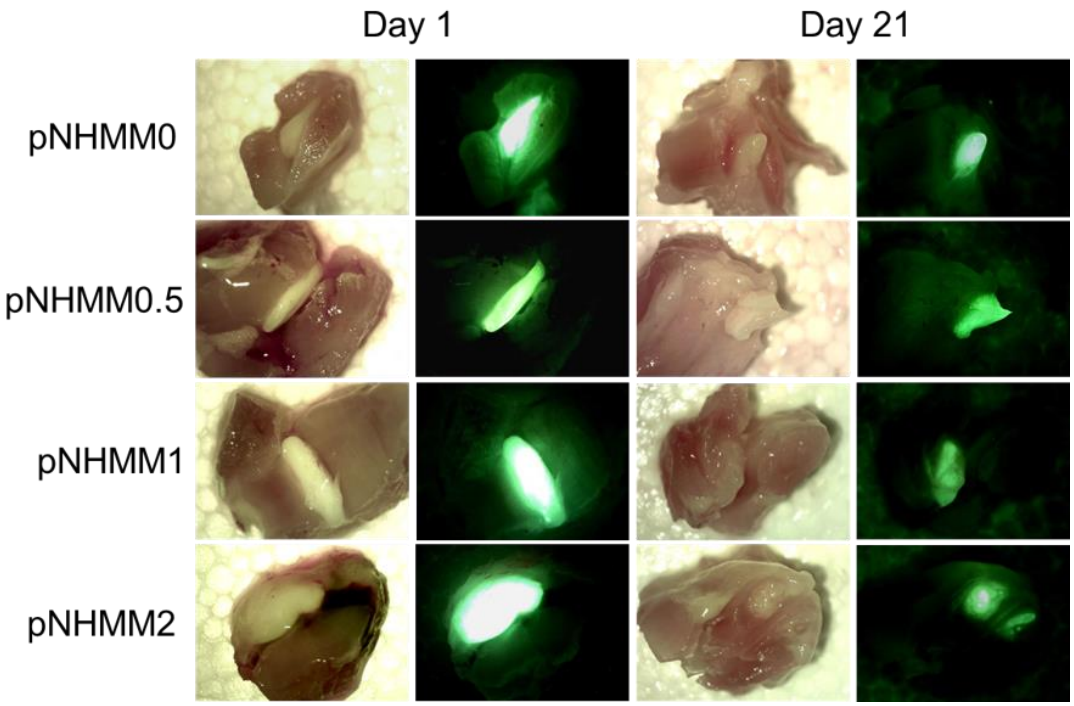


**Figure 2-11.** Bright field and fluorescent images of excised rat leg muscles injected with pNHMMj hydrogels. Left column: excised on the same day of injection. Right column: excised 21 d after injection. The white mass and green fluorescence indicate the hydrogel.

influence on both hydrogel degradation rate and thermal transition behaviors [136]. In other cases, introducing enzyme sensitive cleavage sites has proven an effective mechanism [137-139].

In this study, pNHMMj hydrogels were synthesized and displayed tunable degradation behavior in vitro and in vivo, supporting the design hypothesis that the addition of MAA as an autocatalyst for MAPLA hydrolysis would provide a method to accelerate the hydrogel dissolution. Manipulation of MAA content over a relatively small range resulted in widely varying degradation behavior, with 50% solubilization occurring in time frames from days to months, wider than what has been previously reported in the literature [113, 114, 140, 141]. The

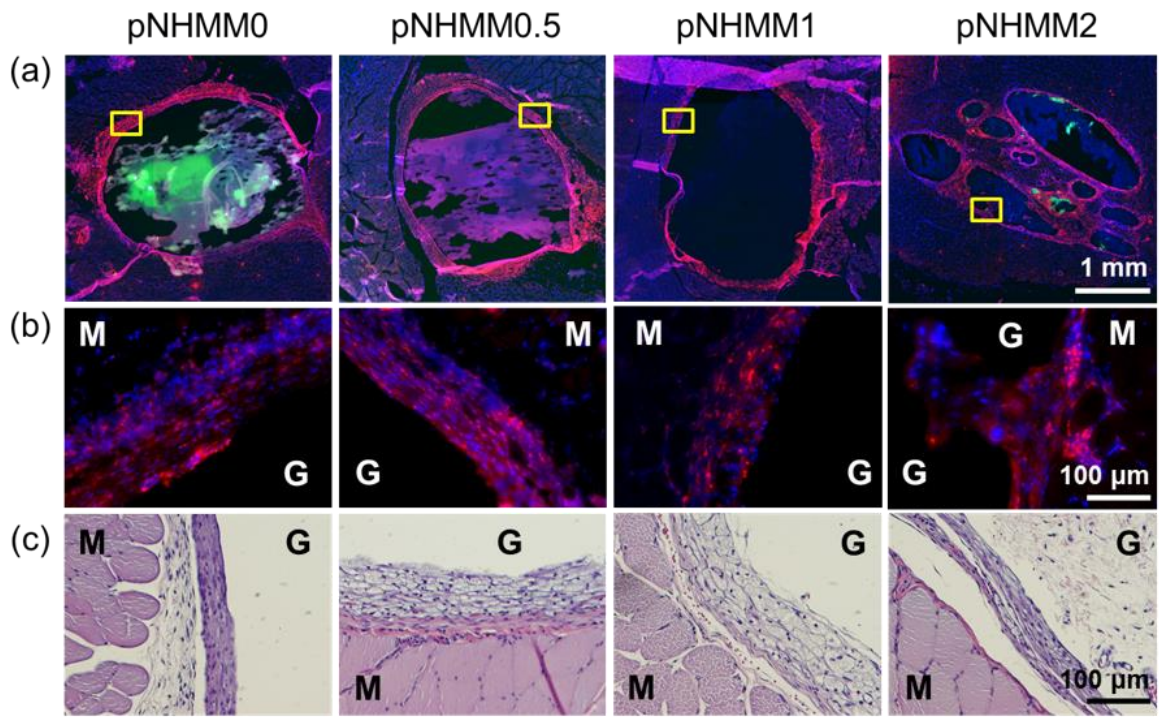


**Figure 2-12.** Immunohistochemical (row (a,b)) and H&E (row (c)) staining of rat hindlimb muscle injected with pNHMMj hydrogels 21 d after injection. In row (a) and row (b): Blue: DAPI for nucleus, Green: hydrogels, Red: CD68 for macrophages. Images in row (b) are enlarged from corresponding areas in row (a), as indicated by yellow rectangles (may be rotated). M indicates muscle and G indicates hydrogel.

lower pH of the supernatant immediately after gelation and after a series of PBS/medium changes and stabilization steps indicated that the proton concentrations were higher in the environment for pNHMMj hydrogels with higher MAA content, as expected. This result also corresponds with the pH being lower inside and on the surface of pNHMM2 compared to other pNHMMj hydrogels having less MAA content, since greater MAA content would be the source of extra protons which decreased the supernatant pH. In addition, the pH appeared to be lower inside pNHMM2 compared to the surface of the hydrogel, suggesting diffusion-driven depletion

of protons towards the surface of the hydrogel. The four pNHMMj hydrogels studied all experienced an abrupt mass loss at different times, indicating a rapid increase in hydrolysis rate and polymer hydrophilicity. This can be explained with the hindered diffusion of protons. As the proton concentration slowly builds up in the hydrogels, the autocatalytic effect would become stronger, leading to faster accumulation of cleaved lactic acid molecules and MAA residues, which in turn would contribute to a higher proton concentration. The fact that degradation of pNHMM10 (with highest MAA content among pNHMMj hydrogels) was slowed in weak basic buffer supports the proposed autocatalytic mechanism.

Hydrogel degradation was largely decoupled from both stiffness and thermal transition behavior, probably because the MAA content was too low to affect the dominance of NIPAAm and highly hydrophobic MAPLA effects on thermal transition, and increases in electrostatic repulsion between MAA residues was not consequential. Theoretically, the ionizable MAA residues should increase pNHMMj copolymer hydrophilicity and pH sensitivity. Peppas et al. systematically studied the thermal sensitivity and pH sensitivity of poly(NIPAAm-co-MAA) hydrogels [142-144]. They found that the thermal transition temperature increased from 32$^{o}$C to 34.5$^{o}$C as MAA in the poly(NIPAAm-co-MAA) hydrogels increased from 0 to 12 mol%; on the other hand, the swelling ratio of the poly(NIPAAm-co-MAA) hydrogels increased significantly between pH 5.3 and pH 5.7 [143]. The pH sensitivity was also observed in a poly(NIPAAm-co-MAA) interpenetrating polymeric network [144]. In the current study, the examined pH range (6.4-7.4) was narrow, corresponding to infarcted cardiac muscle as a potential application area. The pH range studied fell above the $pK_a$ of poly(methacrylic acid) as its effect on thermal transition behavior was studied for pNHMMj hydrogels containing small amounts of MAA. The

pH sensitivity was not significant in the examined range and phase change and mechanical behavior that were attractive for minimally invasive delivery could be maintained, while the degradation rate could independently be optimized for a given application.

As expected, the pNHMM2 hydrogel showed faster in vivo degradation and disappearance from the site of injection compared to the other three hydrogels studied. However, the in vivo degradation and absorption of hydrogels qualitatively appeared to be substantially slower than in vitro. Day 21 was chosen as an endpoint for the in vivo studies based on the in vitro weight loss curve, expecting that almost all of the pNHMM2 hydrogel and about 50% of the mass of the pNHMM1 hydrogel would have been lost. Furthermore, hydrogel mass loss was expected to potentially be faster in vivo if local enzymatic activity contributed to the degradation process. The explanation for the apparently slower hydrogel loss in vivo could be that the catalyzing effect of MAA content was somewhat weakened in vivo as the tissue served as a more effective buffering system relative to the PBS in vitro.

The fluorescence of the remaining injected hydrogels was diminished for the faster degrading hydrogels with higher MAA content (**Figure 2-12**). This result was in accordance with what was observed in vitro. It is known that fluorescein changes from a lactone form to neutral and cation forms under low pH, and its emission intensity and quantum yield drop significantly at ~490 nm [145]. After 21 d in PBS, the fluorescence intensity of the labeled hydrogel interior dropped significantly for pNHMM0.5 and pNHMM1 versus that measured immediately after gelation, whereas the fluorescence intensity of pNHMM0 remained unchanged (**Figure 2-13**). This result would explain the relatively strong green fluorescence only being observed for the pNHMM0 hydrogel after 21 d in vivo (**Figure 2-12**), suggesting that the hydrogel interiors were more acidic for the other three studied hydrogels.

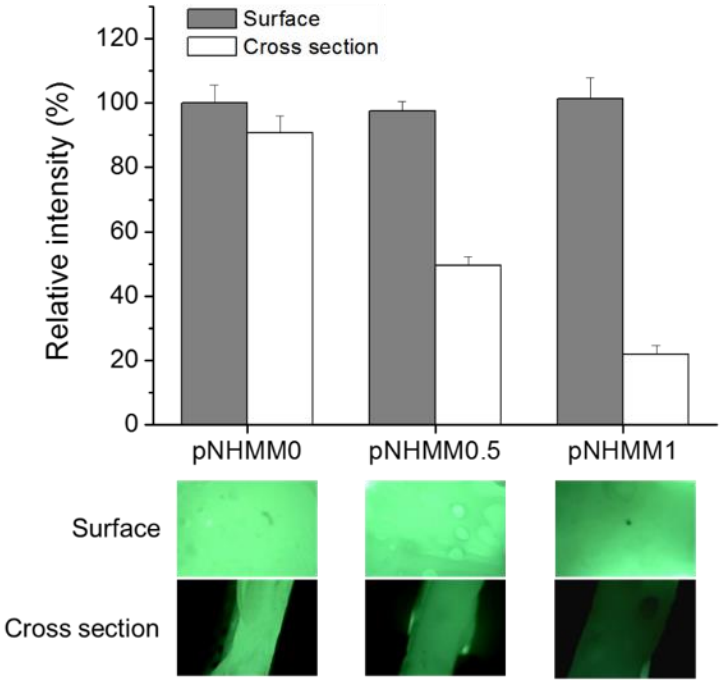


**Figure 2-13.** Surface and cross section fluorescent intensities of fluorescein-labeled pNHMMj hydrogels after 21 d in PBS (with PBS exchange) shown as percentages of the initial intensities immediately after gelation. Data for pNHMM2 were not available due to fast degradation. Photos taken by Dino-Lite, intensities measured with ImageJ from images. Scale bar = 2 mm.

The foreign body response induced by the pNHMMj hydrogels 21 d post injection was characterized by local macrophage recruitment, as is typical of the foreign body response [118]. The macrophages mainly distributed around the hydrogel mass, forming an encompassing cell layer. Few foreign body giant cells could be observed. For the slow degrading pNHMM0, pNHMM0.5 and pNHMM1 hydrogels, the macrophages did not infiltrate or separate the hydrogel mass, as opposed to the findings with pNHMM2, where the hydrogel was fragmented and the pieces surrounded by macrophages. This suggested that the in vivo absorption of

pNHMMj hydrogels is not simply characterized by surface mass loss, but that degradation and solubilization occurs across the hydrogel with fragmentation. This fragmentation was observed in all cases in vitro, with fragmentation not occurring until the rapid phase of mass loss began.

The principle of manipulating acid autocatalysis may apply for controlling degradation rates for other thermally responsive hydrogels, and more broadly, biomaterials whose degradation is based on polyester hydrolysis. Ara et al. blended calcium compounds with different acidity with PLGA and found that the most basic calcium carbonate was most effective in delaying the degradation, while the most acidic calcium dihydrogenphosphate was least effective [146]. Similar buffering effects on autocatalysis were also found by Zhang et al., where basic magnesium carbonate and magnesium hydroxide significantly decreased the degradation rate of PLGA films while neutral sodium chloride and zinc sulfate did not show comparable influence [147]. Wu et al. have shown experimental results suggesting that pore morphology affects the diffusion of acidic degradation products from PLGA scaffolds, thus directly impacting the extent of acid catalyzed hydrolysis and degradation rate [148]. For pNHMM hydrogels, the mass loss curves were characterized by rapid degradation following early periods of slower change, similar to the behavior of several other polyester materials [149-151]. The autocatalytic mechanism might readily be applied to the design and synthesis for current material systems to introduce a tunable means of increasing degradation. For example, it is reasonable to assume that adding a small portion of pendant carboxyl groups onto PEG-PCL-PEG, PCL-PEG-PCL, or PEG-PLGA-PEG hydrogels could accelerate degradation, although such a design might also be dependent upon the overall hydrophilicity of the modified polymer system. Of note, a synthetic route to fabricate PCL-PEG-PCL copolymer bearing pendant carboxyl groups on the PCL blocks has been reported by Lavasanifar et al [152]. The degradation rate of thermally responsive

hydrogels has been studied and utilized to control the release of pharmaceutical agents and proteins [153, 154]. The potential of thermally responsive hydrogels as cell carriers has been demonstrated as well [155-158]. Given that hydrogel degradability significantly influences cell proliferation, migration and differentiation [159-162], along with the therapeutic outcomes of injection therapies [77, 163, 164], adding acid to tune the degradability of thermally sensitive hydrogels is attractive.

One key advantage of the strategy employed here is that relatively small amounts of catalyst (acid) did not significantly influence the material properties of interest. However, there are potential limitations and drawbacks of this strategy. First, for the acid to play its role, a certain level of diffusion and access of protons to the ester bonds is needed, which in turn is dependent on the water content in the hydrogel. The accelerating effect may not be as readily achieved for more hydrophobic materials, particularly in the early stages of degradation. Also, for injectable hydrogels, the catalyzing effect may vary across injection sites under the influence of buffering capacity. Second, an acidic microenvironment would be generated for faster degradation to take place, which would also lower the pH for the cells and corresponding physiological events in the vicinity of the implant. This was not explicitly studied in this report, but the histological results did not suggest an obvious effect for the healthy skeletal muscle bed examined.

## 2.5 CONCLUSION

A series of NIPAAm based thermally responsive polymers (pNHMMj) were synthesized, which contained varying MAA content. By releasing protons that catalyzed ester hydrolysis, MAA

accelerated the degradation and adsorption of the hydrogels both in vitro and in vivo, and this effect was positively correlated to MAA content in the copolymer. The thermal transition behavior and mechanical strength did not significantly vary among the pNHMMj hydrogels. On the other hand, the pNHMMj hydrogels showed low cytotoxicity and appeared to induce a mild foreign body response. Therefore, pNHMMj hydrogels are ideal candidates to study the influence of degradation rates of biomaterial on the therapeutic effect of intramyocardial injection treatment for MI. The introduced autocatalysis strategy of tuning the degradation of thermally responsive hydrogels where degradation or solubilization is determined by their polyester components might be applied to other tissue engineering and regenerative medicine applications where appropriate biomaterial degradation behavior is needed.

# 3.0 TAILORING THE HYDROPHILICITY OF THERMALLY RESPONSIVE HYDROGELS TO COUPLE WITH ROBOTIC SYSTEM FOR MINIMALLY INVASIVE DELIVERY

## 3.1 INTRODUCTION

(Note: This chapter was previously published as: Y. Zhu, N.A. Wood, K. Fok, T. Yoshizumi, D.W. Park, H. Jiang, D.S. Schwartzman, M.A. Zenati, T. Uchibori, W.R. Wagner, C.N. Riviere, Design of a Coupled Thermoresponsive Hydrogel and Robotic System for Postinfarct Biomaterial Injection Therapy, Ann. Thorac. Surg. (2016) 780-786.)

One of the advantages of hydrogel injection therapy is its potential to be delivered in a minimally invasive fashion, for instance Seif-Naraghi et al. successfully injected extracellular matrix-derived hydrogel through a percutaneous transendocardial intervention and Leor et al. delivered alginate by intracoronary infusion, both in pig models [30, 165]. Both techniques approach the injection sites by catheter originating through a femoral artery access site. No remote infarction or embolization was reported in either pig model, however there are theoretical safety concerns associated with the potential for hydrogel leakage into the circulatory system.

In this study we developed an alternative option for minimally invasive delivery of a hydrogel to the LV wall without entrance into the circulatory system, and reduction of concerns

with hydrogel regurgitation into the circulating blood volume. An injection strategy facilitated by the coordinated design of a thermoresponsive hydrogel and a robotic injection device employing local temperature control is described. A biodegradable, thermoresponsive hydrogel was synthesized and its thermal behavior was modulated to facilitate robotic injection. A previously reported robotic system (HeartLander [166]) was modified to incorporate a fluid cooling system and injection pathway redesign to provide the capacity of delivering thermally sensitive materials. Injections were attempted in a pig model through a subxiphoid transepicardial approach with a predefined injection pattern and depth, to show the precision and efficacy of the strategy.

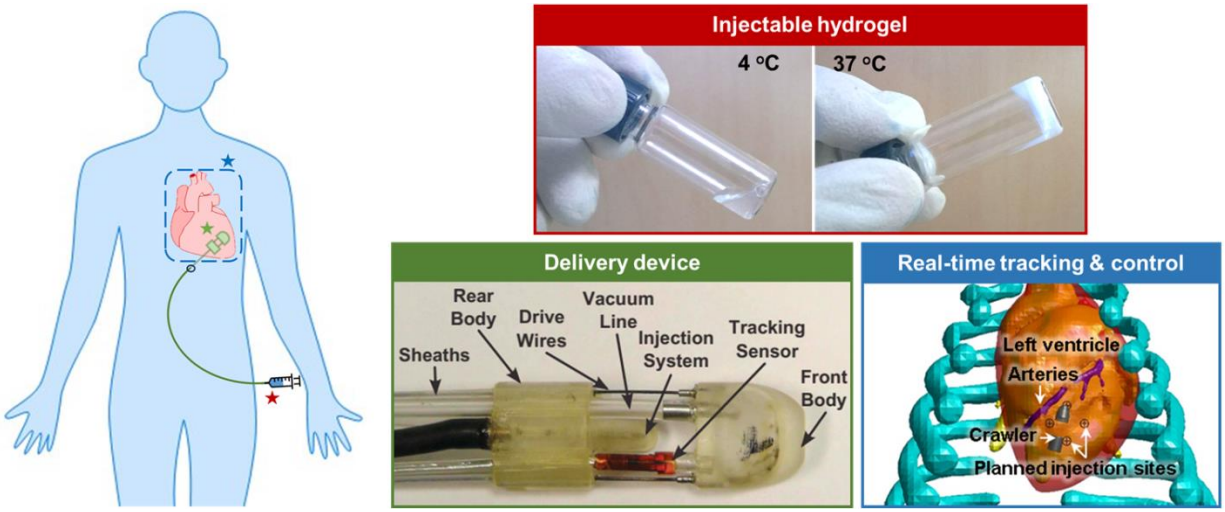


**Scheme 3-1.** Subxiphoid transepicardial injection of thermoresponsive hydrogel for myocardial injection therapy.

To effectively deliver the thermoresponsive hydrogel three efforts were coordinated, as shown in **Scheme 3-1**. The first component was the design of the injectable hydrogel, thermoresponsive poly(NIPAAm-co-VP-co-MAPLA) (NIPAAm: N-isopropylacrylamide, VP: N-vinylpyrrolidone, MAPLA: methacrylate-polylactide) which gels from a low viscosity

solution as the temperature increases to 37˚C. The second component was the modification of the robotic injection system to effectively cool the hydrogel solution, crawl on a beating heart and make injections in a controlled manner. The third component was the real-time tracking system that maps the 3D structure of the working field and localizes the robotic injection system to guide the crawler to the desired positions while avoiding major blood vessels. During the procedure, small subxiphoid and pericardial incisions allow access of the crawler head region to the LV epicardial wall, and the hydrogel is injected extracorporeally. The polymer solution is kept cool by a coaxial cooling fluid pathway up to the point of injection where the injected material undergoes phase transformation within the targeted region of the LV wall.

## 3.2 MATERIALS AND METHODS

### 3.2.1 Materials

All chemicals were purchased from Sigma-Aldrich. N-isopropylacrylamide (NIPAAm) was purified by recrystallization from hexane and vacuum-dried. N-vinylpyrrolidone (VP), lactide, benzoyl peroxide (BPO), sodium methoxide ($NaOCH_3$), methacryloyl chloride, methacrylic acid and other solvents were used as received.

### 3.2.2 Synthesis of methacrylate polylactide (MAPLA)

The synthesis of methacrylate polylactide was performed as previously described [113]. Briefly, $NaOCH_3$/methanol was added to a lactide/dichloromethane solution to synthesize polylactide

(HO-PLA-$OCH_3$) through ring-opening polymerization. MAPLA was synthesized by dropping methacryloyl chloride into a HO-PLA-$OCH_3$/dichloromethane solution containing triethylamine. Dichloromethane was removed by rotary evaporation and the product was purified by flash chromatography to obtain MAPLA with yields of ~60%.

### 3.2.3 **Synthesis of poly(NIPAAm-co-VP-co-MAPLA)**

Poly(NIPAAm-co-VP-co-MAPLA) copolymers were synthesized from NIPAAm, VP and MAPLA by free radical polymerization. The feed ratios of NIPAAm, VP and MAPLA were 80/j/(20-j), where j = 10, 15, 17.5, 20, and the corresponding product polymers were named as VPj, e.g. VP10. Please find supporting information for details of polymer synthesis. For photoacoustic imaging described below, 48 μg/mL indocyanine green (ICG) was dissolved in VP15 hydrogel before injection.

### 3.2.4 **Characterization**

$^1H$ NMR spectra of poly(NIPAAm-co-VP-co-MAPLA) copolymers were recorded with a 600 MHz BRUKER spectrometer using $CD_3Cl$ as solvent.

Rheology studies were conducted on a TA Instrument rheometer (AR2000) to observe the mechanical property change of the hydrogels during the temperature induced sol-gel transition. The polymer solutions (15 wt % in PBS) were placed between two parallel plates. The heating rate was 5 oC/min, the shear storage modulus G' and the loss modulus G" were collected as a function of temperature at a fixed strain of 2% and a frequency of 1 Hz.

To measure the transition time of hydrogels in 37°C air, 150 uL of each type of hydrogel was added to a pre-cooled (0°C) 96-well plate and placed in a plate reader that was pre-warmed to and set at 37°C. Absorbance at 490 nm was recorded for 15 min.

VP10 and VP15 degradation was quantified by mass loss measurements. Hydrogels with known initial dry masses (~60 mg) were immersed into 6 mL of PBS (replaced weekly to maintain a constant pH value of 7) at 37°C. At predefined time points over a 10 w period the hydrogels (n=3 each) were lyophilized and the relative mass loss recorded.

Adult female Lewis rats (3 rats each for VP10 and VP15) weighing 160−210 g were utilized in a protocol that followed the National Institutes of Health guidelines for animal care and that was approved by the University of Pittsburgh's Institutional Animal Care and Use Committee. Anesthesia was induced with 3.0% isoflurane inhalation with 100% oxygen followed by 1.5-2% isoflurane with 100% oxygen during procedure. Dermatotomy was performed to expose the inner thigh muscles on both legs. Single injections of 200-250 uL of VP15 hydrogel were made approximately 3 mm deep in the muscle bed. After 28 d, rats were sacrificed and the inner thigh muscles were excised and fixed in 10% formaldehyde for 3 d before embedding. H&E staining and immunochemistry staining of CD68 was performed.

### 3.2.5 **Robotic injection system modified with cooling line**

Modifications to an existing HeartLander injection robot [167] were made to accomodate the dual lumen cooled injection system, including moving the injection channel to the rear foot and widening the robot from 8 to 9.85 mm. These modifications minimized the effect of increased tether stiffness on robot mobility. The cooled injection system consisted of inner and outer

polytetrafluoroethylene (PTFE) tubes of 23 and 17 gauge respectively. A diagram of the modified robot and injection system is shown in **Figure 3-3a,** with the constructed robot shown in **Scheme 3-1**.

### 3.2.6 Simulation model

The implemented model was a 2D axisymmetric model with an overall length of 0.30 m. The inner channel dimensions assumed the nominal dimensions of 23 gauge PTFE Light Wall Tubing (inner diameter (ID) = 0.66 mm, wall thickness (WT) = 0.15 mm), while the outer channel dimensions were varied to correspond to 15 and 17 gauge PTFE Light Wall Tubing. The hydrogel was modelled as a stationary solid, while the cooling fluid was modelled as liquid water. Constraints and initial conditions of the model were set to provide a conservative estimate of the system performance. A constant-temperature heat source at 37˚C was applied to the outer surface of the outer lumen. The inlet temperature of the cooling channel was set to 12.5˚C with flow rates of 15, 25, 35, 44, and 60 mL/min. Thermal and mechanical properties for the cooling fluid and PTFE tubes were set using COMSOL's built-in material definitions. Because there was no apriori knowledge of the thermal conductivity for the hydrogel, values from 0.2-40 $W \cdot m^{-1} \cdot K^{-1}$ were tested in order to determine the dependency on this value. Each simulation was run to determine the steady-state temperature of the hydrogel.

### 3.2.7 Water bath study

Using the results obtained from the simulation environment, a peristaltic pump (Stenner 85MHP17, Stenner Pump Company, Jacksonville, FL) was identified which could provide

sufficient flow to cool the hydrogel. A length of 0.30 m of the hydrogel-filled injection system was submerged in a 0.30 m × 0.14 m × 0.03 m container filled with water at 36.5-37.5˚C. The distal end of the injection system protruded out of the container and emptied the cooling fluid outside of the system. A thermocouple with attached microprobe was inserted to measure the hydrogel temperature at intervals of 0.05 m along the tube. Water at 0-3˚C was used as the cooling fluid and pumped at a rate of 44 mL/min. The measured temperature of the cooling fluid at the inlet to the injection system was 12.5˚C.

Hydrogel was loaded into the injection system and allowed to reach 37˚C. Once the hydrogel had reached the temperature of the water bath, the pump was started and temperature measurements of the hydrogel were taken at intervals of 1 s for approximately 3 min to ensure steady state. This procedure was performed three times for each temperature measurement and the averages were used for comparison to the heat transfer model.

### 3.2.8 **Beating heart injections in porcine model**

Demonstration of the modified injection system design was then performed in a porcine model in vivo in a protocol that followed the National Institutes of Health guidelines for animal care and that was approved by the University of Pittsburgh's Institutional Animal Care and Use Committee. Testing with the VP15 hydrogel, PA imaging and depth control were carried out on the first animal and patterned injections were performed on the second animal.

A preoperative static 3D computed tomography (CT) image dataset was collected in order to provide image guidance during the procedure, and in order to plan the desired injection pattern on the epicardial surface. Surface models of the pericardium, endocardium, cardiac vasculature, rib cage, and fiducial markers on the chest wall were constructed from the 3D image

set. A 15 mm square injection pattern was selected on the anterior surface of the left ventricle between the anterior interventricular artery and the diagonal artery.

Saline cooling fluid and VP15 hydrogel were pre-cooled prior to the procedure.

During the procedure the heart was allowed to beat naturally, while artificial ventilation was used to regulate respiration at a rate of 12 breaths/min. Access to the apex of the heart was achieved through a subxiphoid skin incision and a second small incision in the pericardium. Injecting head section of the robotic device were placed onto the epicardium, under the pericardium, through these incisions. Once placed on the heart, the device was manually controlled using virtual image guidance in which a virtual view of the robot and anatomy were displayed to the surgeon on the control computer.

Prior to reaching the first target, both the inner and outer lumens of the injection line were kept empty, in order to limit the volume of water expelled into the pericardial space. Upon acquisition of the first target, the cooling fluid was first pumped through the system at a flow rate of 44 mL/min. Next, hydrogel was introduced to completely fill the inner lumen. The needle tip was then advanced into the myocardium, and 0.5 mL of cooled hydrogel was injected into the LV wall. The needle was then retracted. With the injection line filled with hydrogel and the cooling fluid continuing to flow, the robot was driven to the second injection site where another injection was performed. After the second site was injected, the robot was removed from the animal and visually inspected to ensure that no solidification of the hydrogel had occurred in the inner lumen. Saline was pushed through the injection line to ensure the line was free of occlusion. After inspection the robotic device was once again placed on the heart and the procedure was repeated for the third and fourth injection targets.

Upon completion of the injections, the animal was euthanized and the heart was excised and placed in a warm saline bath. Neither identifiable needle tracks nor backflow of the hydrogel were visually inspected. Photoacoustic (PA) imaging was performed to localize the hydrogel material in the excised heart. Quantitative comparison of the planned and actual injection locations was done to determine the positioning accuracy of the modified injection device. The locations of the injection sites in the PA image were calculated by first segmenting the foreground pixels using k-means clustering, then computing the intensity-weighted centroid of each cluster. In order to compare the actual injection locations with the planned injection locations, the rigid registration between the imaged points and the planned points was solved using least squares. A scaling factor was also included to account for the shrinkage of the heart post mortem [168].

## 3.3 RESULTS

### 3.3.1 Thermal and mechanical behavior of poly(NIPAAm-co-VP-co-MAPLA) hydrogels

Thermoresponsive poly(NIPAAm-co-VP-co-MAPLA) with varied composition was synthesized by radical polymerization and its structure was confirmed with NMR (**Figure 3-1a,b**). In the polymer design, NIPAAm provides thermal responsiveness, while increasing VP content tunes the hydrophilicity for lower viscosity, higher transition temperatures and longer transition times. MAPLA, incorporating hydrolytically labile PLA segments, provides an “insoluble to soluble” shift to the whole polymer at body temperature as these hydrophobic segments are cleaved. To ensure smooth injection without solidifying the hydrogel in the catheter, a hydrogel with a higher

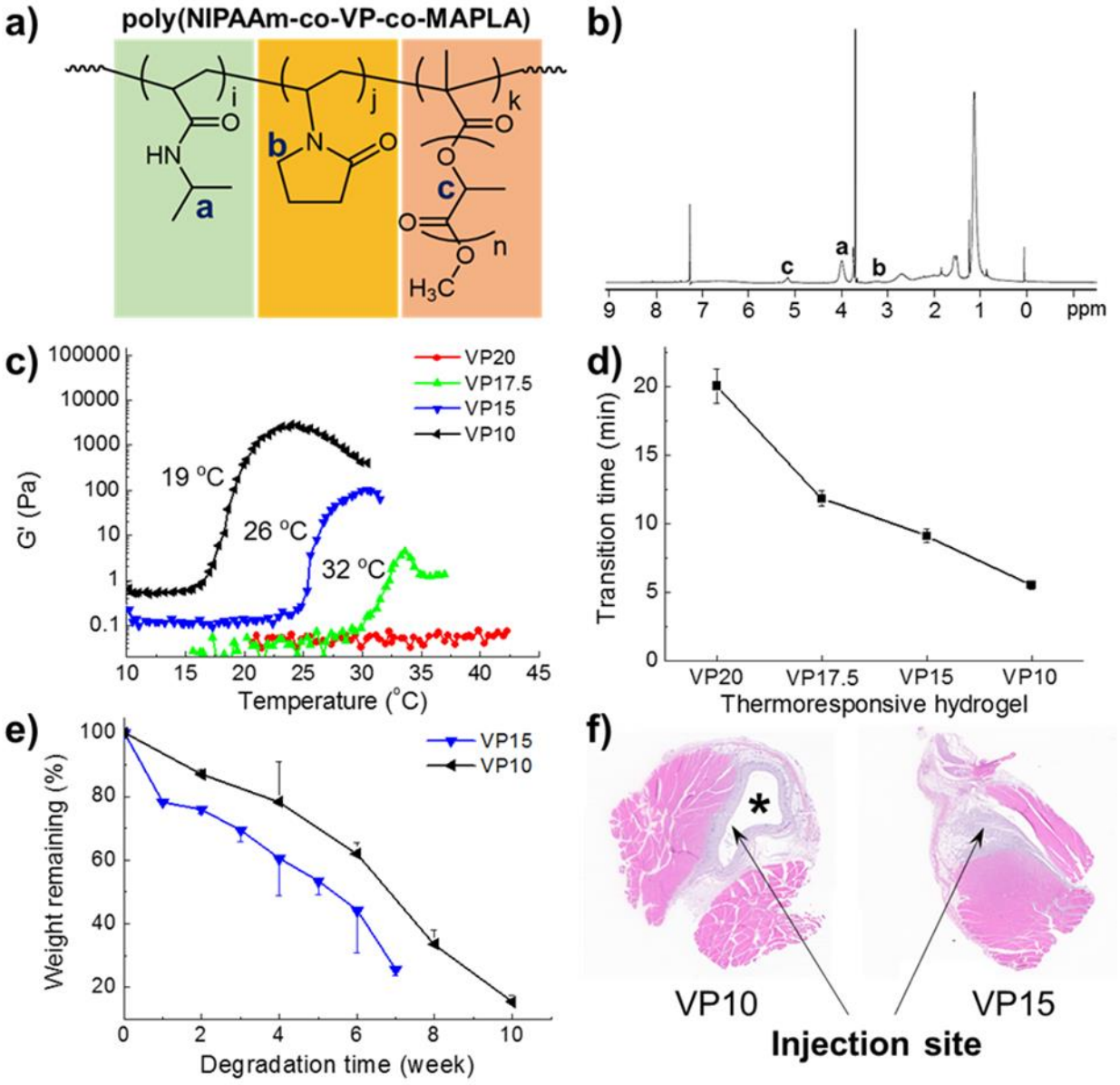


**Figure 3-1.** (a) Composition of poly(NIPAAm-co-VP-co-MAPLA). (b) $^{1}$H NMR of poly(NIPAAm-co-VP-co-MAPLA) with feed ratio of 80:10:10 (VP10). (c) Shear modulus of poly(NIPAAm-co-VP-co-MAPLA) hydrogels under temperature change. (d) Transition time of poly(NIPAAm-co-VP-co-MAPLA) hydrogels in air. (e) Weight loss of VP10 and VP15 hydrogels in PBS. (f) H&E staining of rat hindlimb muscle 28 d after hydrogel injection, left: VP10, right: VP15, * indicates the hydrogel mass.

transition temperature is more attractive. As shown in Figure 1c, the transition temperature increases as the VP feed ratio used in the polymer synthesis increases, from 19˚C (VP10) to an undiscernible transition (VP20, turbidity increase at elevated temperature observed), consistent with increased hydrophilicity. In addition, the viscosity of the hydrogel in the solution state decreased with the increased VP content, which also favored easier hydrogel delivery. While the synthesized hydrogels underwent thermal transition immediately upon contact with 37˚C saline, in 37˚C air the transition was slowed for the more hydrophilic compositions (**Figure 3-1d**). This property helped the hydrogel to stay in solution form along the injection pathway from outside to inside the body.

Mechanical characterization of the hydrogels at 37˚C demonstrated that hydrogels VP17.5 and VP20 were too weak to be handled in testing and were not assessed further, while VP10 and VP15 were further evaluated (VP10: 240±49 kPa, VP15: 21±4 kPa). Both hydrogels completely dissolved in 37˚C saline after 7 to 10 wk of incubation, with more hydrophilic VP15 showing faster solubilization, as shown in **Figure 3-1e**.

In biocompatibility testing, both hydrogels induced a typical foreign body response in vivo when injected into the rat hindlimb muscle for 28 d, without signs of local or systemic toxicity. Histological evaluation demonstrated local macrophage involvement at the injection site, with the number of macrophages (CD68 positive staining) being greater for the VP10 hydrogel. The injection site also demonstrated a residual region of hydrogel for VP10, whereas for the faster solubilizing VP15 no distinct polymer region was found (**Figure 3-1f, Figure 3-2**).

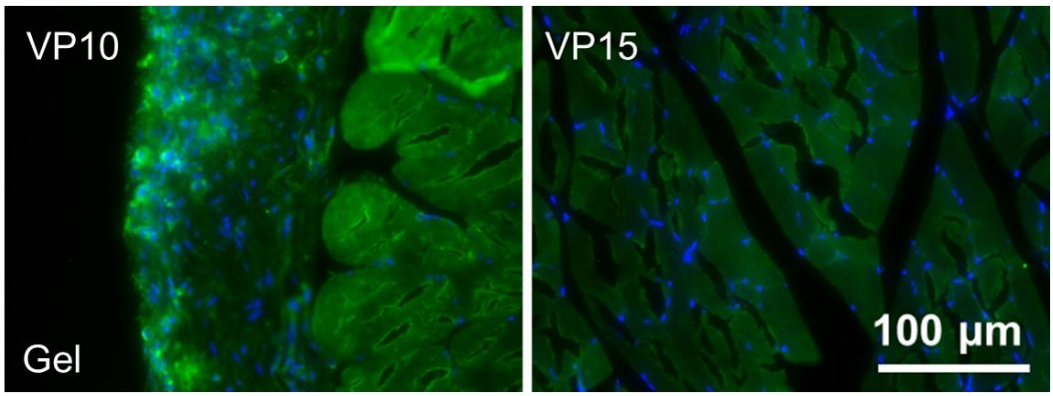


**Figure 3-2**. Immunochemictry staining of CD68 28 d after hydrogel injection, left: VP10, right: VP15. Blue: DAPI.

### 3.3.2 **Efficiency of cooling system**

In the new version of the injection system, a cooling sheath was added to provide cooling fluid running parallel to the hydrogel solution. A simulation of the temperature distribution of the hydrogel was found to be insensitive to changes of the thermal conductivity (0.2-40 $W \cdot m^{-1} \cdot K^{-1}$) of the hydrogel. Simulation results with varied cooling fluid flow rates and outer tube diameters showed that the greatest influencers on the hydrogel temperature distribution were the cooling fluid inlet temperature and flow rate. Changing the tube diameter from 15 to 17 gauge had little effect on the hydrogel temperature profile, leading to the choice of 17 gauge outer tubing to minimize tether stiffness, and a cooling fluid flow rate of 44 mL/min to keep the hydrogel well below 27˚C (**Figure 3-3b**).

The injection system with the cooling-sheath incorporated was loaded with hydrogel and initially tested in a 37˚C water bath for its cooling effect. Time traces of the temperature of the hydrogel at various points along the length of the cooling system are shown in **Figure 3-3c**. The cooling system lowered the temperature of the hydrogel to a minimum in approximately 10 s

where the temperatures increased slightly and settled to steady-state values. The steady-state values along the entire length (0.3 m) of the injection system were well below the transition temperature of VP15. Within the first 0.2 m the steady-temperature was near or below the transition temperature of VP10. Since the distance from the subxiphoid incision to the epicardial injection injection sites would be less than 0.3 m, the hydrogel would be expected to remain in the liquid state.

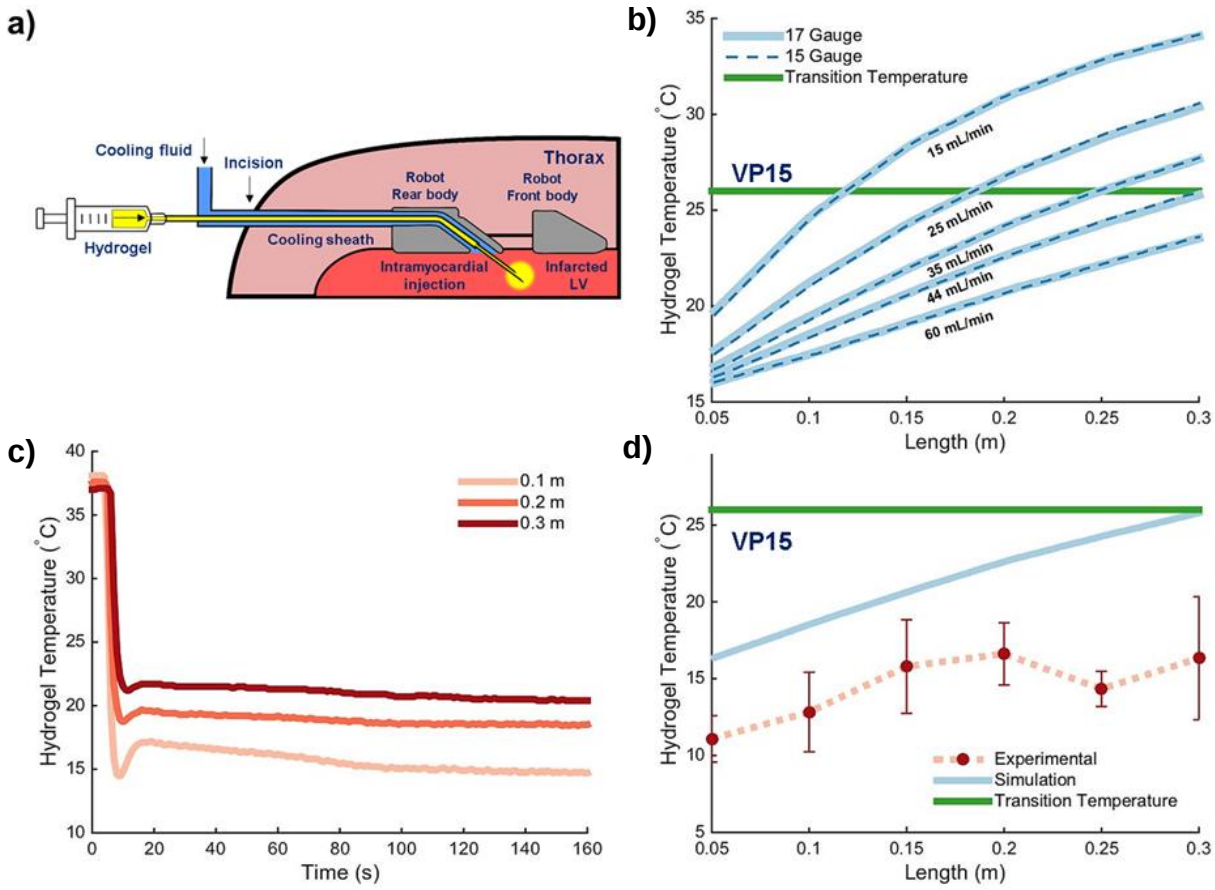


**Figure 3-3.** (a) Components of the injection device (modified HeartLander) and illustration of transepicardial hydrogel injection with cooling (b) Simulation of hydrogel temperature cooled by cooling fluids with different flow rates. (c) Simulated temporal change of 37 ˚C hydrogel temperature at different positions in the catheter under cooling. (d) Measured hydrogel temperature along the cooled catheter, comparing to the simulated values and trasition temperature of VP15.

**Figure 3-4**. HeartLander crawler crawling on porcine heart.

To evaluate the coordination between hydrogel and the cooling system, the catheter was preloaded with hydrogel and submerged in 37˚C water bath to reach an isothermal state, followed by active cooling. Both VP10 and VP15 gelled and occluded the catheter at 37˚C, and in both cases the hydrogels were dissolved as a result of heat transfer with the cooling fluid, allowing reoccurence of smooth injections. The unblocking process took ~10 s for VP15 and ~45 s for VP10 (data not shown), remarkably consistent with the measured time required for the cooling system to bring the hydrogel temperature down to near transition temperature (**Figure 3-3c**). This feature of lower potential for catheter occlusion and faster occlusion recovery again favored VP15 in terms of both safety and efficiency of the procedure, in addition to the reduced viscosity (easier injection) and slower phase transition of VP15 comparing to VP10 (less occlusion in the needle). Taking the aforementioned aspects into consideration, VP15 was chosen for further ex vivo and in vivo experiments.

### 3.3.3 **Ex vivo injection test**

In an ex vivo injection test using an excised porcine heart at 37˚C, the injection device successfully crawled to 2 distant injection sites and performed one shallow injection at 3.5 mm

deep and one deeper injection at 6.8 mm deep, as shown in the **Figure 3-4** and **Figure 3-5**. The injection depth was controlled by the distance the needle was pushed out of the catheter, as demonstrated in **Figure 3-6**. The hydrogel temperature was maintained below the hydrogel transition temperature and no gelation was observed in fluid pathway. It took approximately 10 s to complete the injection of 0.3 mL VP15 hydrogel. Inspecting the site visually by dissection 5 min after the injection showed ellipsoid hydrogel deposits with long axes orienting along the circumferential direction. The shallow deposit was 10.8 mm long and 3.1 mm wide, whereas the deeper deposit was 8.2 mm long and 2.7 mm wide (**Figure 3-5**).

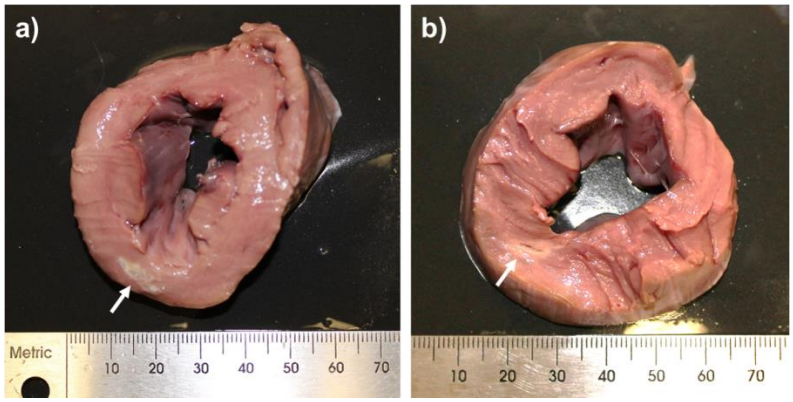


**Figure 3-5**. Sections of porcine heart after ex vivo injection of VP15. (a) shallow injection at 3.5 mm deep. (b) Deep injection at 6.8 mm.

### 3.3.4 In vivo injection test

Hydrogel injections in healthy beating porcine hearts were performed to validate the concept of the subxiphoid transepicardial injection strategy and to demonstrate the potential to perform injections in a pre-defined pattern as might be planned in a patient-specific manner for an

ischemic area after an MI. During the procedure, the crawler was manually controlled to approach the first target site without loading of the hydrogel until the time of injection. Hydrogel was not retrieved from the catheter, but remained in the injection pathway for the subsequent injections. With the cooling system functioning, smooth injections were achieved without experiencing hydrogel clotting of the catheter. No hydrogel leakage was observed on the epicardial surface of excised heart, as a result of rapid gelation of hydrogel upon contact with warm myocardium. No arrhythmias or other severe complications have been observed.

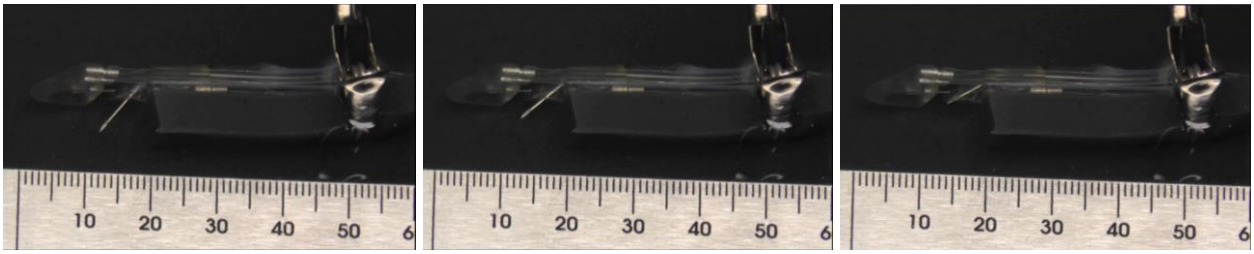


**Figure 3-6**. Pushing and retracting needle from catheter.

As shown in **Figure 3-7a**, four distinct injection sites in a square pattern can be identified near the cardiac apex under photoacoustic (PA) imaging. The observed injection sites were placed in the preoperative 3D virtual view of the animal to compare with the pre-planned injection sites as marked by black crosses (**Figure 3-7b**). The overlaid PA image shows that the injection pattern accurately matches the desired pattern with a mean error of 1.4 ± 0.5 mm. Due to the artifactual reduction in size of the heart upon explant, the measured square was smaller than both that planned and recorded during the procedure. The calculated scaling factor was determined to be 1.87, meaning the excised heart size reduction post mortem was approximately 47%, which is consistent with the observations of Reynolds and Hartshorne [167]. In addition to

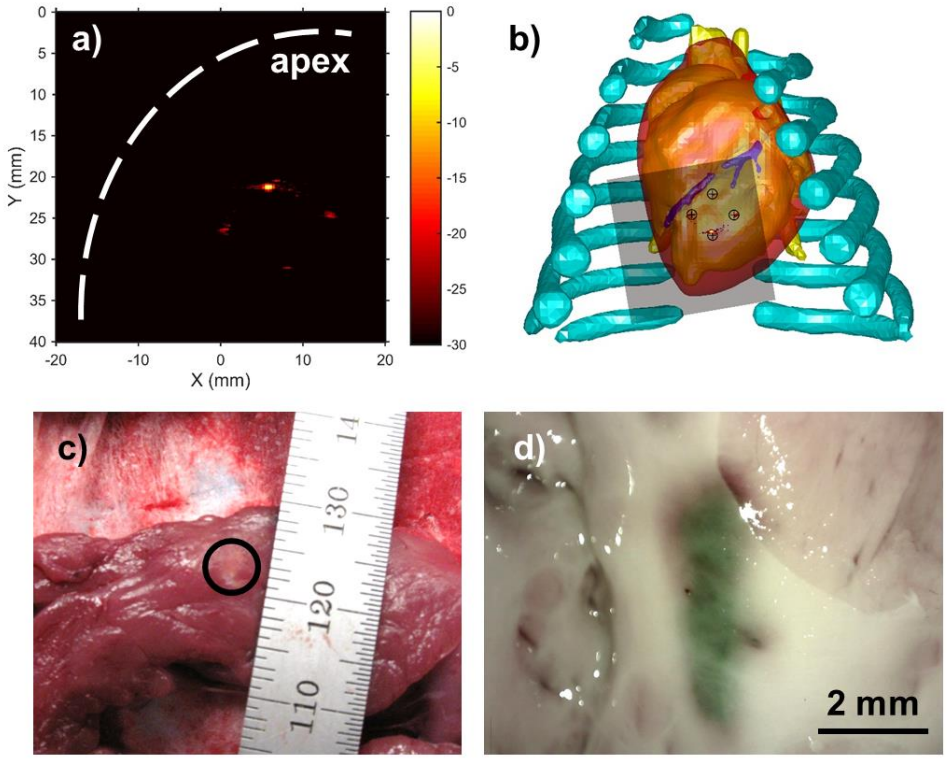


**Figure 3-7.** (a) Photoscoustic imaging of patterned injections in a beating porcine heart, probing from the apex. The signals of injection sites away from apex were weaker due to energy loss through tissue. (b) Match between imaged injection sites with planned. (c) Injected hydrogel in the myocardium. (d) Deep injection of hydrogel on the endocardial side.

the accuracy in injection localization, reliability in depth control was also achieved, as indicated by the ability to image the 4 injection sites were in the same plane with PA imaging. Rapid hydrogel gelation limited the occurence of diffusion in the healthy myocardium. Consistently, the injected hydrogels could be found ~ 7 mm underneath the epicardial surface in both animals undergoing the surgery, as shown in **Figure 3-7c**. The morphological integration of the hydrogel with the myocardium was similar to that observed in the ex vivo test. Deeper injections about 15 mm underneath the epicardial surface could also be achieved by inserting the needle closer to the

endocardial surface such that the dyed hydrogel could be directly visualized (**Figure 3-7d**). Given the angle of the injection system, 0-12.5 mm of the metallic needle was exposed to 37˚C tissue instead of being protected by cooling fluid as in the catheter. Despite this uncooled region in the needle, it was found that multiple injections of the VP15 hydrogel could be accomplished without occlusion, as in the test ex vivo.

## 3.4 DISCUSSION

The coordinated design of a thermoresponsive hydrogel and a robotic injection device employing local temperature control has been accomplished such that the hydrogel was compatible with cardiac wall injection. Further, this hydrogel could be delivered in a targeted fashion into a beating heart in a large animal model. Such targeted delivery would be compatible with a patient-specific planning strategy to optimize the mechanical benefits of the hydrogel bulking effect [169, 170]. Previous experimentation has shown the ability of HeartLander to reach the posterior surface of the heart and for this device to electrical activity mapping, although the latter functionality was not present on the device used for these studies [166, 171]. The efficaciousness of the hydrogel therapy has not been the subject of this study and chronic large animal studies in animals with MI would be necessary. However, similar synthetic hydrogels have shown benefit in small animal models and the general concept of hydrogel introduction into the infarcted LV wall is undergoing clinical evaluation using endovascular delivery approaches [62, 99]. Co-delivery of cells, growth factors, gene vectors or drugs could also be options. The described

coupled biomaterial/robotic delivery system represents an attractive technique that takes advantage of the phase change behavior of a bulking agent and robotic control systems to potentially achieve a planned intervention for patients at risk for cardiac failure following MI.

## 3.5 CONCLUSION

A coupled thermoresponsive hydrogel and robotic injection system was developed, incorporating a temperature controlled injectate line capable of targeted injections and amenable to use with a subxiphoid transepicardial approach for hydrogel injection after myocardial infarction. The confirmation of precise location and depth injections would facilitate a patient-specific planning strategy to optimize injection patterning to maximize the mechanical benefits of hydrogel placement.

# 4.0 IMPROVING THERAPEUTIC FUNCTION OF THERMALLY RESPONSIVE HYDROGELS BY INCORPORATING A REACTIVE OXYGEN SPECIES SCAVENGER

## 4.1 INTRODUCTION

As a mechanical therapy for MI, intramyocardial biomaterial injection reduces LV wall stress by increasing wall thickness and decreasing the ventricle radius, thereby moderating the remodeling process and lowering the probability of heart failure [8, 33, 53]. Various biomaterials have shown therapeutic effects in pre-clinical trials [17, 30-32, 35, 37, 39-41, 172]. Recently, PRESERVATION-1 and AUGMENT-HF trials using alginate hydrogels as injectate have reported their clinical results. Favorable trends in EF shortly after injection were observed in AUGMENT-HF trial, as well as improvements in secondary endpoints in both studies. However, long term functional benefits were not confirmed in neither trial on the contrary to observed cardiac function preservation effects in pre-clinical trials [14, 15, 22]. In addition to optimizing injection parameters corresponding to the characteristics of MI in patients, it is expected that increasing bioactivity of the injectates upon mechanical effects could augment the therapeutic effects of injection treatment.

Excessive reactive oxygen species (ROS) are generated after myocardial infarction, especially after reperfusion [173, 174]. These highly radical oxides cause cell membrane damage, leading to cardiomyocyte apoptosis [173-176]. ROS also stimulate elevation in inflammatory cytokines and activate extracellular matrix degradation. As a result, ROS promote fibrosis and LV dilation. In a number clinical trials, administration of antioxidant drug obtained beneficial therapeutic outcomes [177-181]. However, contradictory results were observed in other clinical studies, as well [182-189]. Efforts have been made to the discrepancies across studies, and it is indicated that delivering a sufficient dosage of antioxidant drugs with favorable spatiotemporal parameters is critical for availability of the drugs to LV myocardium and rebalancing ROS metabolism [174].

Our hypothesis is that combining biomaterial injection and antioxidant drug administration by covalently attaching ROS scavenger to injectable material could exploit the advantages of both therapies and simultaneously remedy the shortcomings, thus achieving additive therapeutic outcome. The amount and distribution of injectates in the infarcted area, border zone and remote tissue can be precisely manipulated with open-chest surgeries and minimally invasive procedures, which enables both optimization of the mechanical effect from the stiff biomaterial and localized concentration of ROS scavenger in a targeted manner. Especially, safety of minimally invasive delivery immediately after the ischemic event has been proven in large animal models, showing the potential of performing such procedure right prior to reperfusion for MI patients. Some injectates including thermally responsive hydrogel is able to infiltrate the tissue before gelation and form interpenetrating network, thus allows efficient

cellular level access of attached scavenger to adjacent ROS. Biodegradability of injected biomaterial and the bond between the scavenger and substrate can be modulated to achieve long term retention of the antioxidant drug and avoid inducing reductive stress.

In this study, a design following the aforementioned strategy of attaching a ROS scavenger, 4-amino-TEMPO to a biodegradable, thermally responsive injectable hydrogel is raised. The poly(N-isopropylacrylamide) based hydrogel has been successfully delivered by a minimally invasive miniature robotic device in a porcine model through subxiphoid epicardial pathway [105]. 4-amino-TEMPO is attached to the polymer sidechain the ROS scavenging effect is evaluated in vitro. A rat infarction/reperfusion model is used to demonstrate the hypothesis that the ROS scavenging hydrogel could mitigate the oxidative damages in the myocardium and preserve LV function and geometry, and the overall efficacy would be greater than mechanical or antioxidant treatment alone. To the best of our knowledge, this is the first time that such strategy and design is practiced in vivo.

## 4.2 MATERIALS AND METHODS

### 4.2.1 Materials

All chemicals were purchased from Sigma-Aldrich unless otherwise stated. N-isopropylacrylamide (NIPAAm) was purified by recrystallization from hexane and vacuum-dried. N-vinylpyrrolidone (VP), lactide, benzoyl peroxide (BPO), sodium methoxide ($NaOCH_3$), methacryloyl chloride, methacrylic acid N-hydroxysuccinimide ester (MANHS), 4-amino-TEMPO, cyclohexylamine (CHA) and other solvents were used as received.

### 4.2.2 **Synthesis of polymers**

The MAPLA was synthesized as previously described [113]. Poly(NIPAAm-co-VP-co-MAPLA-co-MANHS) copolymer was synthesized from NIPAAm, HEMA, MAPLA and MANHS by free radical polymerization. The feed ratios of NIPAAm, VP, MAPLA and MANHS were 80/15/5/5. Monomers (0.07 mol) were dissolved in 180 mL of 1,4-dioxane containing 0.23 g BPO. The polymerization was carried out at 75°C for 20 h under argon protection. The copolymer was precipitated in hexane and further purified by precipitation from THF into diethyl ether and vacuum-dried, with yields of ~80%. Poly(NIPAAm-co-VP-co-MAPLA-co-MANHS) (pNVMN) was subsequently dissolved in DMF at a concentration of 20 wt% and supplemented with 2.65 wt% 4-amino-TEMPO or cyclohexylamine and reacted at room temperature for 12 h under argon protection (**Scheme 4-1**). The solutions were transferred into dialysis bags and dialyzed in DMF for 3 d with periodical changes of DMF. Dialyzed solutions were concentrated by rotary evaporation and dried in vacuum to obtain poly(NIPAAm-co-VP-co-MAPLA-co-MATEMPO) (pNVMT) and poly(NIPAAm-co-VP-co-MAPLA-co-MACHA) (pNVMC), respectively.

### 4.2.3 **Quantification of 4-amino-TEMPO in pNVMT**

Electron paramagnetic resonance (EPR) spectra were recorded using a Bruker EMX premiumX spectrometer (Bruker BioSciences, Billerica, MA) operating at X-band with a 100 kHz modulation frequency as described previously [190]. Data acquisition was performed using Bruker Xenon software. Data processing was performed using Graphprism software.

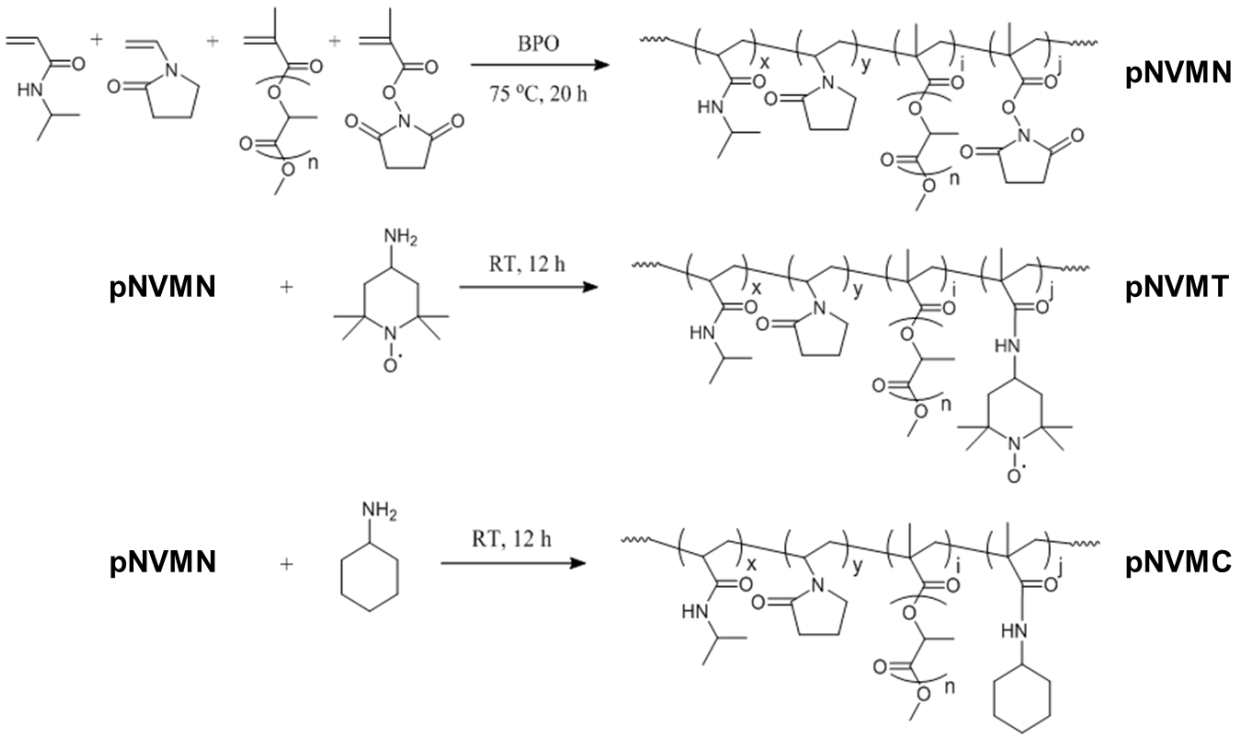


**Scheme 4-1.** Synthesis of poly(NIPAAm-co-VP-co-MAPLA-co-MATEMPO) (pNVMT) and poly(NIPAAm-co-VP-co-MAPLA-co-MACHA) (pNVMC).

Liquid samples of 50 μL were loaded in a glass capillary tubes that were sealed on one end using critoseal clay and placed inside the 4 mm ESR quartz tube. Hydrogel was placed directly in the 4 mm ESR quartz tube. The quartz tube was positioned inside the cavity and EPR spectra were recorded at room temperature. The following settings were used: microwave frequency, 9.85 GHz; sweep width, 100 G (200 G for hydrogel); microwave power, 20 mW; modulation amplitude, 0.5 G; receiver gain, 60 dB (30 dB for hydrogel); time constant, 0.01 ms; conversion time, 15 ms, sweep time, 30 s (60 s for hydrogel); number of scans, 10.

### 4.2.4 **Physical properties of hydrogels**

pNVMT and pNVMC were dissolved in PBS (15 wt%) and placed in 24 well plates, incubated at 37°C to obtain hydrogel discs (TEMPO Gel and Analog, dimensions). The hydrogel discs were then loaded in a water bath equilibrated to 37 °C to reach stable water content. An ElectroForce 3200 Series II (Bose, Minnesota, US) equipped with a 2.5 N load cell was utilized to record the compression stress-strain curve immediately after the samples were taken out of the water bath.

Rheology studies were conducted on a TA Instruments rheometer (AR2000) to observe viscosity changes in the hydrogels during the temperature induced sol-gel transition. The polymer solutions (15 wt% in PBS) were placed between two parallel plates. With a temperature sweep from 5 to 35°C and a heating rate of 5oC/min, the shear storage modulus G' and the loss modulus G" were collected as a function of temperature at a fixed strain of 2% and a frequency of 1 Hz.

Hydrogel degradation was quantified by mass loss measurements. Hydrogels with known initial dry masses (~60 mg) were immersed into 4 mL of PBS at 37°C. PBS was changed weekly. At predefined time points over a 4 w period the hydrogels (n=3 each) were lyophilized and the relative mass loss was recorded.

### 4.2.5 **In vitro ROS scavenging effect of TEMPO Gel**

Fenton reaction was employed to determine the inhibiting/scavenging effect of hydrogels on hydroxyl radical generation. The reaction mixture, containing 50 µL TEMPO Gel or Analog, 60 µL $FeSO_4$ solution (2 mM), 50 µL Safranin O (360 µg/mL) and 80 µL $H_2O_2$ (6 wt%) or water, was incubated for 10 min, and then heated in a 55ºC water bath for 30 min. In the blank group

(no inhibiting reagent), 50 μL DI water was used instead of the hydrogel solution. In the control group (no oxidative reagent or inhibiting reagent), 50 μL and 80 μL DI water were used to substitute the hydrogel solution and $H_2O_2$ solution, respectively. The reaction mixtures were cooled to room temperature and the absorbance at 492 nm was measured on a plate reader. The inhibiting/scavenging effect on hydroxyl radicals was calculated using equation (1):

$$\text{Inhibiting/scavenging effect (\%)} = (A_{hydrogel}-A_{blank})/(A_{control}-A_{blank}) \times 100 \quad (1)$$

Pyragallol assay was employed to determine the scavenging effect of hydrogels on superoxide radicals. 50 μL TEMPO Gel or Analog was mixed with 120 μL Tris-HCl (50 mM, pH=8.1), 20 μL pyrogallol (3mM) was subsequently added into the mixture for 5 min in the dark. 40 μL HCl (1 M) was finally added into the mixture to stop the reaction. In the control group, 50 μL DI water was added instead of hydrogel solution. The absorbance at 299 nm was measured by spectrophotometer on a plate reader. The scavenging effect on superoxide radicals was calculated using equation (2):

$$\text{Scavenging effect (\%)} = ((A_{control}-A_{hydrogel})/A_{control}) \times 100 \quad (2)$$

Cell protective effect of TEMPO Gel (hydrogel made from pNVMT) against oxidative stress was evaluated by smooth muscle cell culture with $H_2O_2$ treatment. Rat vascular smooth muscle cells (SMCs) were seeded and cultured in Dulbecco's modified Eagle medium (DMEM) (Gibco, Life technologies) with 10% fetal bovine serum (FBS), 1% penicillin/streptomycin for 24 with before changing culture medium with fresh medium. SMCs were cultured for another 30 min as the healthy control group. $H_2O_2$ was added to culture medium with final concentration of 500 μM to generate oxidative stress for 30 min as negative control. In treatment groups, pNVMT solution (15 wt% in PBS) and pNVMC solution (15 wt% in PBS) were added to the culture medium (10%, v/v) immediately after addition of $H_2O_2$, respectively. Intracellular ROS was

stained with carboxy-H2DCFDA (Thermo Fisher Scientific, MA) according to manufacturer's instructions. Fluorescent images were taken and averaged fluorescent strengths were calculated by dividing the total fluorescent strengths with total area of cells. Cell metabolic activity was measured (n=4 each) using an MTS assay kit (Promega CellTiter 96 Cell Proliferation Assay). Cells were also observed under fluorescence microscopy after live/dead staining with a Promokine Live/Dead Cell Staining Kit.

### 4.2.6 **Animal model**

10-12 w old adult female syngeneic Lewis rats (Harlan Sprague Dawley Inc., Indianapolis, IN, USA) weighing 200-250 g were used for this study. The research protocol followed the National Institutes of Health guidelines for animal care and was approved by the Institutional Animal Care and Use Committee of the University of Pittsburgh. Rats were divided into 3 treatment groups (TEMPO Gel, Analog and TEMPO Drug) and 2 control groups (healthy and PBS injection) to study the short- and long-term effects of hydrogel injection therapy.

Left ventricular infarction was created by ligation of the proximal left anterior descending (LAD) coronary artery as previously described [61]. Briefly, rats were anesthetized with isoflurane (3.0% induction and 1.0% maintenance) inhalation with 100% oxygen followed by intubation and respiratory support with a rodent volume-controlled mechanical ventilator (683 Ventilator, Harvard Apparatus, Holliston, MA, USA) at a tidal volume of 2-2.5 mL and 60-70 breaths/min. Rats were placed in the spine position and the chest was shaved and prepared with povidone-iodine solution. Procedures were performed in a sterile environment on a heating blanket. The heart was exposed through a 4th left thoracotomy with electrocardiogram monitoring. The proximal LAD coronary artery was ligated with 5-0 polypropylene.

Visual identification of infarction was used to include rats with large infarctions. 30 min after ligation, total of 100 μL of TEMPO Gel (15 wt% pNVMT in PBS), Analog (15 wt% pNVMC in PBS), TEMPO Drug (1.0 wt% 4-amino-TEMPO in PBS), or PBS was injected into the distal, proximal, lateral, and anteiror wall regions bordering the infarct as well as into the center of the infarct (5 injections, 20 μL per region). The volume of hydrogel injected was arrived at based on the authors' experience performing biomaterial injections into this rat model, generally seeking to maximize injection volumes, but recognizing that hydrogel regurgitation will increasingly occur when too large of injection volumes are attempted. Immediately after injections, the ligations were removed to allow reperfusion. After reperfusion, the incision was closed in layers with 4-0 polypropylene continuous sutures.

### 4.2.7 **Magnetic resonance imaging of TEMPO Gel distribution**

24 h after infarction/injection/reperfusion, rat hearts were excised and fixed in 37$^{o}$C formalin. MRI was performed on a 9.4T AVIII HD spectrometer (Bruker Biospin, Billerica, MA) equipped with a 30 cm bore and 12 cm gradient set. The excised hearts were imaged using a 23 mm mouse brain volume coil. The hearts were kept at 37°C via a warm air system with a fibre optic temperature probe placed underneath the hearts (SA Instruments Inc., Stony Brook, NY). A 3D $T_1$- and $T_2$-weighted RARE sequence was used with the following parameters: repetition time (TR)/echo time (TE) = 500/10 ms for $T_1$ and 1800/35 ms for $T_2$-weighted images, field of view (FOV) = 15×15×15 mm$^3$, acquisition matrix = 128×128×128, with an isotropic resolution of 117 μm, and a RARE factor = 8.

### 4.2.8 **Lipid peroxidation assay**

Frozen heart samples (same hearts used for mitochondrial metabolism evaluation) were homogenized in lysis solution. Malondialdehyde (MDA), a product of lipid peroxidation as a result of oxidative degradation of lipids was quantified with lipid peroxidation colorimetric assay (Abcam, MA) according to manufacturer's instructions.

### 4.2.9 **Characterization of mitochondrial metabolism**

24 h after infarction/injection/reperfusion, rat hearts (n=4) were excised and quickly washed in cold PBS to remove the blood. The excised heart tissues were flash frozen and stored in liquid nitrogen for EPR spectroscopic analysis to measure the free radical and paramagnetic species. Heart tissue samples were prepared by transferring the frozen heart tissue (450-600 mg) into a ceramic mortar pre-chilled with liquid nitrogen [190]. The frozen tissue was maintained at 77 K in liquid nitrogen and broken into small pieces using a pestle. The tissue in liquid nitrogen was then loaded directly in to an EPR finger Dewar containing liquid nitrogen. The EPR Dewar was filled with liquid nitrogen to a sufficient volume and inserted in to the EPR resonator. The localization of the heart tissue sample was adjusted to the middle of the resonator. All spectra were recorded with the following parameters: microwave frequency = 9.49 GHz, sweep width = 500 G, microwave power = 20 mW (1 mW for semi-quinone radicals), modulation amplitude = 5 G (2 G for semi-quinone radical signals), receiver gain = 30 dB, time constant = 164 ms, conversion time = 80 ms (32 ms for quinone radicals), sweep time = 120 s, and number of scans = 10.

### 4.2.10 **Cell apoptosis**

24 h after infarction/injection/reperfusion, rat hearts from the treatment groups were excised and fixed in 37$^{o}$C formalin. Hearts collected from healthy rats and rats experienced 30 min ligation without further treatment were also fixed. Terminal deoxynucleotidyl transferase dUTP nick end labeling (TUNEL) was used to stain the heart sections. TUNEL positive cells in representative areas of infarction area (IF, middle of LV), border zone (BZ, ~1/4 and 3/4 of LV semicircle) and remote myocardium (RM, ends of LV semicircle) were counted to derive the percentage of dead cells in the LV. For convenience, representative area of the Healthy and 30 min infarction groups were assigned to the similar positions in other groups and defined as IF, BZ and RM.

## 4.3 RESULTS

### 4.3.1 **4-amino-TEMPO content in pNVMT**

The EPR spectrum of pNVMT dissolved in THF was featured with triple peaks appeared at the same fields as free 4-amino-TEMPO. As shown on the spectrum (**Figure 4-1a**), the intensities of peaks at 3506 G and 3522 G descends compared to the peak at 3491 G, as a result of hindrance in movement of covalently bonded 4-amino-TEMPO molecules. Triple peaks of free 4-amino-TEMPO have the same intensity (data not shown). In addition, the peaks of TEMPO hydrogel were distorted more as the freedom of attached 4-amino-TEMPO was highly limited in the aggregated polymer network (**Figure 4-1b**). Calibrated by the 3491 G peak intensities of 4-amino-TEMPO solutions with gradient concentration, the content of attached 4-amino-TEMPO

in pNVMT was determined to be 6.07 wt% or 0.356 mmol/g. On the other hand, pNVMT and its PBS solution were orange attributed to the color of nitroxide radicals in 4-amino-TEMPO. The orange color was bleached by reduction with ascorbic acid (data not shown).

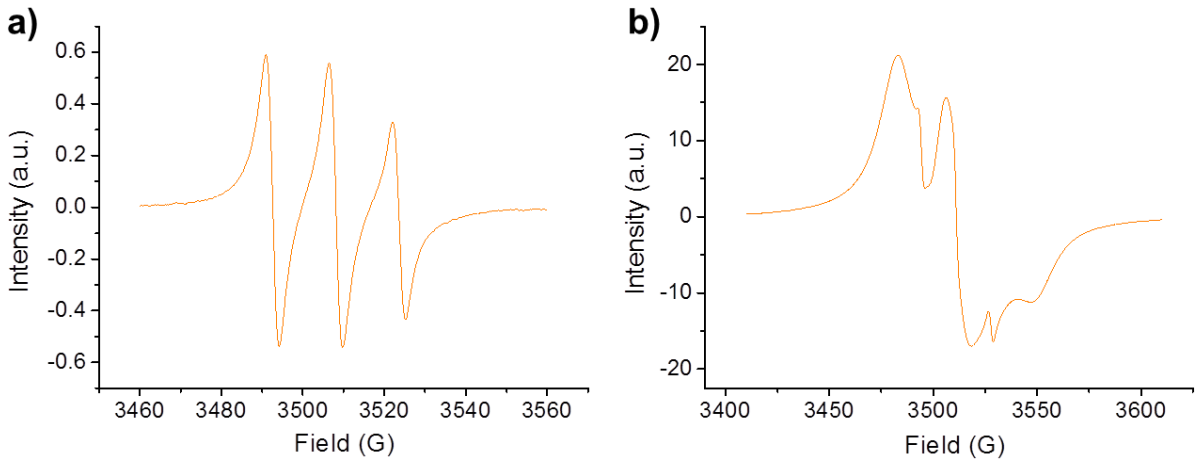


**Figure 4-1.** EPR spectra of pNVMT/THF solution and TEMPO Gel (gelled 15 wt% pNVMT/PBS solution).

### 4.3.2 **Physical properties of hydrogels**

pNVMT and pNVMC solutions (15 wt% in PBS) were low viscous liquids at 5ºC, and their shear modulus increased rapidly around 24.1ºC and 21.3ºC as temperature rises, which represent their sol-gel transition, respectively (**Figure 4-2**). When injected into 37 ºC PBS, pNVMT and pNVMC solutions gelled within seconds, generating TEMPO Gel and Analog, respectively. The compression modulus of TEMPO Gel was 222±66 kPa, higher than of Analog (50±8 kPa) (**Figure 4-3**). As shown by the weight loss profile of the hydrogels in PBS, TEMPO Gel and Analog had similar degradation rate and lost 50% weight in 2.5 w (**Figure 4-4**).

### 4.3.3 **In vitro ROS scavenging effect**

In Fenton reaction and Pyrogallol assay, TEMPO Gel or Analog (pNVMT or pNVMC solution) was added to the reaction mixture. They rapidly gelled in the mixture and kept the gel form during the reactions. Compared to control, TEMPO Gel inhibited 92.4±8.8% colorimetric change in Fenton reaction which generates hydroxyl radicals, significantly higher than the inhibiting effect of Analog (17.3±1.7%) (**Figure 4-5a**). Similarly, in superoxide-generating Pyrogallol assay, TEMPO Gel scavenged 66.4±1.5% superoxide radicals, significantly higher than 22.0±5.4% of Analog (**Figure 4-5b**).

Healthy SMCs exhibited spindle shape 24 h after seeding and showed weak fluorescent intensity in intracellular ROS staining (**Figure 4-6b**). On the contrary, SMCs became much brighter in intracellular ROS staining after 30 min of $H_2O_2$ treatment, and the cells became round in shape **(Figure 4-6a**). Similar to phenomena observed in the Fenton reaction and Pyrogallol assay, pNVMT or pNVMC solutions were added to the culture media and gelled instantly,

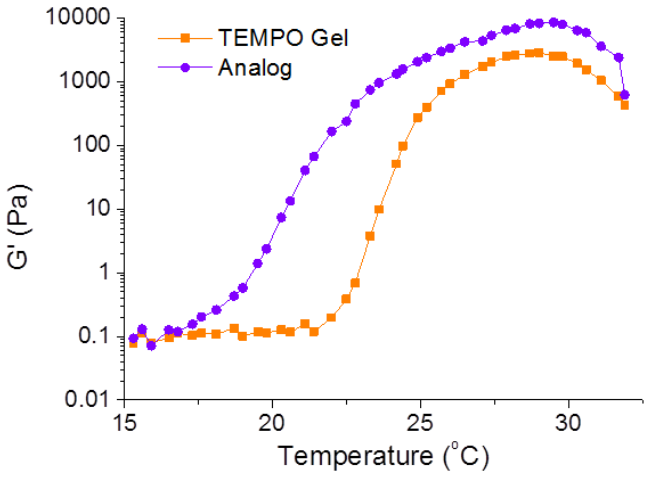


**Figure 4-2.** Temperature sweep of shear modulus (G') of TEMPO Gel and Analog.

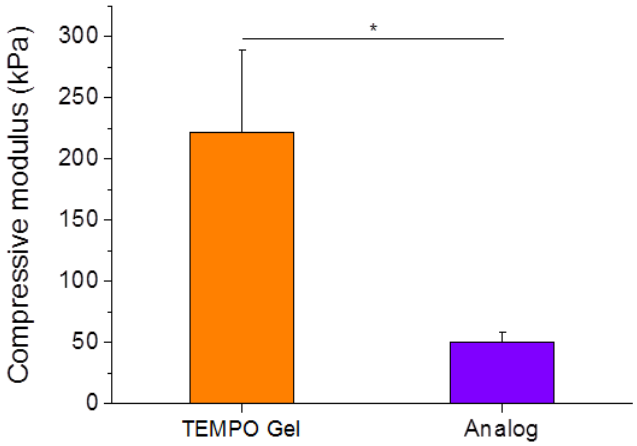


**Figure 4-3.** Compressive modulus of TEMPO Gel and Analog. * Significant difference, $p$ <0.05.

forming TEMPO Gel and Analog. Cell deformation and ROS increase were also observed in $H_2O_2$+Analog group, as shown in **Figure 4-6d**. Addition of TEMPO Gel maintained the spindle shape of SMCs seen in the healthy cells, but did not eliminate the brightening of $H_2O_2$ treated cells (**Figure 4-6c**). Divided by cell area, the increase in the average fluorescent intensity of the $H_2O_2$ treated cells compared to the healthy control was confirmed, reflecting the elevation of intracellular ROS concentration. TEMPO Gel mitigated the production of ROS species, as shown by the significant difference in fluorescent intensity compared to the $H_2O_2$ treatment group. The Analog did not show such effect (**Figure 4-6e**).

Determined by MTS assay, 500 μM $H_2O_2$ treatment significantly lowered the mitochondrial function of SMCs compared to healthy cells (**Figure 4-7a**). TEMPO Gel alleviated the oxidative damage caused by $H_2O_2$ to a level comparable to which caused by 100 μM $H_2O_2$, which could be interpreted as TEMPO Gel scavenged nearly 80% the oxidative stress. Consistent with the results in intracellular ROS staining, Analog did not present protective effect to oxidatively stressed SMCs (**Figure 4-7a**). About 25% cells died during the 30 min $H_2O_2$

treatment in the negative control group as revealed by Live/dead staining (**Figure 4-7b**). TEMPO Gel prevented SMCs deaths despite that mitochondrial function was impaired in the cells (98.1% live cell percentage compared to 98.5% of the healthy control). Again, Analog did not increase the survive rate of cells compared to the negative control (**Figure 4-7b**).

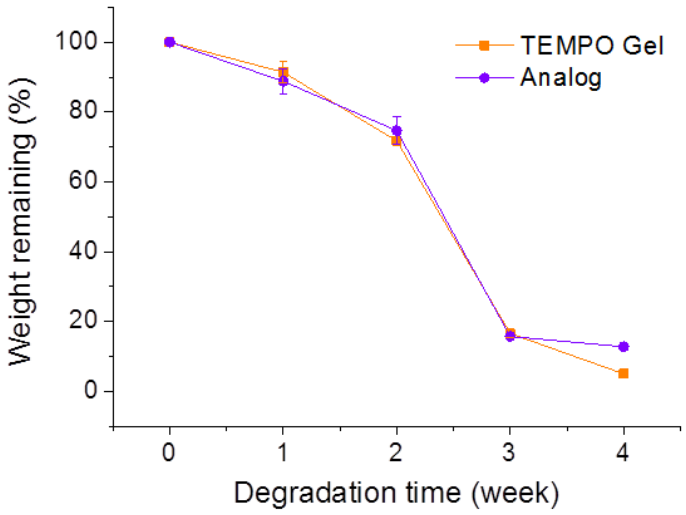


**Figure 4-4.** Weight loss profiles of TEMPO Gel and Analog.

### 4.3.4 **MRI of TEMPO Gel distribution**

The LV of rat heart after 30 min infarction and 24 h reperfusion appeared dark under T2-weighted MRI, as shown in **Figure 4-8a**. The signal was generated attributed to the hemorrhage in the infarction region. Bright signals distributed in separate dots presented on T1-weighted MRI images for hearts injected with TEMPO Gel, which attributed to the nitroxide radicals of 4-amino-TEMPO molecules in pNVMT polymer. The signals of the TEMPO Gel localized in the

LV regions overlapping with the dark area on T2-weighted MRI images (**Figure 4-8b**). No bright signals were found in rat hearts belong to the TEMPO Drug, Analog and PBS injection groups. 1 w after injection, the bright signals can still be seen in the TEMPO Gel injected hearts.

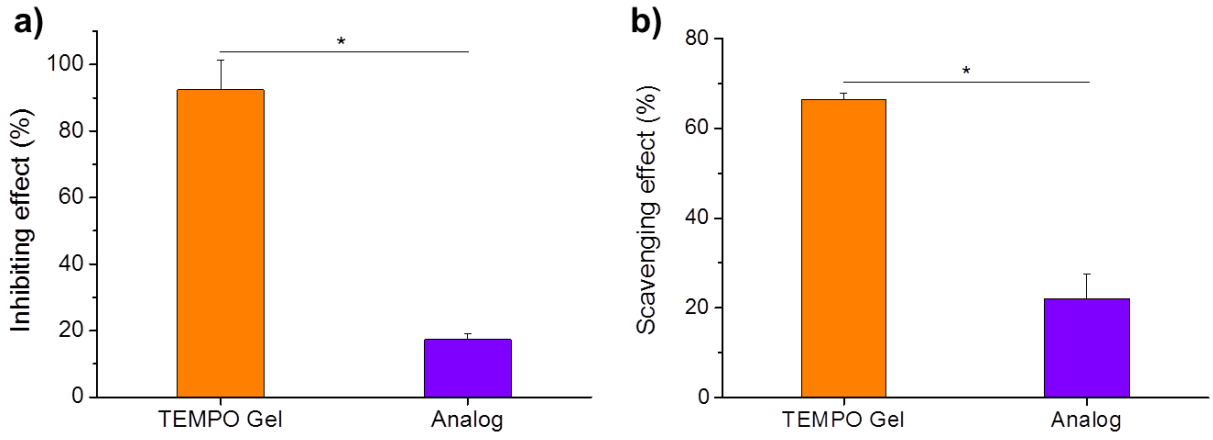


**Figure 4-5.** In vitro ROS scavenging effect of hydrogels. (a) Inhibition (%) on hydroxyl radical-generating Fenton reaction. (b) Effect (%) of scavenging superoxide radicals generated in Pyrogallol assay. * Significant differences, $p < 0.05$.

### 4.3.5 **Lipid peroxidation**

After 30 min infarction and 24 h reperfusion, MDA concentration in the hearts of PBS group increased significantly compared to of the healthy hearts as a result of lipid peroxidation (**Figure 4-9**). MDA concentration in the hearts of Analog group elevated significantly as well. Compared to PBS group, Analog injection did not mitigate MDA production compared PBS group. On the contrary, both TEMPO Drug and TEMPO Gel injection reduced lipid peroxidation compared to PBS group. The reduction effect of TEMPO Gel was greater than TEMPO Drug: both treatments

maintained MDA concentration as low as in the healthy hearts; MDA concentration in TEMPO Gel treated hearts was significantly lower than of the Analog group while no significant difference was observed between TEMPO Drug group and Analog group.

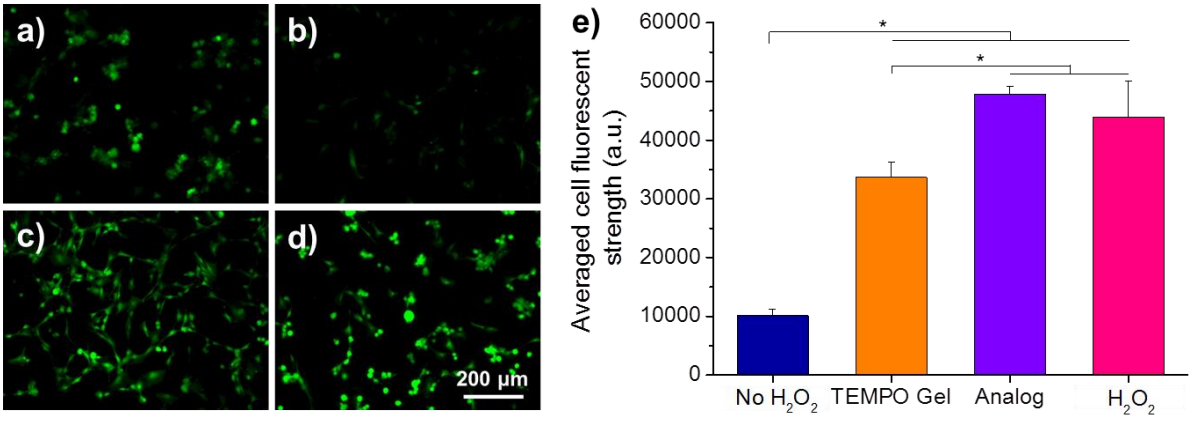


**Figure 4-6.** Intracellular ROS level in SMCs after $H_2O_2$ oxidative stress. (a-d) Carboxy-H2DCFDA staining of intracellular ROS, a: 500 μM $H_2O_2$ treatment for 30 min, b: Healthy control, c: 500 μM $H_2O_2$ treatment for 30 min with TEMPO Gel protection, d: 500 μM $H_2O_2$ treatment for 30 min with Analog protection. (e) Quantification of fluorescent strength averaged by cell area. * Significant differences, $p$ <0.05.

### 4.3.6 **Influence on mitochondrial metabolism in vivo**

The levels of semiquinone and FeS containing proteins were characterized by EPR for hearts after 30 min infarction and 24 h reperfusion. For all groups, corresponding peaks of FeS containing proteins (3488.0 G) can be clearly differentiated (**Figure 4-10a,b**). Slightly differently, the peak of semiquinone containing proteins (3372.0 G) in TEMPO Gel group was covered by a high intensity peak belong to the nitroxide radicals in TEMPO Gel, while other groups did not present such signal. This result is consistent with the MRI observation that only

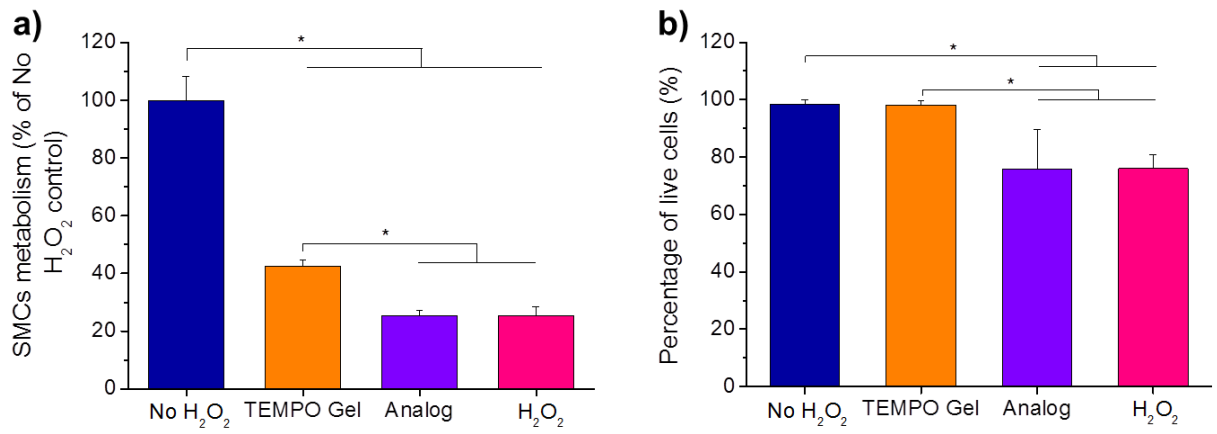


**Figure 4-7.** Protection effect on cell viability from $H_2O_2$ treatment by hydrogels. (a) Mitochondria metabolism characterized by MTS assay. (b) Percentage of live cells determined by live/dead staining. * Significant differences, $p < 0.05$.

TEMPO Gel group presented TEMPO signal. Quantitative results of semiquinone containing proteins exhibited same trend seen in the lipid peroxidation assay: peak intensities of PBS and Analog groups were significantly greater than of healthy control (**Figure 4-10c**). FeS containing proteins showed a similar trend among different groups. TEMPO Gel treated hearts had a lower concentration FeS containing proteins compared to hearts from PBS and Analog groups (**Figure 4-10d**).

### 4.3.7 **Cell apoptosis**

As determined by TUNEL staining, less than 1.5% cells in the LV of healthy hearts were apoptotic and the dead cell distributed evenly in IF, BZ and RM (**Figure 4-11**). No increase in percentage of dead cells was observed after 30 min ligation in none of the three areas (data not shown). After PBS injection 24 h after reperfusion, nearly 30% cells in IF and 16% cells in BZ

were died while the cells in RM areas were not fatally impacted by the infarction/reperfusion injury, as shown in **Figure 4-11**. TEMPO Drug treatment did not significantly mitigate cell apoptosis in LV compared to the PBS group despite the trend of lowered dead cell percentage in IF and BZ areas. Analog injection reduced cell deaths from 30% to 14% in highly risked IF area, while such effect were not as strong in BZ and RM areas. Among all treatment groups, TEMPO Gel treated hearts showed least cell apoptosis, also significantly lower than PBS injection group in IF and BZ areas (**Figure 4-11**).

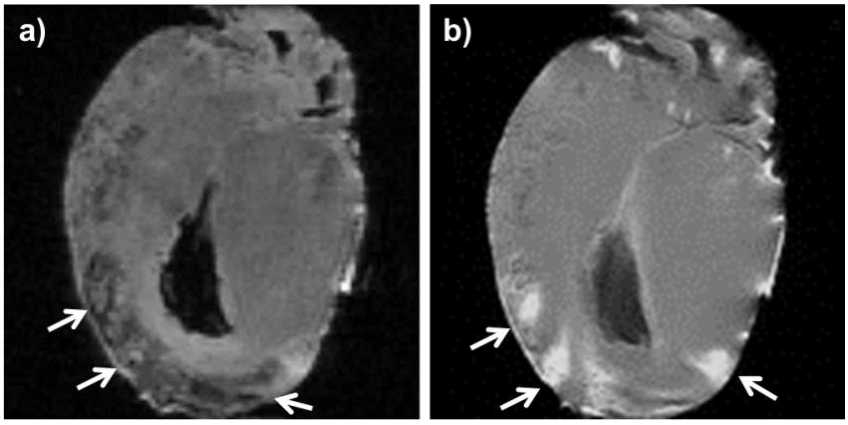


**Figure 4-8.** Magnetic resonance images of rat heart after infarction/reperfusion treatment and injected with TEMPO Gel. (a) T2-weighted image, arrows indicate the dark area representing hemorrhage. (b) T1-weighted image, arrows indicate the birght signal from nitroxide radicals in injected TEMPO Gel.

## 4.4 DISCUSSION

Several previous studies have developed antioxidant injectable biomaterials (particularly hydrogels) and evaluated their corresponding therapeutic potentials for MI with in vitro models.

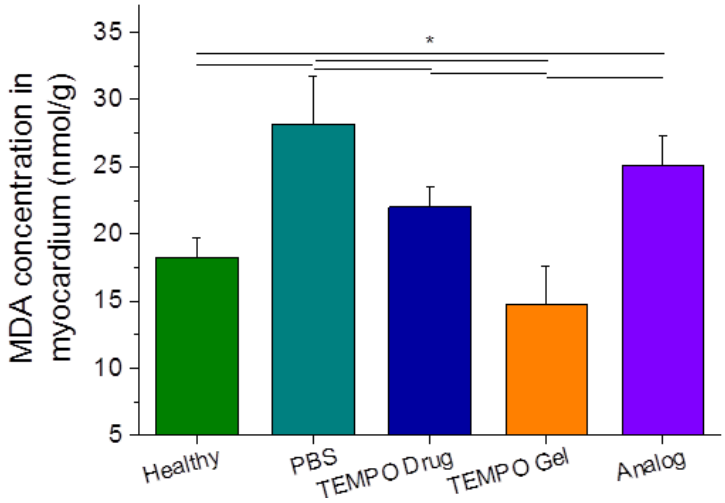


**Figure 4-9.** Protection effect by hydrogels on lipid peroxidation induced by oxidative stress. * Significant differences, $p < 0.05$.

Cheng et al. loaded a chitosan-gelatin-based hydrogel with ferulic acid (FA) and determined its effect in protecting Cisd2-deficient ($Cisd2^{-/-}$) cardiomyocytes under oxidative stress [42]. The FA loaded hydrogel effectively decreased the oxidative stress-induced damage and increased survive rate of $Cisd2^{-/-}$ cardiomyocytes by decreasing intracellular ROS production and increasing catalase activity [42]. Li et al. covalently conjugated glutathione (GSH) to chitosan chloride (CSCl), deriving CSCl-GSH hydrogels, which were shown to effectively scavenge ROS including the superoxide anion, hydroxyl radical and 1,1'-diphenyl-2-picrylhydrazyl radical (DPPH·) at high concentrations in a GSH grafting degree dependent manner [43]. CSCl-GSH hydrogels reduced intracellular ROS production and cardiomyocyte apoptosis under oxidative stress [43]. Cui et al. attached antioxidant tetraaniline (TA) to a poly(NIPAAm) based copolymer to form a thermally responsive hydrogel [44]. The TA containing hydrogel showed a time dependent DPPH· scavenging effect and protected cardiac myoblasts from ROS [44]. To the best

of our knowledge, our work is the first to evaluate the therapeutic effect of an injectable biomaterial incorporated with antioxidant moieties in an in vivo myocardial infarction model (with or without reperfusion).

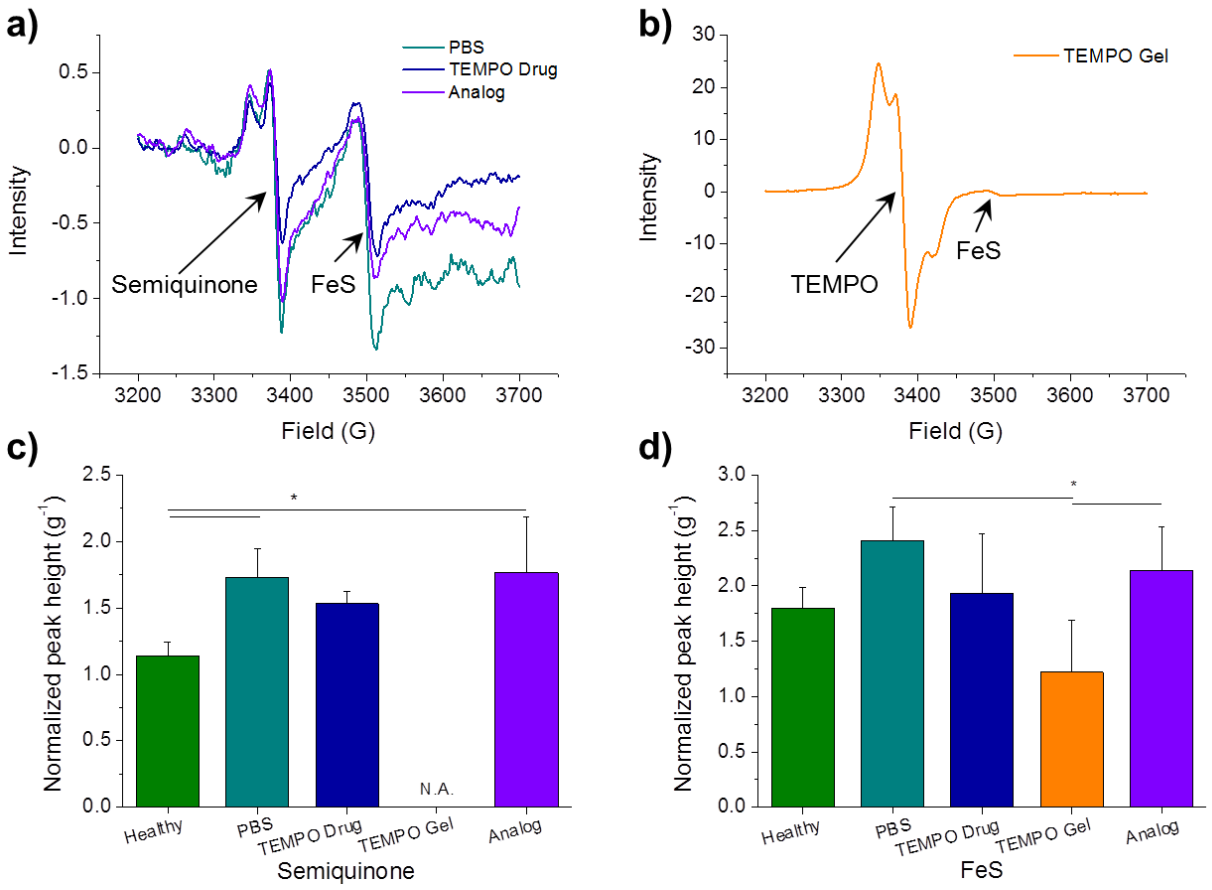


**Figure 4-10.** Influence by hydrogels on cardiac mitochondrial metabolism after infarction/reperfusion. (a,b) Representative EPR spectra of excised hearts form each group. (c,d) Peak heights of semiquinone and FeS signals normalized by tissue weight. * Significant differences, $p$ <0.05.

The ROS scavenger used in this study, 4-amino-TEMPO, contains a stable nitroxide radical, which provides TEMPO Gel the capacity to consume ROS. As confirmed by the color and EPR spectrum of pNVMT and the TEMPO Gel, the nitroxide remained stable during 4-

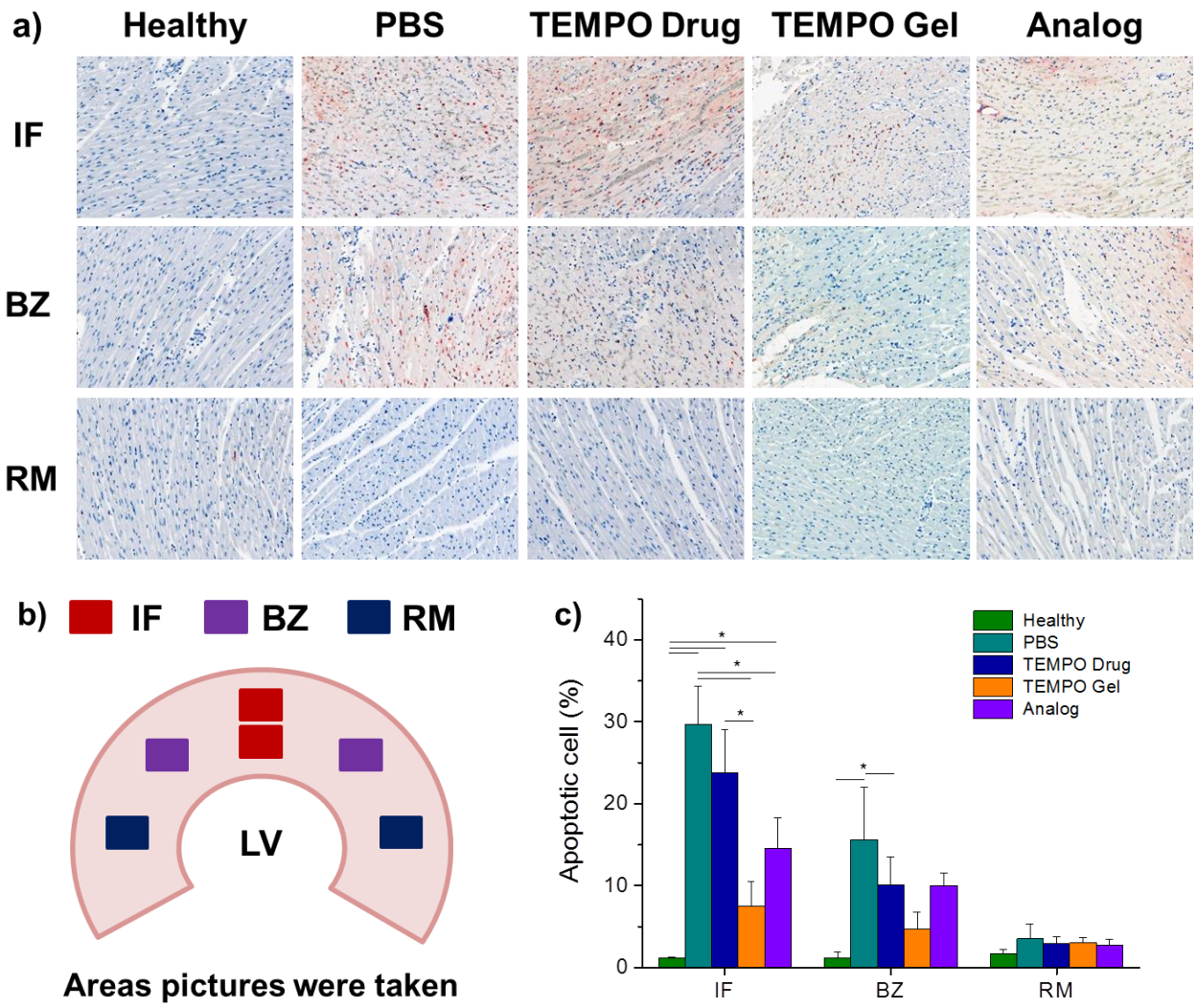


**Figure 4-11.** Cell apoptosis staining of rat LV 24 h after infarction/injection/reperfusion treatment. (a) Representative images from TUNEL staining of sections of each group. Blue: nuclei; red: apoptotic cells. (b) Locations of images taken representing infarction area (IF), border zone (BZ) and remote area (RM). Representative area of the Healthy group was assigned to the similar positions in other groups. (c) Percentage of apoptotic cells in IF, BZ and RM areas. * Significant differences, $p$ <0.05.

amino-TEMPO attachment and TEMPO Gel gelation. Nitroxides are considered general purpose antioxidant as they react with a wide spectrum of ROS: they catalyze the dismutation of superoxide radicals, facilitate catalase-like metabolism of H2O2, catalytically inhibit

peroxynitrite-mediated nitration and prevents Fenton signaling and hydroxyl radical formation [45-47]. A significant characteristic in the ROS scavenging mechanism of nitroxides is that they work like catalyzers. This derives another two major advantages of nitroxides: recyclability and high efficiency. For example, the reactions in superoxide scavenging by nitroxides have been summarized as (1) and (2). One nitroxide radical dismutate two equivalence of superoxide radicals and is then recovered. On the other hand, the effectiveness of 4-hydroxy-TEMPO in catalyzing the metabolism of cellular superoxide is significantly higher than frequently used antioxidants including vitamins and is similar to native superoxidase dismutase [48]. In addition, the diversity of the 4-position functional groups of 4-amino-TEMPO and its nitroxide makes them easy to attach to polymers.

$$RR'NO^{\bullet} + {}^{\bullet}O_{2}^{-} + 2H^{+} \rightarrow [RR'NO^{+}] + H_2O_2 \quad (1)$$

$$[RR'NO^{+}] + {}^{\bullet}O_{2}^{-} \rightarrow RR'NO^{\bullet} + O_2 \quad (2)$$

The ability of TEMPO Gel to scavenge a variety of ROS was confirmed by Fenton reaction inhibition, pyrogallol assay and cell culture under oxidative stress. As TEMPO Gel was suspended in the reaction solution and cell culture media in the hydrogel form, it did not have full contact with the soluble ROS. Despite this, TEMPO Gel managed to inhibit the production of hydroxyl radicals and scavenge superoxide radicals in the chemical reactions at high percentages, showing the high ROS scavenging efficiency of the attached nitroxide radicals. The minimal scavenging effect observed with the Analog may be attributed to separation of reactants caused by limited diffusion of reactants absorbed within and in-and-out the hydrogel matrix. Similarly, despite the same inevitable loss of nitroxide diffusability due to covalent linkage onto the hydrogel, SMCs survived the oxidative stress. This effect was particularly important as it

prevented the damage which may have been caused by the potential burst released cell content (including intracellular ROS produced as a result of oxidative injury) as the live cell membranes were kept intact.

Consistent with the in vitro observations, the myocardium was protected from oxidative injury by TEMPO Gel, as shown by the levels of membrane peroxidation and mitochondrial metabolism, which is believed to lead to the higher survive rate of resident cells in LV. In contrast, local administration of free TEMPO Drug did not rescue as many cells. EPR and MRI results agreed that free TEMPO molecules were cleaned from LV within 24 h, which explained the differences in the protection effect and demonstrated the efficacy of the design of covalent bonding of TEMPO to polymer backbone. Although not explored in this study, it can be predicted that physically mixing TEMPO with hydrogel prior to injection could not significantly prolong the retention of the free drug, judging by the release profile of growth factors from intramyocardially injected hydrogel [49]. It is worth noting that more cells survived the infarction/reperfusion injury in the Analog treated group compared to PBS control without ROS scavenger. This unreported phenomenon may be attributed to the lowered wall stress by hydrogel injection and the resulting mitigated apoptotic signaling.

In this study, timely, wide-spread and extended bioavailability of ROS scavenging TEMPO has been achieved and exhibited translational potentials. The hydrophilicity of TEMPO Gel is close to previously reported poly(NIPAAm-co-VP-co-MAPLA) (VP15) hydrogel developed in our lab [38]. Therefore TEMPO Gel has a similar transition temperature and was able to diffuse through the myocardium and cover the risk areas, as observed under MRI. VP15 has been transepicardially delivered into beating porcine heart in a planned square pattern using a minimally invasive robot, thus potentially in a clinical setting TEMPO Gel can be injected using

such technique to desired locations and interact with ROS in a large volume of myocardium through diffusion. On the other hand, bioactive TEMPO remained in the injection area for at least a week, which can be attributed to the catalytic characteristic of TEMPO and the covalent bonding of TEMPO to the hydrogel. Extended retention of polymer bound TEMPO has been proven critical as TEMPO Drug was cleaned in 24 h and corresponding treatment did not show as good therapeutic effect.

Despite the encouraging results from the short-term study post infarction/reperfusion, the long-term in vivo influence on cardiac function still needs to be evaluated. One of the limitations of this study is the lack of evaluation on the effect of TEMPO concentration in hydrogel. On the other hand, cautions need to be taken in future large animal studies on the choice of injection time. Although injecting hydrogels shortly prior to reperfusion has been proven safe in the rat model, feasibility of applying such slightly aggressive procedure in patients is still open to question before being verified in a clinical setting.

## 4.5 CONCLUSION

In this study the mechanical support from injectable hydrogel was combined with the antioxidant effect from a ROS scavenger, TEMPO, producing a bioactive injectate (TEMPO Gel) for intramyocardial injection therapy. The covalently attached TEMPO presented high antioxidant activity and ROS scavenging efficiency in vitro when the polymer was in the hydrogel form. In a rat infarction/reperfusion model, TEMPO Gel mitigated the oxidative injury and rescued cells from entering the apoptotic process after 24 h treatment. Longer retention of TEMPO in TEMPO Gel was observed under MRI compared to free TEMPO Drug, which explained the lack of

therapeutic effect in vivo from the latter. Analog without ROS scavenger exhibited no antioxidant property, but decreased cell death in the short-term study. To further evaluate the therapeutic effect of integrative strategy, long-term cardiac function study needs to be done.

# 5.0 POROUS INJECTABLE HYDROGEL FOR FASTER CELL INFILTRATION AND PRO-M2 MACROPHAGE POLARIZATION

## 5.1 INTRODUCTION

Biodegradable injectable hydrogels have found extensive applications in intramyocardial injction therapy for myocardial infarction. One of the advantages of injectable hydrogels is that they can be delivered minimally invasively in designed and controlled manners [30, 105, 191]. In addition, the biodegrability of injectable hydrogels allows tissue regrowth and remodeling. The physiological activities in neotissue development follow specific temporal patterns. While tissue ingrowth could be inhibited by slow hydrogel degradation and results in prolonged undesired material-tissue interaction and scarring, unmatched fast degradation could lead to failure in mechanical support and adhesive substrate for cell infiltration [192, 193]. Efforts have been made to match the degradation rates of hydrogels to the temporal requirements to achieve maximal beneficial effects. As hydrogels usually form nonporous crosslinked swollen masses upon injection, one strategy is to incorporate enzyme cleavable sites to allow cells to actively erode their way through the hydrogels [194, 195]. The other strategy is to tune hydrogel degradation rate by controlling the crosslinking density or hydrolytical potential [98, 196]. However, significant degradation of injected hydrogels would compromise their integrity, which is not favored for injection therapy relying on long term mechanical support. Recently, concepts

have been developed to generate porous structure within hydrogels to provide pathways for cell infiltration and tissue integration before hydrogels collapse [192, 197]. Griffin et al. employed microspherical hydrogel building blocks to assemble crosslinked porous scaffold in situ [192]. Bencherif et al. squeezed an elastic porous hydrogel through a needle and the subsequent shape recovery opened the pores in vivo [197]. The poly(N-isopropylacrylamide) (PNIPAAm) based hydrogels developed in our lab quickly solidify from low temperature solution at body temperature and stay intact in the injection site for weeks before degradation without signs of cell infiltration [61, 114]. As the two previously mentioned methods to form pores in vivo are not compatible with hydrogels having the similar rapid in situ gelation mechanisms, we developed a novel method to fabricate porous injectable hydrogels. Mannitol microparticles were mixed and injected with poly(NIPAAm-co-VP-co-MAPLA) (VP: N-vinylpyrrolidone, MAPLA: methacrylate-polylactide) hydrogel as porogens to form pores shortly after injection.

In addition to supporting cell infiltration and tissue integration, managing foreign body response is another important and difficult issue. Similar to other implanted medical devices, injectable hydrogels induce foreign body responses, which begin from nonspecific protein adsorption onto hydrogel surface and chemoattractants release by platelets and the clot following blood-material interactions [118, 198]. Consequently, these proteins and chemoattractants recruit macrophages to the injection sites, and the latter adhere onto the hydrogel surface via binding to the adsorbed proteins [118, 199-202]. Adherent macrophages are subsequently activated, results in secretion of the pro-inflammatory cytokines and material degrading enzymes, macrophage fusion generating foreign body giant cells, and crosstalk with fibroblasts promoting collagen deposition and encapsulation of the injected hydrogel [203-206]. On the other hand, it is known that macrophages can be activated into several heterogeneous phenotypes including classically

activated macrophages (M1) which promote inflammation and alternatively activated macrophages (M2) which are anti-inflammatory [207]. Therefore, modulating macrophage behavior is the key to mediate the foreign body responses for injectable hydrogels. Vegas et al. identified that triazole modified alginate hydrogel inhibited recognition by macrophages and fibrous deposition among a library of modified alginate hydrogels, although the mechanism is not clear [119]. Zhang et al. employed the superhydrophilicity of zwitterionic polymers to form nondegradable hydrogels with low protein adsorption level, as a means to reduce the activation of macrophages [198]. In addition to a less dense deposition of collagen, an inclination of macrophage polarization toward M2 phenotype on zwitterionic hydrogels compared to the control was found. Instead of reducing the recruitment or activation of macrophages, actively encourage the M2 polarization of recruited macrophages may theoretically lead to a more favorable remodeling process, especially for porous hydrogels which invite the infiltration of cells including macrophages. Decelullarized extracellular matrices (ECM) and their derivative products have shown strong effects on promoting macrophage polarization toward M2 phenotype and constructive remodeling in regenerative applications. Coating of ECM component on implantable medical devices mitigated the foreign body response in vivo. Recent advance has identified the matrix-bound vesicles as the main functional component in ECM products. Among the variety of ECM products, digested ECMs hold a liquid form at low temperature which allows thorough mixture with the thermally responsive poly(NIPAAm-co-VP-co-MAPLA). Therefore, we explored the possibility of modulating the polarization of the recruited marcrophages by adding digested decellularized ECM to our porpous injectable hydrogel.

In this study, we aim to develop a platform technique for fabricating porous injectable hydrogel for faster cell infiltration and pro-M2 macrophage polarization to address two major

issues associated with the performance of injectable hydrogel materials in MI treatment application. Our hypotheses are two folds. First, highly soluble porogen particles can leave pores shortly after injection of hydrogels with rapid in situ gelation mechanisms. Secondly, mixing digested ECM containing matrix-bound vesicles and other bioactive components can polarize the recruited (especially the infiltrated) macrophages toward more favorable M2 phenotype. As the mainstream of injectable hydrogels employs rapid, in situ gelation mechanisms, and by principle it is easy and convenient to mix the porogen and digested ECM with hydrogel precursors prior to injection procedures, we expect that this platform technique can be transferred to a wide spectrum of injectable hydrogels with little difficulties. To test our hypotheses, thermally responsive poly(NIPAAm-co-VP-co-MAPLA) was chosen as the representative hydrogel, and mannitol particles and digested urinary bladder matrix (UBM) were selected as the porogen and the bioactive ECM component. A rat hindlimb muscle injection model was employed to characterize the pore formation, cell infiltration and macrophage polarization processes, as shown in **Scheme 5-1**.

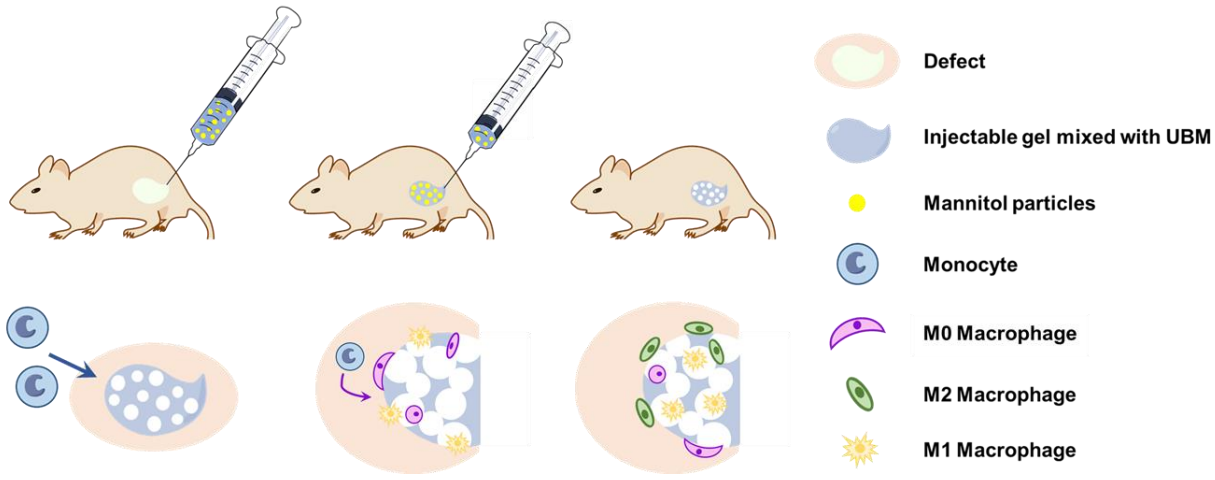


**Scheme 5-1.** Faster cell infiltration and pro-M2 macrophage polarization in the porous injectable hydrogel.

## 5.2 MATERIALS AND METHODS

### 5.2.1 Materials

All chemicals were purchased from Sigma-Aldrich unless otherwise stated. N-isopropylacrylamide (NIPAAm) was purified by recrystallization from hexane and vacuum-dried. 2-Hydroxyethyl methacrylate (HEMA) was purified by vacuum distillation. Vinylpyrrolidone (VP), lactide, benzoyl peroxide (BPO), sodium methoxide (NaOCH3), methacryloyl chloride, methacrylic acid (MAA) and other solvents were used as received. D-mannitol particles were sieved to obtain the portion between 170 mesh and 230 mesh.

### 5.2.2 Synthesis of methacrylate polylactide (MAPLA)

The synthesis of methacrylate polylactide was performed as previously described [113]. Briefly, $NaOCH_3$/methanol was added to a lactide/dichloromethane solution to synthesize polylactide (HO-PLA-$OCH_3$) through ring-opening polymerization. MAPLA was synthesized by dropping methacryloyl chloride into a HO-PLA-$OCH_3$/dichloromethane solution containing triethylamine. Dichloromethane was removed by rotary evaporation and the product was purified by flash chromatography to obtain MAPLA with yields of ~60%.

### 5.2.3 Synthesis of poly(NIPAAm-co-VP-co-MAPLA) (VP10)

Poly(NIPAAm-co-VP-co-MAPLA) copolymers were synthesized from NIPAAm, VP and MAPLA by free radical polymerization as previously described [105]. The feed ratios of

NIPAAm, VP and MAPLA were 80/10/10 , and the corresponding product polymers were named as VP10. Monomers (0.066 mol) were dissolved in 180 mL of 1,4-dioxane containing 0.23 g BPO. The polymerization was carried out at 70°C for 24 h under an argon atmosphere. The copolymer was precipitated in hexane and further purified by precipitation from THF into diethyl ether and vacuum-dried, with yields of ~80%.

### 5.2.4 **Preparation of urinary bladder matrix (UBM) digest**

Urinary bladder matrix (UBM) digest was prepared as previously described [208]. Briefly, porcine bladders were obtained from market weight pigs (Thoma Meat Market) immediately following euthanasia. Excess connective tissue and residual urine was removed. The tunica serosa, tunica muscularis externa, the tunica submucosa, and the tunica muscularis mucosa were then mechanically removed. The luminal surface was rinsed with 1.0 N saline solution to dissociate urothelial cells of the tunica. The resulting material was composed of the basement membrane of the urothelial cells plus the subadjacent lamina propria, or UBM. UBM sheets were then placed in a 0.1% (v/v) peracetic acid solution, 4% (v/v) ethanol, and 95.9% (v/v) sterile water for 2 h. To remove peracetic acid, UBM was washed twice for 15 min with PBS followed by two 15 min washes with sterile water. UBM sheets were then lyophilized. Lyophilized UBM was powdered using a Wiley mill and filtered through a 40 mesh screen. The powdered material was solubilized at a concentration of 10 mg/mL in 0.1 mg/mL pepsin in 0.01 N HCl at a constant stir rate of 48 h. The ECM digest solution was then frozen until use in further experiments. The digest was neutralized to a pH of 7.4 using NaOH and diluted in PBS to the desired concentration.

### 5.2.5 **Hydrogel preparation**

Nonporous hydrogel (NP) is prepared by dissolving VP10 in PBS (10 wt%). Nonporous hydrogel with ECM component (NPE) was obtained by mixing 20 wt% VP10 in PBS and 10 mg/mL UBM digest (1:1 v/v). Porous hydrogel without ECM component (PM) was prepared by adding 30 wt% mannitol particles to the NP formula and mixing with a syringe. Pores were formed after PM gelation at 37ºC and dissolution of the mannitol particles. Similarly, porous hydrogel with ECM component (PME) was prepared by adding 30 wt% mannitol particles to the NPE formula and mixing with a syringe.

### 5.2.6 **Characterization of physical properties of hydrogels**

Mannitol release from the PM and PME hydrogels were characterized by quantifying the dissolved mannitol in the supernatant of hydrogel/PBS system. 0.5 mL of PM or PME hydrogel was injected into 10 mL 37ºC PBS in 30 s after mixing the hydrogels with mannitol. Supernatants were collected at different time intervals and replaced with fresh 37 ºC PBS. Mannitol concentration in the supernatants were quantified with mannitol assay (Sigma-Aldrich, USA) and the cumulative release was of calculated accordingly.

Subsequent to 24 h gelation in 37ºC phosphate buffered saline (PBS), NP, PM and PME hydrogels were frozen in liquid nitrogen, cut to expose the intersection and freeze-dried. The hydrogel samples were observed with scanning electron microscope (SEM). Pores size of PM and PME hydrogels were measured with ImageJ on the SEM pictures.

Matrix-bound vesicles (MBVs) in the aforementioned supernatants were isolated as previously described [209]. Supernatants of the PM and PME groups from the release study were

subjected to successive centrifugations at 500g (10 min), 2500g (20 min), and 10,000g (30 min) to remove collagen fibril remnants. Each of the above centrifugation steps was performed three times. The fiber-free supernatant was then centrifuged at 100,000g at 4°C for 70 min to concentrate the MBVs and remove the dissolved polymer. The 100,000g pellets were washed and suspended in 500 µl of PBS and passed through a 0.22-µm filter (Millipore). TEM imaging was conducted on negative stained MBVs loaded on Cu grids.

Protein content in the supernatants of PME group obtained in the mannitol release study were quantified with BCA assay (Sigma-Aldrich, USA). The cumulative release was of calculated accordingly.

To measure the mechanical properties of the hydrogels, samples from the NP, PM and PME groups were incubated in a 37°C water bath for 24 h to reach a stable water content, obtaining hydrogel discs. An ElectroForce 3200 Series II (Bose, Minnesota, US) equipped with a 10 N load cell was utilized to record the compression-force curve immediately after the samples were taken out of the water bath. Compression modulus were calculated accordingly.

Hydrogel degradation was quantified by mass loss measurements. Hydrogels with known initial dry masses (~40 mg) were immersed into 4 mL of PBS containing 50 U/mL type I collagenase at 37°C. At predefined time points over a 4 week period the hydrogels (n=3 each) were lyophilized and the relative mass loss was recorded.

### 5.2.7 **Cytotoxicity of mannitol and released products from hydrogels**

The cytotoxicity of the mannitol was assessed by measuring the relative metabolic activity of rat vascular smooth muscle cells (SMCs) cultured in Dulbecco's modified Eagle medium (DMEM) (Gibco, Life technologies) with 10% fetal bovine serum (FBS), 1% penicillin/streptomycin, and

supplemented with graded concentrations of mannitol. SMCs were seeded at an initial density of 30,000/cm$^2$ and their metabolic activity after 24 h culture was measured (n=6 each) using an MTS assay kit (Promega CellTiter 96 Cell Proliferation Assay).

Similar to the mannitol release study, 0.5 mL of NP, PM and PME hydrogels were immersed in 10 mL PBS for 24 h without PBS replacements. The effect of the released products from NP, PM and PME hydrogels on SMCs proliferation was assessed by measuring the relative metabolic activity of the cells cultured in DMEM with 10% FBS, 1% penicillin/streptomycin, and supplemented with 10% supernatants collected from the release experiment. SMCs were seeded an initial density of 15,000/cm$^2$ and their metabolic activity after 24 h, 3 d and 7 d culture was measured (n=6 each) using an MTS assay kit. Culture media supplemented with PBS instead of released products were included as the control group.

### 5.2.8 **Cell migration study**

Bone marrow-derived macrophages were harvested from 2 month old C57/BL6 mice as previously described [210]. Briefly, femur and tibiae were harvested and separated from muscle and connective tissue. Bones were cut at either end to expose bone marrow. Bone marrow was flushed out using macrophage differentiation media (DMEM/10% FBS/10% L-929 Supernatant/1% PenStrep/2% NEAA/1% HEPES/0.2% β-2 mercaptoethanol). Bone marrow lysate was reconstituted in media and filtered through a sterile cell filter. Cells were plated in 6 well plates and cultured for 7 d in media to differentiate them into macrophages.

0.5 mL of NP, PM and PME hydrogels were immersed in 10 mL DMEM for 24 h without DMEM replacements. The effect of the released products from NP, PM and PME hydrogels on macrophage migration was evaluated with CytoSelect cell migration assay (Cell Biolabs, USA)

according to manufacturer's instruction. 500 μL released product was added to the lower well of the migration plate. 150,000 macrophages were added to the inside of each insert (n=4 each group). DMEM only was used as control.

### 5.2.9 **In vivo hydrogel injection studies**

Adult female Lewis rats weighing 160−210 g were utilized in a protocol that followed the National Institutes of Health guidelines for animal care and that was approved by the University of Pittsburgh's Institutional Animal Care and Use Committee. Anesthesia was induced with 3.0% isoflurane inhalation with 100% oxygen followed by 1.5-2% isoflurane with 100% oxygen during procedure. Dermatotomy was performed to expose the inner thigh muscles on both legs. Single injections of 200-250 uL of hydrogel were made approximately 3 mm deep in the muscle bed. For each hydrogel, 18 injections in 18 legs were made. Inner thigh muscles from 2 legs each of NP, PM and PME group were excised 3 min after injection. The muscles were incised to expose the hydrogels, and images were taken with a Dino-Lite (AM4113T-GFBW, AnMo Electronics, New Taipei City, Taiwan) under brightfield mode. After 3d and 21 d, 4 rats from each group at each time point were sacrificed and the inner thigh muscles encompassing the hydrogels were excised, and the tissue was fixed in 10% formaldehyde for 3 d before embedding. Trichrome staining and immunohistochemical staining with monoclonal antibodies against CD68 (1:200, Abcam, USA), CD86 (1:150, Abcam, USA) and CD206 (1:200, Santa Cruz, USA) was performed. CD68 was co-stained with CD86 and CD206 separately. A red secondary antibody was used for CD68, green secondary antibodies were used for CD86 and CD206. Nuclei were stained with 40',6-diamidino-2-phenylindole (DAPI; 1:10000, Sigma). Microscopic images were taken under fluorescence microscopy.

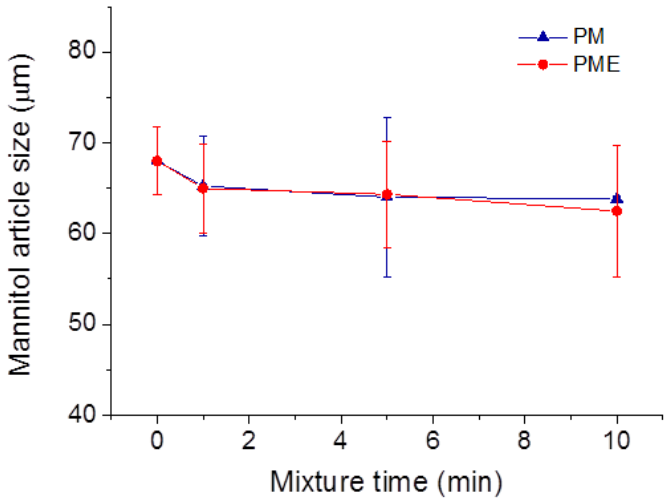


**Figure 5-1.** Size change of mannitol particles in cold hydrogel mixture.

Cell densities around and in the hydrogel injection sites for each group at day 3 and day 21 were analyzed from the microscopic images using ImageJ. M1 macrophages were identified by CellProfiler as $CD68^+/CD86^+$/DAPI cells. M2 macrophages were identified by CellProfiler as $CD68^+/CD206^+$/DAPI cells.

### 5.2.10 **Statistical analyses**

For the paired comparisons, a t-test was employed. Where three or more groups were being compared, one-way ANOVA was employed with Tukey's test applied for specific comparisons. Results are presented as the mean with standard deviation. Statistical significance was defined as $p < 0.05$.

## 5.3 RESULTS

### 5.3.1 Porous hydrogel formation

As Shown in **Figure 5-1**, sieved mannitol particles have an initial size of 68.0 μm. After mixture with VP10 hydrogel solution for 10 min, the particle size did not decrease significantly. In addition, there was no significant size difference between particles mixed with or without UBM digest in the hydrogel. After injecting the hydrogel/mannitol mixtures into 37°C PBS, the mixtures instantly solidified, and mannitol was rapidly dissolved and released from the hydrogel mass. After 24 h, 80% mannitol was released from the hydrogel of PM group, whereas 100% mannitol was released from the hydrogel of PME group, as shown in **Figure 5-2a**.

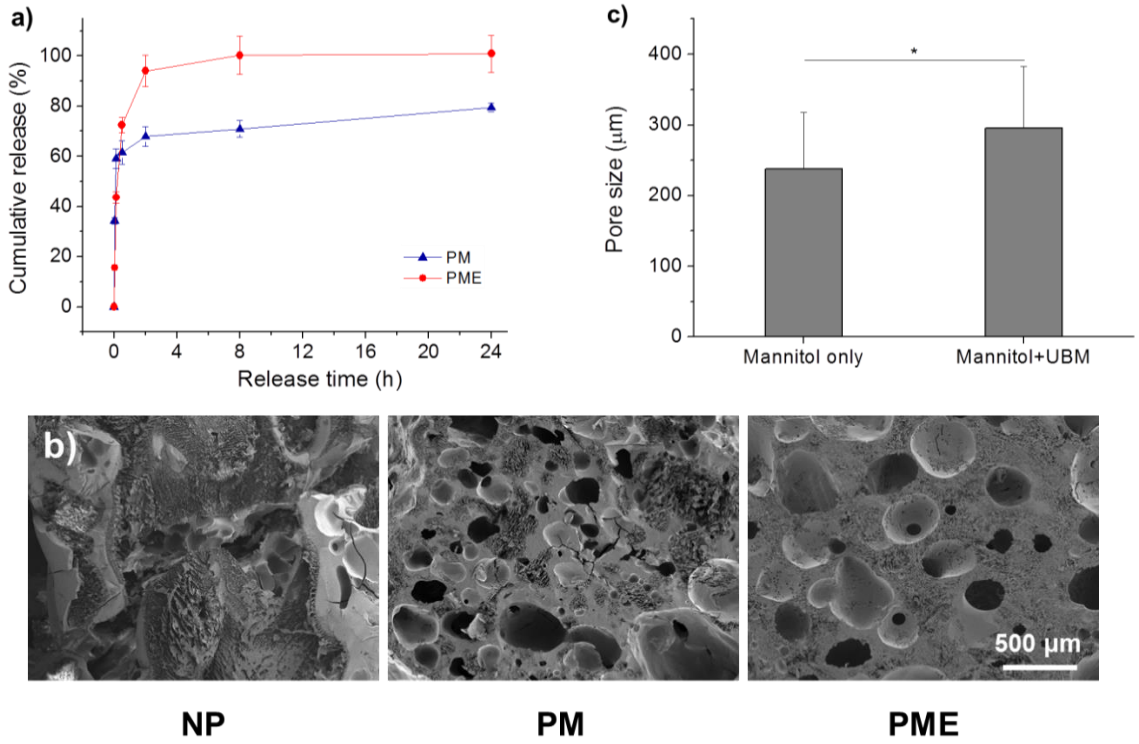


**Figure 5-2.** (a) Mannitol release from PM and PME hydrogels. (b) SEM images of intersections of freeze-dried hydrogel 24 h after gelation. (c) Pore size of porous PM and PME hydrogels. * Significant differences, $p$ <0.05.

Densely packed pores can be observed in the hydrogels of PM and PME groups after 24 h of gelation, as opposed to the nonporous hydrogel mass of NP group (**Figure 5-2b**). The majority of the pores found in PM and PME groups were elliptical. The pore size of PM group was 237±80 μm, significantly smaller than the pore size of PME group, which is 295±87 μm (**Figure 5-2c**). In addition, channels wider than 50 μm can be observed on the walls of pores, making the pores connected (**Figure 5-2b**).

### 5.3.2 **Release of UBM component**

Matrix-bound vesicles (MBVs) were found by TEM in the supernatant 2 min after hydrogel immersion in 37ºC PBS, as shown in **Figure 2a**. The MBVs showed a typical size as previously reported and remained intact [209].

The protein content of UBM mixed in the hydrogel was rapidly released. 48% of total protein was released within 30 min of gelation, 70% was released 24 after gelation (**Figure 5-4a**). As shown in **Figure 5-4b,c**, the released proteins covered the same molecular weight

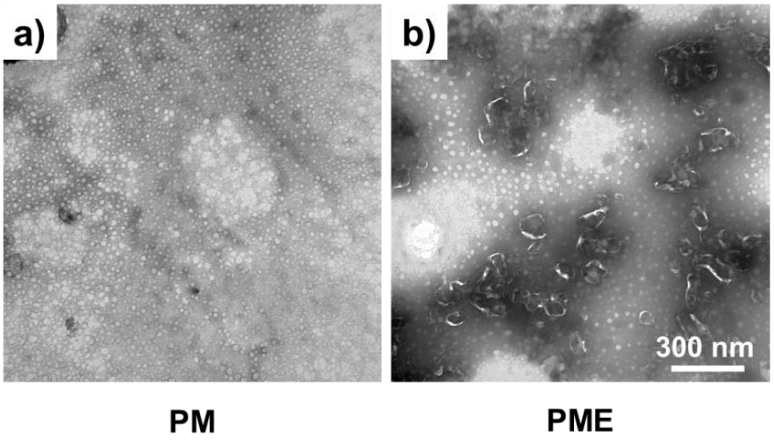


**Figure 5-3.** TEM images of supernatant2 min after gelation of PM and PME in PBS.

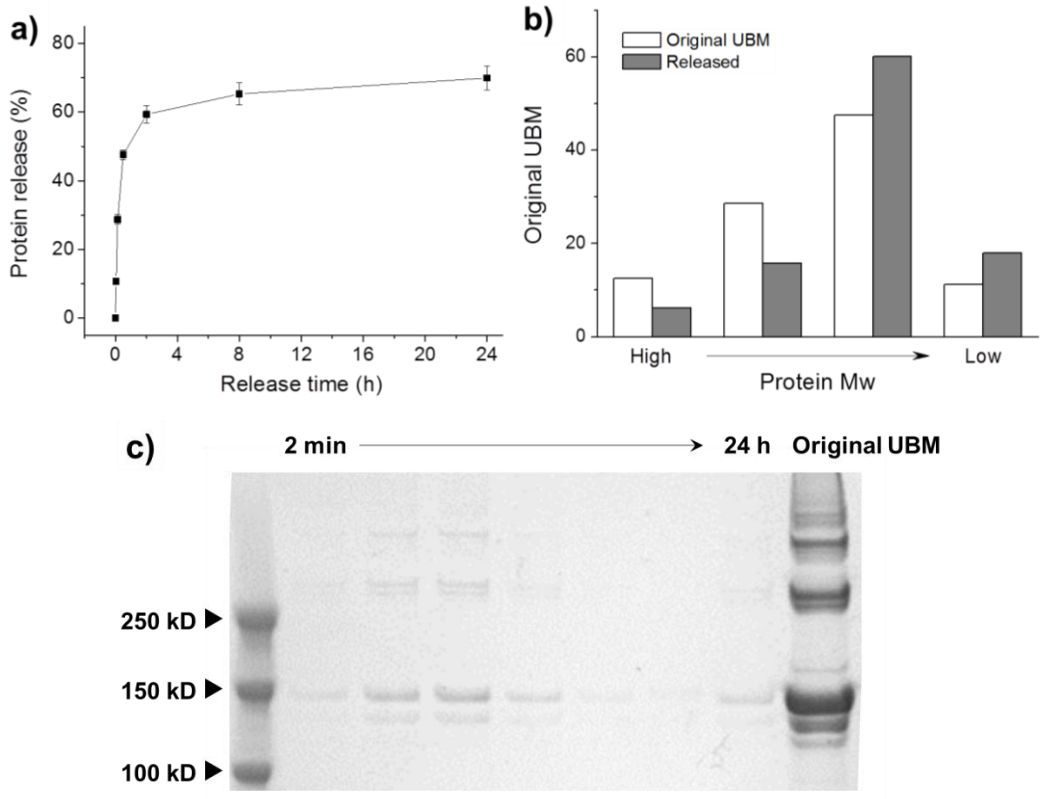


**Figure 5-4.** (a) Protein release profile of PME hydrogel. (b) Molecular weight distribution of proteins of original UBM and proteins released from PME hydrogel in 24 h. (c) WB of released proteins from PME hydrogel in comparison with original UBM.

spectrum of the original UBM. However, proteins with smaller molecular weight released faster than larger proteins. Along with the proteins, endotoxins carried by the UBM digest also released to the supernatant (**Figure 5-5**).

### 5.3.3 **Physical properties of porous hydrogel**

The compression modulus of the nonporous hydrogel (NP group) was 272±38 kPa. Pore structures significantly decreased the compression modulus to 106±8 kPa and 87±6 kPa for PM

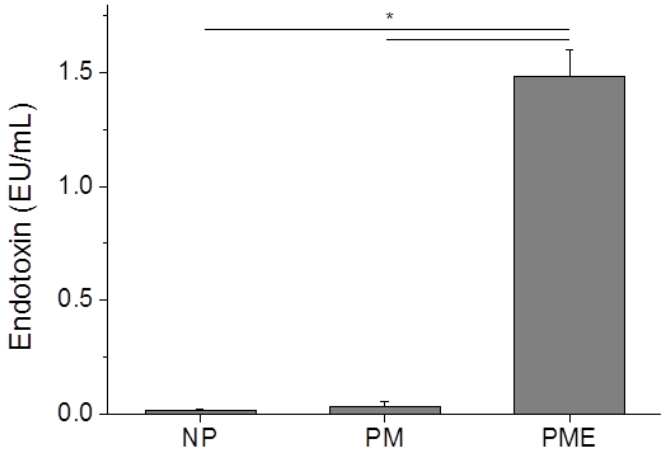


**Figure 5-5.** Endotoxin released from hydrogels. * Significant differences, $p < 0.05$.

group and PME group, respectively (**Figure 6a**). There was no difference in terms of degradation rate, hydrogel of PME group lost weight in PBS faster than NP and PM groups. As shown in **Figure 6b**, PME hydrogel lost 50% weight in 2 weeks in collagenase/PBS, while similar weight loss took 3 weeks for the other two groups.

### 5.3.4 **Influence of hydrogel on cell behaviors**

Dissolved mannitol did not show cytotoxicity on SMCs up to 100 mM, as shown in **Figure 7a**. Comparing to SMCs treated PBS, SMCs treated with products released from the hydrogels did not show effects on proliferation over a week (**Figure 7b**). SMCs significantly proliferated during the culture period, neither mannitol, proteins, MBVs nor other components promoted or inhibited cell proliferation over this period as evaluated with cell mitochondrial functions (**Figure 7b**). On the other hand, the released products from PME hydrogel attracted macrophages

to migrate through 8 μm membrane towards the high concentration source, as shown in **Figure 5**. Released products from the other two groups did not show significant effect on macrophage migration comparing to the PBS group (**Figure 8**).

### 5.3.5 **Cell infiltration into hydrogel in vivo**

Immediately after injection into rat hindlimb, hydrogel from all three groups solidified and formed hydrogel mass in the muscle bed as a result of temperature increase. As shown in **Figure 5-9**, clear boundaries can be identified between the hydrogels and the muscle. For the hydrogel from the NP group, hydrogel mass was continuous and homogeneous, whereas pores can be found in injected PM and PME hydrogels (pointed by arrows in **Figure 5-9**). In addition, similar to the in vitro result, channels between pores can be found in the PM and PME hydrogels.

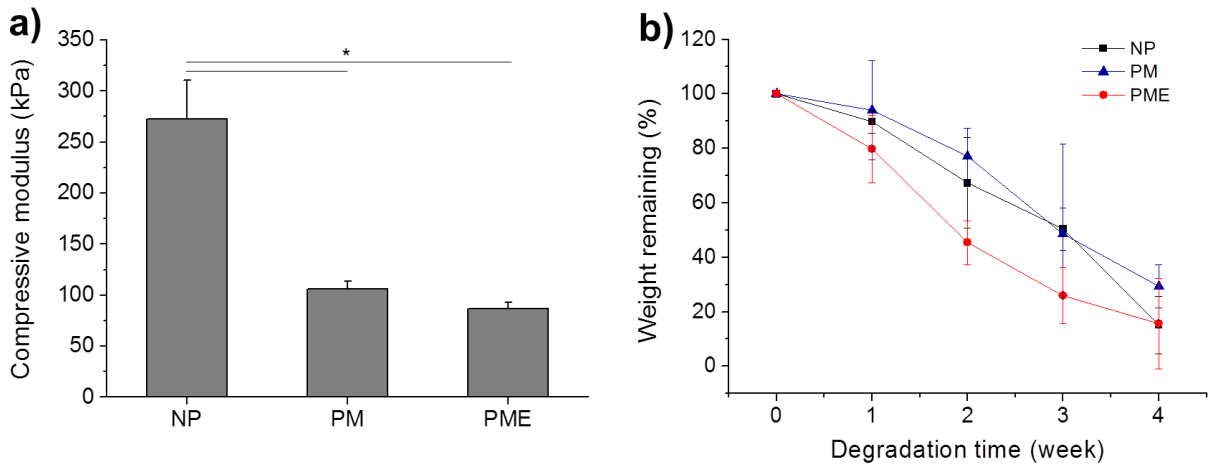


**Figure 5-6.** (a) Compressive modulus of hydrogels. (b) Weight loss profiles of hydrogels. * Significant differences, $p < 0.05$.

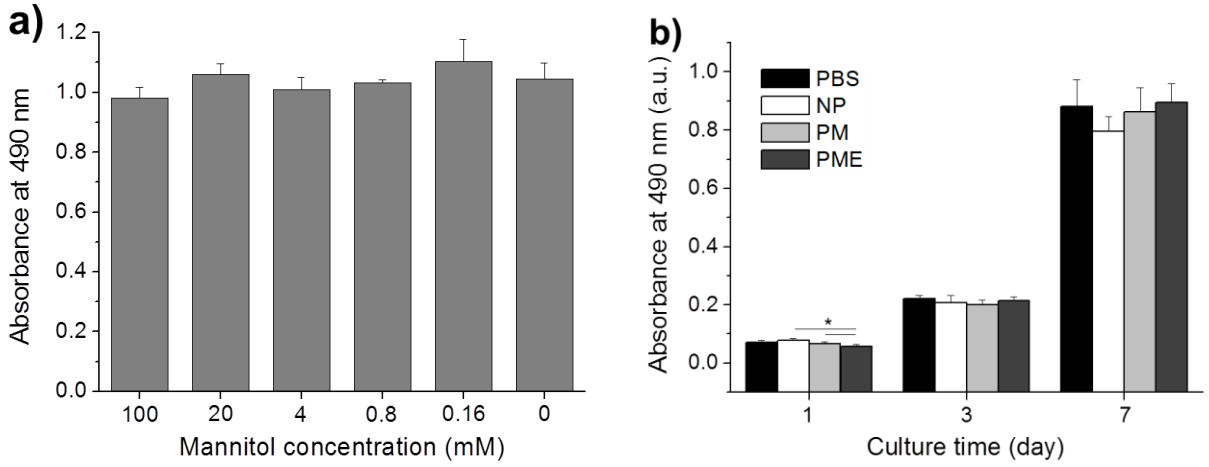


**Figure 5-7.** (a) Cell viability of SMCs after mannitol treatment. (b) SMCs proliferation with release product from hydrogels. * Significant differences, $p < 0.05$.

3 d after injection, rat leg muscle with injected hydrogels were sectioned and stained. On DAPI stained images, hydrogel injection sites can be identified in all three groups. In NP and PM groups, empty holes with no cell nuclei within the region were observed, corresponding to the injected hydrogels, encompassed by a capsule of densely packed cells with ~100 μm thickness (**Figure 5-10a**). These phenomena were consistent with typical features of foreign body response. A similar capsule of cells can be found around the injected hydrogel in the PME group. On the contrary to other two groups, cells were present in the hydrogel area, with a lower density compared to the cell density in the capsule (**Figure 5-10a**). What is worth noting is that not the entire hydrogel injection site was infiltrated by cells - the core of the PME hydrogels remained cell-free at 3 d after injection. As for the NPE group (non-porous VP10 hydrogel mixed with UBM digest), extrusion of cells from the hydrogel/capsule edge to the hydrogel can be observed (data not shown). However, the cells did not penetrate as far as in the PME group. The enlarged trichrome staining images agreed with the DAPI staining images, capsules featured with a higher

cell density and an extracellular matrix distinct from the muscle bed encapsulating the NP, PM and PME hydrogels: only in the PME group have cells infiltrated into the hydrogel mass (**Figure 5-10b**).

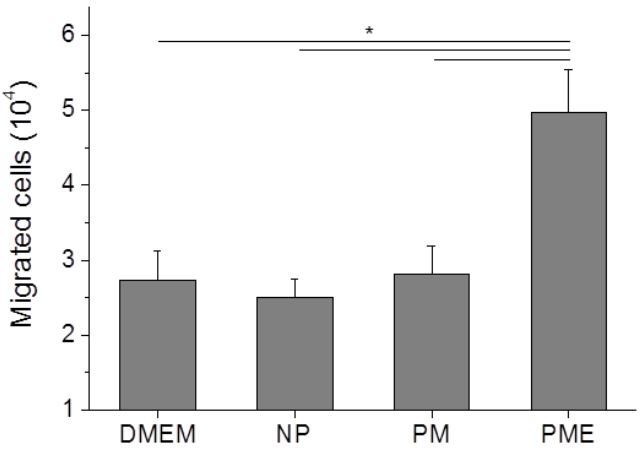


**Figure 5-8.** Migrated cells induced by released products from hydrogels. * Significant differences, $p < 0.05$.

21 d after injection, the capsules of cells remained around the injection sites for all three groups and presented no significant changes in terms of thickness or cell density comparing to the capsules at day 3, as shown in **Figure 5-11a**. For the two groups that did not show cell infiltration at day 3, no signs of cell infiltration in the NP group appeared given another 18 days, as opposed to the extensive infiltration towards the core of hydrogels observed in PM groups. Similar to PME group at day 3, the core of PM hydrogels was not occupied by cells at day 21 (**Figure 5-11a)**. On the other hand, the entire injection site of PME group was filled with cells, including the core of the hydrogel. As shown in **Figure 5-11a**, the cells evenly distributed in the injection area, and the density of the infiltrated cells was significantly higher than the density of cells in the hydrogel area of PM group. In addition, comparing to it at day 3, the cell density in

the injection area of PME group at day 21 increased significantly (**Figure 5-11c**). Echoing the cell infiltration results, no extracellular matrix deposition was found at day 21 in the hydrogel injection area of NP group, while a great amount of extracellular matrix was deposited for the PM and PME group, on top of no deposition for PM group and a significantly smaller amount of deposition for PME group at day 3 (**Figure 5-11b**).

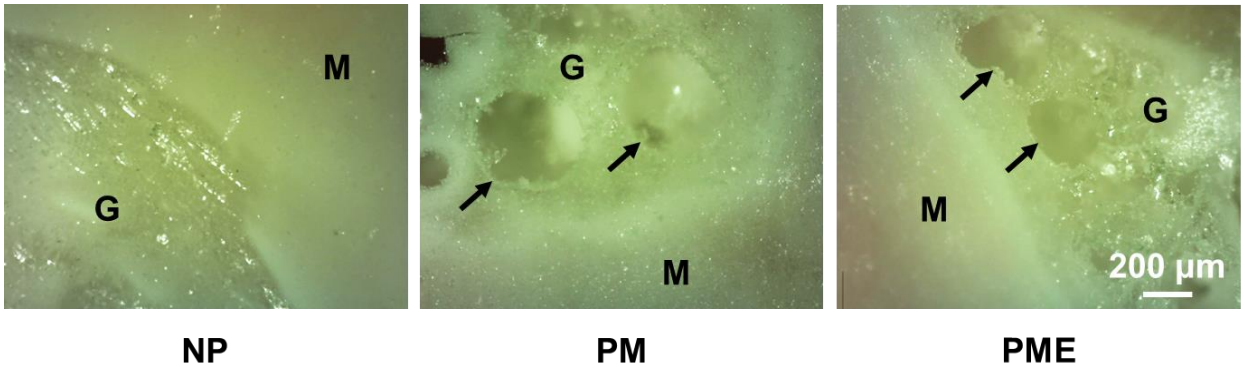


**Figure 5-9.** Porous structure formed in rat hindlimb muscle. M: muscle, G: hydrogel, arrows indicate the capsule.

### 5.3.6 **Macrophage polarization**

Cells around and in the injection area were stained with macrophage markers. CD68 (red)/CD86 (green) and CD68 (red)/CD206 (green) were stained on separate sections. As shown in **Figure 5-12a-d**, $CD68^+$ cells were present in, concentrated in and comprised the major portion of the cell population in the capsule around the injection areas for all three groups at day 3. Colocalization of the red fluorescence from CD68 and green fluorescence from CD86 was observed in all three groups, resulted in yellow cells in the capsules (**Figure 5-12a,c**). The $CD68^+/CD86^+$ subgroups of macrophages ($CD68^+$ cells) were evenly distributed in the capsules without preference on

neither the hydrogel side nor the muscle side. Quantitative results given by CellProfiler showed that around 60% of the macrophages were CD68 positive for all three groups at day 3 (**Figure 5-12e**). $CD68^+/CD206^+$ subgroups of macrophages were also identified in the capsules (**Figure 5-12b,d**). Similar to the $CD68^+$ macrophages, $CD206^+$ macrophages distributed evenly in the capsules. 35%, 40% and 55% of the macrophages were CD206 positive for NP, PM, and PME groups, respectively (**Figure 5-12f**). However, no significant differences among the $CD206^+$

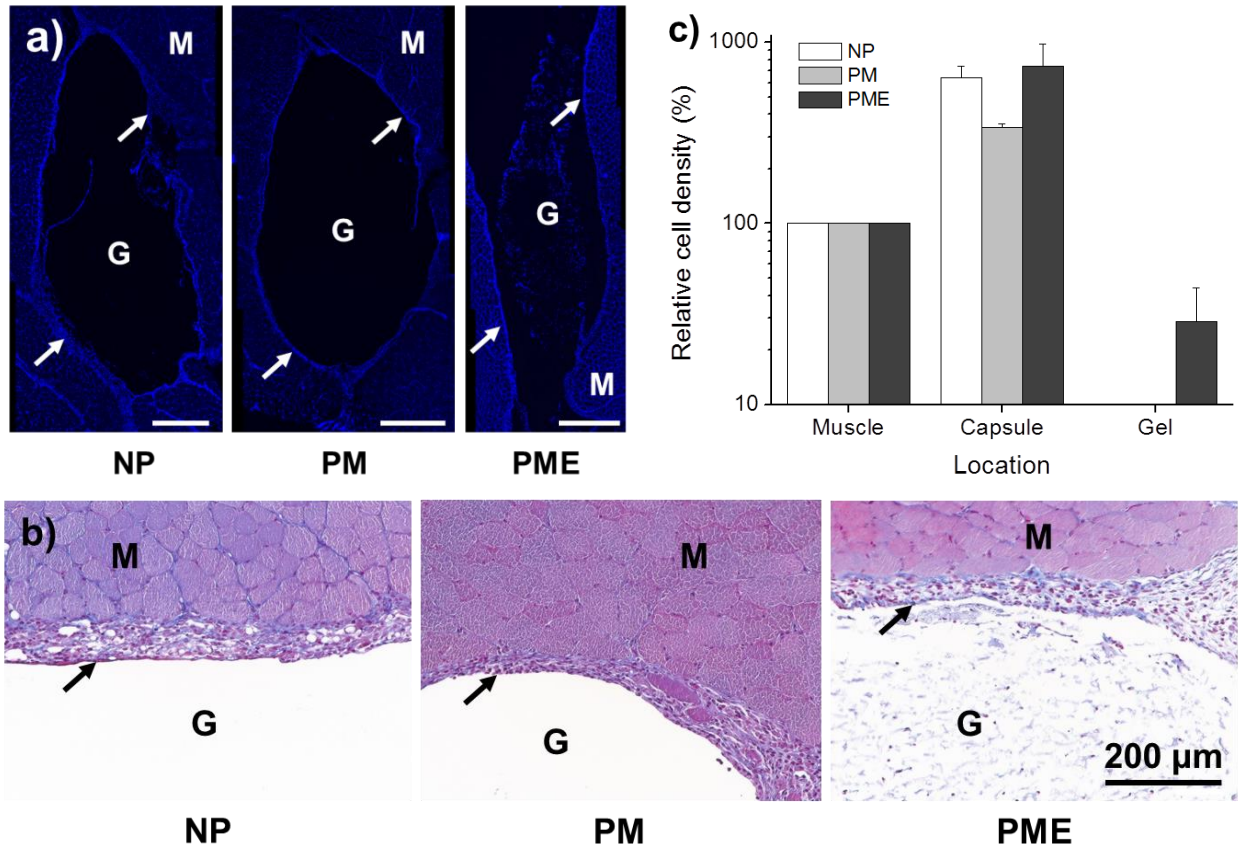


**Figure 5-10.** Cell infiltration 3 d after hydrogel injection. (a) DAPI staining of infiltrated cells and cells encompassing the cells. Scale bar = 500 μm. (b) Masson's trichrome staining of infiltrated cells and cells encompassing the cells. (c) Quantification of cells infiltrated the hydrogels and cells in the capsules. M: muscle, G: hydrogel, arrows indicate the capsule.

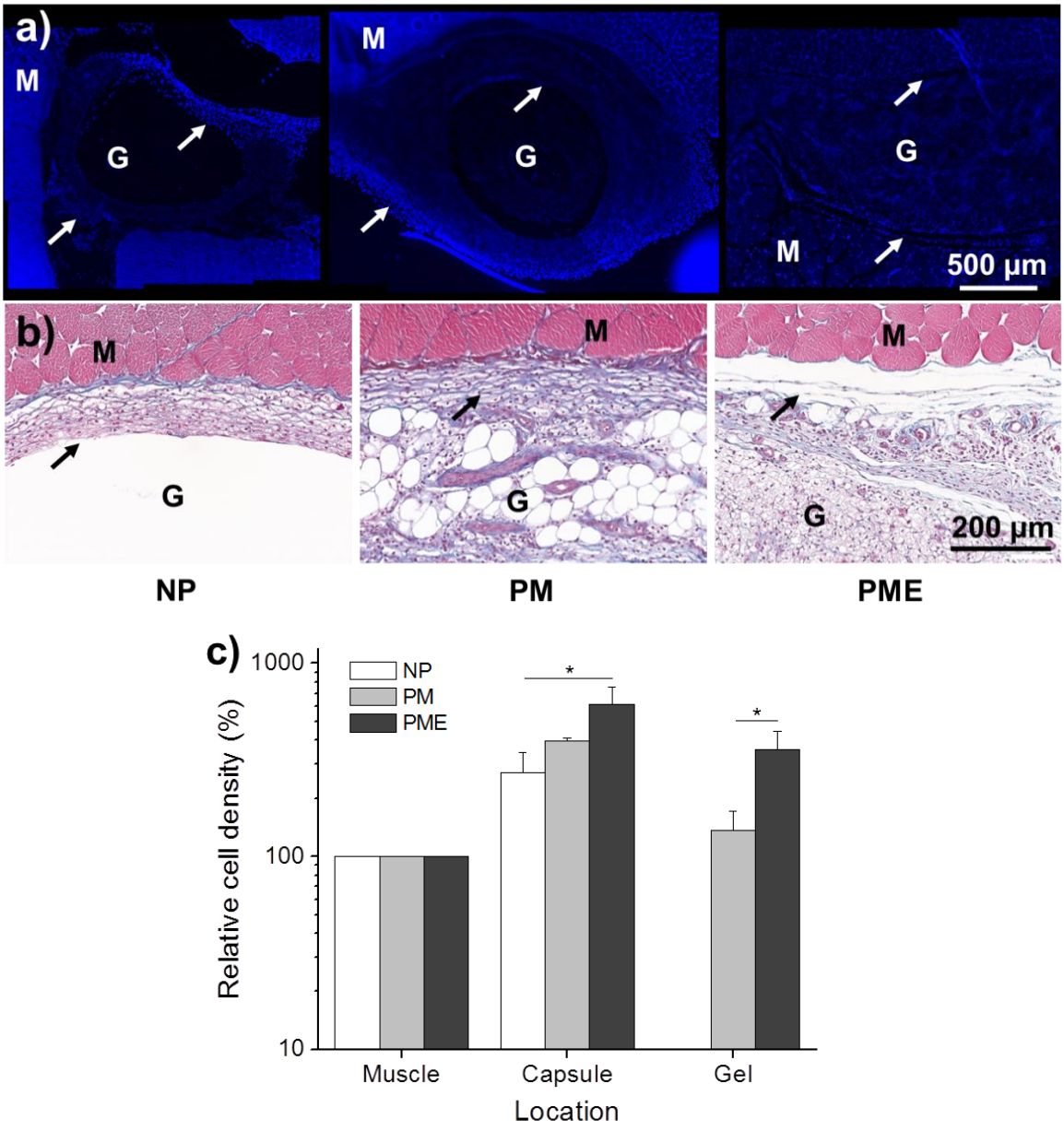


**Figure 5-11.** Cell infiltration 21 d after hydrogel injection. (a) DAPI staining of infiltrated cells and cells encompassing the cells. (b) Masson's trichrome staining of infiltrated cells and cells encompassing the cells. (c) Quantification of cells infiltrated the hydrogels and cells in the capsules. M: muscle, G: hydrogel, arrows indicate the capsule.

percentages were identified. Further calculation showed that the ratio between $CD206^+$ macrophages and $CD68^+$ macrophages for NP group (57%) was smaller than the PME (90%)

group (**Figure 5-12g**), showing that the macrophages in the capsules around injected NP hydrogel was polarized more toward M1 phenotype comparing to PME group. No significant difference was found between NP group and PM group, or between PM group and PME group. Since no cells were found infiltrated the hydrogels of NP and PM groups at day 3, only the macrophage polarization of the cell population in the PME group injection area was analyzed. Comparing to macrophages in the capsule, macrophages infiltrated the PME hydrogel was less activated, as both the $CD68^+$ and $CD206^+$ percentages were smaller (**Figure 5-12e,f**). However, the ratio between $CD206^+$ macrophages and $CD68^+$ macrophages was not significantly different from the ration of the macrophages in the capsule (**Figure 5-12g**).

At day 21, the foreign body response did not diminish, macrophages remained around and in the injection sites, as shown in **Figure 5-13a,b**. CD68 staining showed that the cells infiltrated the PM hydrogel and the cells followed the first wave of infiltrated cells in the PME hydrogel were mostly macrophages (**Figure 5-13a,b**). Similar to the results at day 3, colocalization of CD68 and CD86 was observed for a significant portion of the macrophages in the capsules for all three groups (**Figure 5-13a,c**). The percentage of $CD86^+$ macrophages decreased significantly between day 3 (61%) and day 21(53%) for the PME group, while the percentages did not change significantly for NP and PM groups (**Figure 5-13e**). In terms of $CD206^+$ subgroup of macrophages in the capsules, the percentages decreased significantly between day 3 (40% and 55%) and day 21 (17% and 43%) for PM and PME groups, while no significant change in the percentage of the NP group was found (**Figure 5-13f**). From day 3 to day 21, the ratio between $CD206^+$ macrophages and $CD68^+$ macrophages in the capsules for PM group decreased significantly, while the ratios of NP an PME groups remained at the same level (**Figure 5-13f**).

the

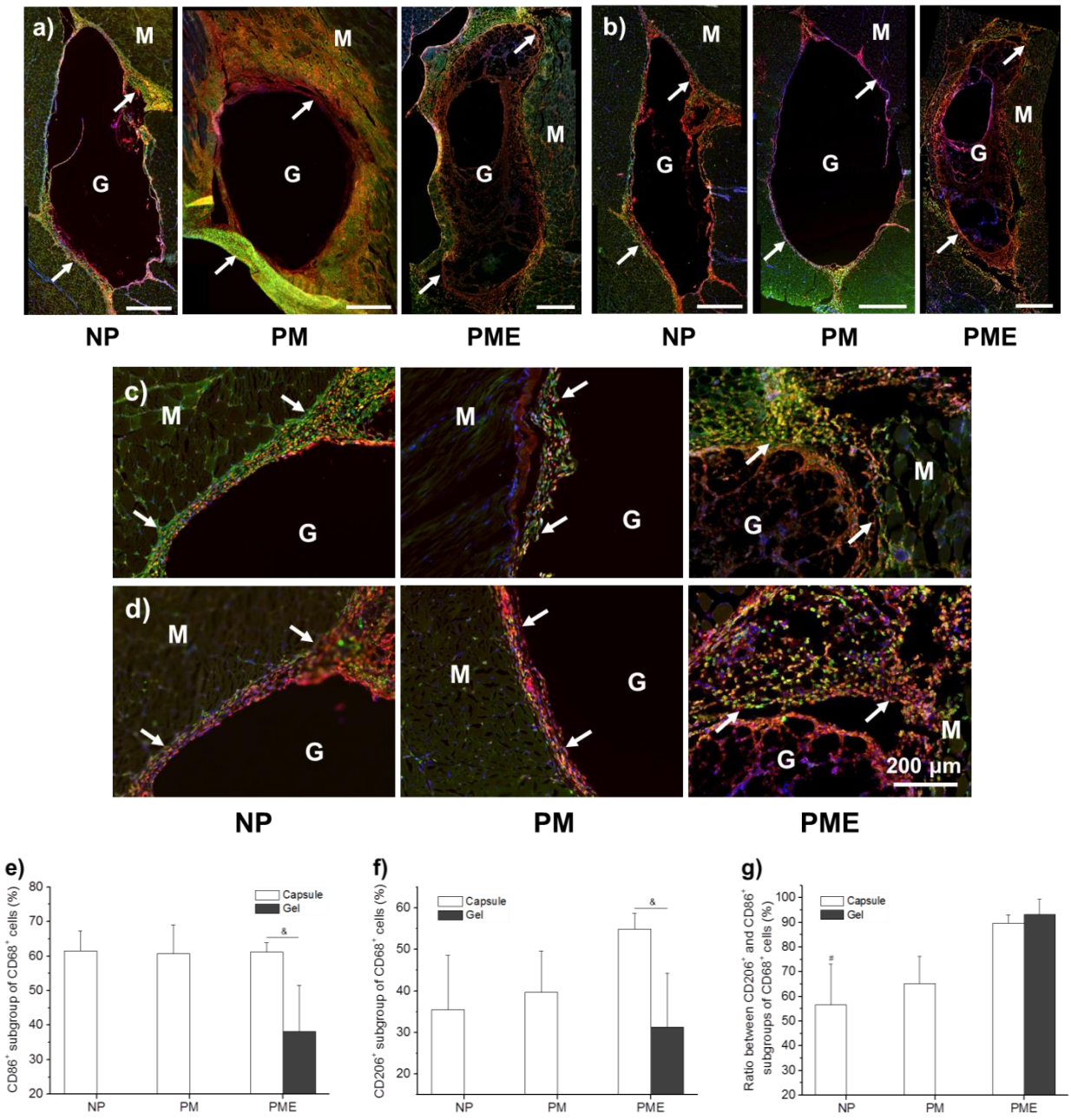


**Figure 5-12.** Macrophage polarization of cells infiltrated the hydrogels and cells in the capsules 3 d after rinjection. (a,c) Pro-M1 macrophage staining. Red: CD68, Green: CD86, Blue: DAPI. (b,d) Pro-M1 macrophage staining. Red: CD68, Green: CD206, Blue: DAPI. (e) Quantification of $CD86^+$ ratio of $CD68^+$ cells infiltrated the hydrogels and cells in the capsules. (f) Quantification of $CD206^+$ ratio of $CD68^+$ cells infiltrated the hydrogels and cells in the capsules. (g) Ratio between pro-M2 and pro-M1 macrophages. M: muscle, G: hydrogel, arrows indicate the capsule. Scale bar in (a,b) = 500 μm.

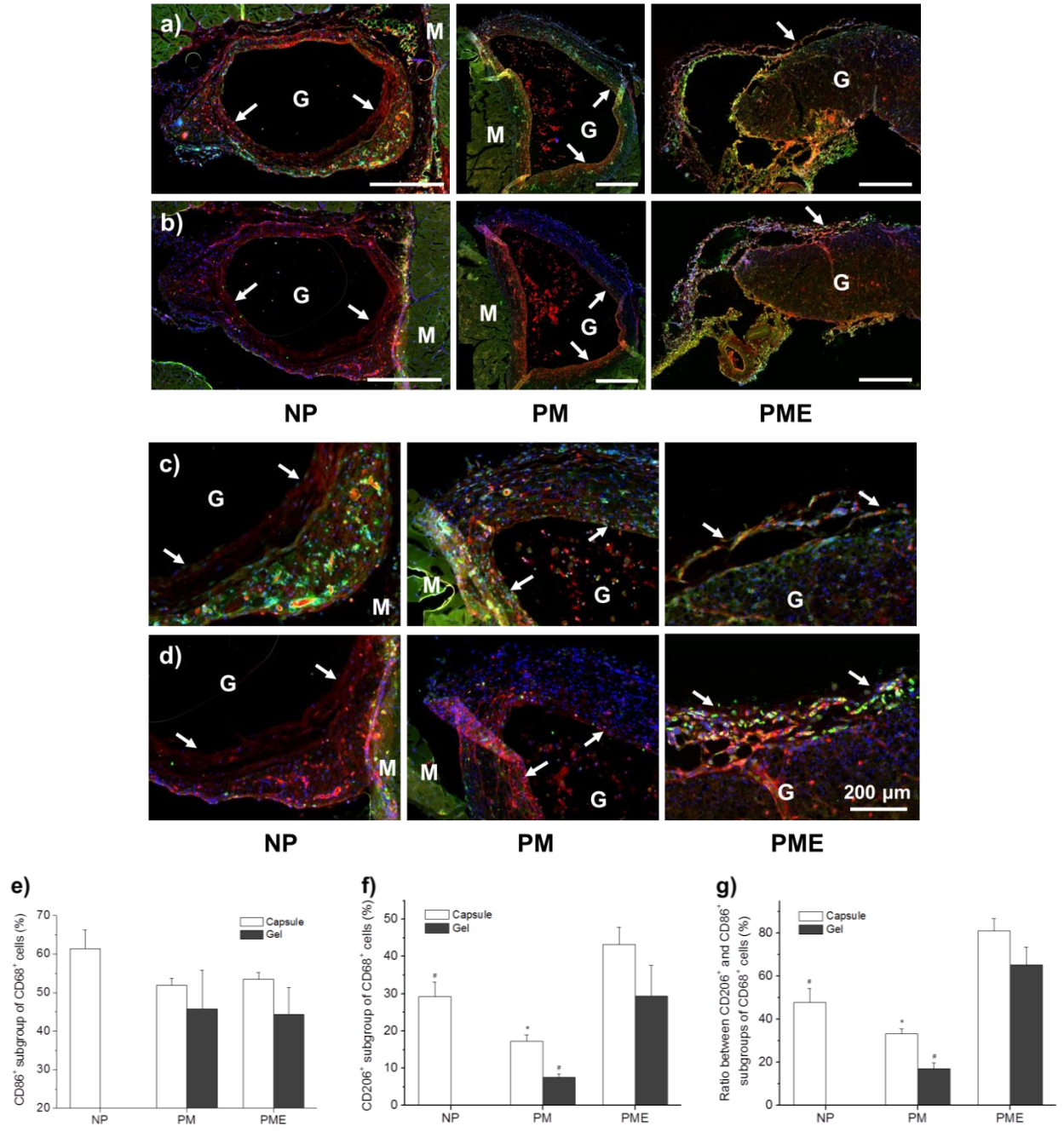


**Figure 5-13.** Macrophage polarization of cells infiltrated the hydrogels and cells in the capsules 21 d after injection. (a,c) Pro-M1 macrophage staining. Red: CD68, Green: CD86, Blue: DAPI. (b,d) Pro-M1 macrophage staining. Red: CD68, Green: CD206, Blue: DAPI. (e) Quantification of $CD86^+$ ratio of $CD68^+$ cells infiltrated the hydrogels and cells in the capsules. (f) Quantification of $CD206^+$ ratio of $CD68^+$ cells infiltrated the hydrogels and cells in the capsules. (g) Ratio between pro-M2 and pro-M1 macrophages. M: muscle, G: hydrogel, arrows indicate the capsule. Scale bar in (a,b) = 500 μm.

As a result, the PM group showed the highest $CD206^+/CD86^+$ ratio among the three groups, and the ratio of NP group is higher than it of the PM group. Therefore, the macrophages in capsules around the injected hydrogel were less activated in PM and PME groups 21 d after injection, and the macrophages in the PME group showed a higher inclination toward M2 polarization. On the other hand, macrophages infiltrated the PM hydrogel after 21 d as previously mentioned. In terms of the $CD206^+/CD86^+$ ratio, the macrophages infiltrated the PM hydrogel polarized more toward the M1 phenotype compared to the macrophages in the capsule around the PM hydrogel and the macrophages infiltrated the PME hydrogel (**Figure 5-13g)**. In contrast, the $CD206^+/CD86^+$ ratios of macrophages in the PME hydrogel did not change between day 3 and day 21.

## 5.4 DISCUSSION

As mentioned above, porous structure in injectable hydrogels could encourage cell infiltration and tissue integration, similar to the widely proven function in other porous scaffolds [211-213]. Recent developments have enabled formation of porous structures in situ in injected hydrogels [192, 214, 215]. However, current strategies are not widely applicable to a broader spectrum of injectable hydrogels. Sacrificial porogen leaching is extensively adopted in fabricating porous scaffolds with control over pore size, porosity and connectivity [216-219]. In principle, porogen leaching is compatible with various gelation mechanisms and material candidates to obtain corresponding combinations for injectable porous hydrogels. The key is the coordination of delivery time, gelation time and dissolution time of porogens. In this study, mannitol was chosen not only for its biocompatibility, but also its characteristics in solubility. Mannitol is highly

soluble in PBS (body fluid) at body temperature, while its solubility is relative low at 4 $^{o}$C. This feature is opposite of poly(NIPAAm-co-VP-co-MAPLA) in PBS solution. Attributed to the contrast in solubility, mixture of hydrogel solution and mannitol particles was feasible at 4 $^{o}$C with insignificant decrease in particle size, and rapid dissolution initiated about the same time of the instant phase transition of hydrogel. Highly soluble porogens may dissolve during mixture and injection steps, or during sol-gel transition for hydrogels with relatively slow gelling mechanisms. On the other hand, slightly soluble porogens or porogens with slow dissolving rates may not generate porous structure shortly after gelation for cell infiltration (gelatin microspheres did not dissolve 24 h after gelation of poly(NIPAAm-co-VP-co-MAPLA) hydrogel, data not shown). Therefore, the solubility and dissolving behavior of porogen candidates should meet the requirement to stay stable prior to gel formation. In addition, the porogens should not interfere with the gelation process or the resultant crosslinks.

It was not expected that the pore size was significantly greater than the size of mannitol particles; and channels were formed connecting adjacent pores. Compared to the original design in which the walls between pores were thin to allow channel formation upon degradation, the existing connections formed during mannitol dissolution is theoretically more beneficial or cell infiltration. We hypothesize that there was short range fluctuation in mannitol particle concentration during mixture and gelation steps which resulted in local aggregation of particles by the end of gelation. This lead to larger, more spherical pores compared to the expected. The volume of hydrogel solution between the aggregated particles is small and relatively discrete. As a result, it did not form scaffold like structures within the pores. The channels between pores may be due to particle aggregates contacting each other during hydrogel gelation as similar poly(NIPAAm) based hydrogel has been reported to shrink upon gelation. Although the focus of

this study is to proof the concept of fabricating porous injectable hydrogel (in combination with modulation of foreign body response), it is important to learn the mechanism behind this phenomenon in order to design and control pore structure in future studies.

In addition to promoting cell infiltration, polarization of macrophage towards a remodeling phenotype has been achieved. As mentioned above, recent studies focusing on mitigating foreign body response induced by injectable hydrogels have employed the strategy of "making material invisible" [119, 198]. In this study we selected to actively intervene the important process as an effort to turn a foe to a friend. Latest mechanistic study by Huleihel et al. has identified matrix-bound vesicles (MBVs) as one of the most decisive component in ECM products in terms of the corresponding bioactivities [209]. Therefore, the introduced simple strategy is theoretically widely applicable to other injectable hydrogel materials, as has been presented in other types of biomaterials and devices [220-222].

Beside the successfully achieved function, several influential factors and accompanying effects need to be discussed. UBM product promoted cell infiltration thus increased the number of macrophages in and around the hydrogel. Although the overall pro-M2 polarization effect has been demonstrated, it is worth noting that the population of M1-like macrophages enlarged as well. Attentions need to be paid on evaluation of such effect base on specific applications. Secondly, with the UBM gel, endotoxin originated from the tissue source was added to the hydrogel composite, too. As endotoxins has been shown to induce pro-M1 polarization of macrophages and it is impossible to completely remove them from ECM product (although endotoxin-tolerance effect may act as a counteractive force), quality control which limits the concentration of endotoxin at a low level is critical [223-225].

In addition to ECM component, there are several other material properties of the composite hydrogel that have potential influence on cell infiltration and macrophage polarization. Pore size (curvature) has been shown to affect macrophage polarization in polyester scaffolds, indicating there may be a favorable range of pore size [117]. The diameter of mannitol particles was originally chosen according to the pro-M2 pore size reported in previous studies. As the concept of modulating macrophage polarization has been proved, in this study we did not attempt to optimize the pore size while the pores were bigger than expected. Hydrogel compressive modulus has also been affected by mixed ECM. Blakney et al. studied activation of macrophages on poly(ethylene glycol)-based hydrogels with compressive moduli of 130, 240 and 840 kPa and found that hydrogels with lower stiffness led to reduced macrophage activation [226]. Since PME gel is porous, the compression modulus of the hydrogel substrate is higher than the composite. Comparing the stiffness of the PM and PME gels, the compression modulus of substrate in PME gel is estimated between 200 and 250 kPa. Therefore, the effect of pro-M2 macrophage polarization may be further improved by optimizing the stiffness of hydrogel substrate. Last but not least, degradation of hydrogel was accelerated with additive ECM component. Current data does not support comprehensive elaboration of its influence on cell infiltration and macrophage polarization, which require input from future studies in order to make the concept introduced in this study more transferrable.

## 5.5 CONCLUSION

In this study, faster cell infiltration and more constructive foreign body response was achieved as an effort to develop platform strategies for improving the biocompatibility and therapeutic

functions for injectable hydrogels. As an example of fast eroding porogens that is compatible with hydrogel gelation mechanism, mannitol microparticles generated connective porous structures shortly after gelation of poly(NIPAAm-co-VP-co-MAPLA) hydrogel. Cell infiltration into the porous gel was significantly accelerated. Decellularized UBM digest was mixed with the porous hydrogel, which lead to pro-M2 macrophage polarization. The PME hydrogel is expected to preserve cardiac function better than its nonporous, less bioactive polyNIPAAm-based counterparts. The material design strategies are believed to have great potential to be translated into other injectable hydrogel systems and corresponding tissue engineering and regenerative medicine applications.

# 6.0 PERSPECTIVE

Important milestones have been reached for intramyocardial biomaterial injection therapy during the first decade since the introduction of this concept. Particularly in the past five years, forms of this type of therapy have proven compelling enough to justify the initiation of clinical trials. For this type of therapy to become a routine option for MI patients, like coronary artery bypass grafting and stenting, compelling data from future clinical trials is required. Furthermore, for clinical success and widespread adoption, it appears that further progress will need to occur in understanding the mechanisms by which injection therapy may benefit and preserve cardiac function, and improving material design to leverage this knowledge. From a practical application perspective, improvements in material properties, injection strategies, imaging, and modeling all can help to improve the efficacy of the therapy to a point where its clinical potential might be realized.

More readily available, information-rich cardiac imaging strategies should complement the development of biomaterial injection therapy. Such advancements would provide better information to correlate the topography of injectate delivery with the local state of the cardiac tissue, allowing the development of algorithms that optimize injection maps for improved, patient-specific functional outcomes. To realize the potential offered by imaging advancements, better delivery methods that can effectively deliver precise injectate patterns within targeted tissue regions will be essential. As noted above, significant progress is being made in this area,

but much room remains for innovation. In terms of the nature of the injectate, the field continues to offer biomaterials scientists and engineers an intriguing design landscape. The classic trade-offs between bioactive natural materials and highly controllable synthetic materials characterize much of the literature to date. As with many other biomaterial applications, designs that can capture the strengths of each material approach would be desirable. The specific design criteria will remain in flux as mechanistic questions and delivery strategies are explored. The designs of poly(NIPAAm) based thermally responsive injectable hydrogels introduced in this research aimed at different aspects of material properties, which exhibited the advantages in versatility. The modification strategies can be combined to fabricate hydrogels integrated with desired enhanced effects.

Often underestimated in its importance for the adoption of such new interventional approaches is the design of the early clinical trials. This is apparent in the few approaches that have progressed to this stage for biomaterial injection therapy, as investigators and regulators seek to design trials that will provide an appropriate risk/benefit profile, but still apply the therapy in a setting where the benefit is pronounced and readily demonstrated. Often this means application in patients with poorer prognoses, (who may be receiving concurrent gold-standard therapy) and the application of the new therapy in a less aggressive fashion. The clinical trials to date suggest that study design may have failed to provide a scenario that allowed the benefit of biomaterial injection therapy to be clearly demonstrated. This is clearly a statement made from the perspective that biomaterial injection therapy holds promise, but is based on observations that many of the parameters employed to date in the clinic may have been suboptimal. For instance, the injectate volume, achieved injectate pattern, patient selection criteria, and time of

intervention all are subject to criticism based on pre-clinical studies and modeling results. These issues apply to HeartLander assisted minimally invasive hydrogel delivery, too. More safety and efficacy studies are required to determine its capabilities, and more importantly, the limitations of the newly proposed intervention option. Further, clinical trials reported to date have used the relatively bland material, alginate. While attractive from a regulatory perspective, there is a broad array of alternative natural and synthetic materials that would be more attractive from a variety of perspectives. In spite of the early clinical failures in terms of their primary endpoints, it is worth recalling that both the AUGMENT-HF and PRESERVATION-1 trials did demonstrate benefit in secondary endpoints, providing encouragement that these early results will serve as a baseline for future advancement.

In considering the future, this research carried a bias in that it focused exclusively on acellular biomaterial injection strategies, whose main function is to provide mechanical support to the LV wall. This class of materials included functional biomaterials whose bioactive components are innate or are covalently attached to the principal material. Not considered were injectable biomaterials that serve principally as vehicles for the delivery of bioactive factors including pharmaceuticals, growth factors or cells. Interested readers may refer to recent reviews that provide good coverage of biomaterials designed for controlled release and delivery in the heart [12, 118, 119]. Although biomaterial injection therapy has repeatedly demonstrated efficacy in animal models, the primary effect and endpoint across the many studies is the preservation of cardiac function. However, the ultimate goal for MI treatment is to regenerate myocardial tissue and restore the cardiac function to pre-infarct levels. Recent advances in cell-based cardiac therapy have demonstrated some promise that cardiomyocyte populations may be restored in the infarcted LV [120-122]. There is potential to combine the mechanical features

inherent in the materials of this review with the pharmaceutical and biological features developing rapidly as well to create injection strategies capable of additional efficacy, albeit with potential added regulatory burden.

# 7.0 SUMMARY

In this research, new classes of thermally responsive injectable hydrogels were developed for intramyocardial injection treatment. A hydrogel previously shown to be effective, poly(NIPAAm-co-HEMA-co-MAPLA), was modified in order to improve its biocompatibility, injectability using a robotic device, visibility under imaging, and bioactivity. The ultimate goal is to develop injectable hydrogels that could better preserve cardiac function, prevent LV dilation and meet the requirements for guided minimally invasive delivery.

In the first part of the study, we added a fourth monomer, MAA to poly(NIPAAm-co-HEMA-co-MAPLA) as an internal catalyzer for the hydrolytic degradation of MAPLA side chains. Results shown that the proton release by MAA lowered the pH in the poly(NIPAAm-co-HEMA-co-MAPLA-co-MAA) (pNHMMj) hydrogels and in the local environment. The in vitro degradation rate of pNHMMj hydrogels was significantly increased, while the thermal sensitivity and mechanical strength of hydrogels were not influenced. A rat hindlimb muscle injection model demonstrated accelerated degradation of pNHMM2 hydrogel in vivo. However, the in vivo degradation rate was smaller than it in vitro. No stimulation of adverse responses to injected acidic hydrogels was observed.

Secondly, a more hydrophilic version of thermally responsive hydrogel was designed to solve the occlusion issue of poly(NIPAAm-co-HEMA-co-MAPLA) hydrogels in the lumen of HeartLander, a robotic injection device for minimally invasive delivery. HEMA component was

replaced by a more hydrophilic monomer, VP, deriving poly(NIPAAm-co-VP-co-MAPLA) copolymers. The specific version of poly(NIPAAm-co-VP-co-MAPLA) with feed ratio of NIPAAm:VP:MAPLA=80:15:5 (VP15) exhibited transition temperature at 26 $^{o}$C. Coupled with the new cooling feature of HeartLander, VP15 hydrogel presented significantly improved injectability with lower viscosity and free of occlusion issue in an ex vivo injection trial. Guided injections of VP15 were successfully made transepicardially on a beating porcine heart through a suxiphoid incision using HeartLander. The pattern of injection sites was confirmed to overlap with designed pattern with minimal error.

As an effort to incorporate bioactivity into the thermally responsive hydrogels whose main function is to provide mechanical support, a ROS scavenger, 4-amino-TEMPO was added to VP15, deriving poly(NIPAAm-co-VP-co-MAPLA-co-MATEMPO) (pNVMT) hydrogel. pNVMT showed high ROS scavenging efficiency as evaluated by ROS generating chamical reactions. pNVMT also protected cells from $H_2O_2$ oxidative stress. In a rat infarction/reperfusion model, pNVMT mitigated cell damage under oxidative stress, protected cell metabolic function, and reduced cell apoptosis. The antioxidant effect of pNVMT was greater than free TEMPO, which was attributed to the extended retention of TEMPO in the myocardium by covalent attachment to pNVMT. On the other hand, TEMPO enabled imaging of pNVMT hydrogel in vivo with MRI.

In the last part of our research, a porous, bioactive hydrogel was fabricated to promote cell infiltration and modulate foreign body response to a more remodeling fashion. Employing "porogen leaching" strategy, connective porous structure were formed shortly after hydrogel (poly(NIPAAm-co-VP-co-MAPLA), VP10) injection. These pores and channels facilitated faster cell infiltration compared to nonporous control. On the other hand, decellularized tissue product

(UBM digest) was mixed into VP10 hydrogel, which promoted pro-M2 polarization of macrophages in and around the injected hydrogel. The modulation effect lasted for the entire observation period (21 d). In addition, UBM digest also accelerated hydrogel degradation and cell infiltration, superimposing the effect of porous structure.

In summary, aiming at better meeting the specific requirements for hydrogel candidates for intramyocardial injection treatment, the poly(NIPAAm-co-HEMA-co-MAPLA) hydrogel was modified at different aspects. These modifications have been proven effective. In addition, the chemistry and strategies used in each modification were mutually orthogonal. The hydrogels described in this work and potential designs combining the advantages of individual modification would potentially further improve the performance of thermally responsive injectable hydrogels for MI treatment.

## BIBLIOGRAPHY


[1] WHO, Global status report on noncommunicable diseases 2014, World Health Organization, Geneva, 2014.

[2] J. Xu, S.L. Murphy, K.D. Kochanek, B.A. Bastian, Deaths: Final Data for 2013, Natl. Vital Stat. Rep. (2016) 1-119.

[3] K.L. Christman, H.H. Fok, R.E. Sievers, Q. Fang, R.J. Lee, Fibrin glue alone and skeletal myoblasts in a fibrin scaffold preserve cardiac function after myocardial infarction, Tissue Eng. (2004) 403-409.

[4] K.L. Christman, A.J. Vardanian, Q. Fang, R.E. Sievers, H.H. Fok, R.J. Lee, Injectable fibrin scaffold improves cell transplant survival, reduces infarct expansion, and induces neovasculature formation in ischemic myocardium, J. Am. Coll. Cardiol. (2004) 654-660.

[5] S.T. Wall, J.C. Walker, K.E. Healy, M.B. Ratcliffe, J.M. Guccione, Theoretical impact of the injection of material into the myocardium: a finite element model simulation, Circulation. (2006) 2627-2635.

[6] E. Tous, B. Purcell, J. Ifkovits, J. Burdick, Injectable Acellular Hydrogels for Cardiac Repair, J. Cardiovasc. Transl. Res. (2011) 528-542.

[7] A.A. Rane, K.L. Christman, Biomaterials for the treatment of myocardial infarction: a 5-year update, J. Am. Coll. Cardiol. (2011) 2615-2629.

[8] D.M. Nelson, Z. Ma, K.L. Fujimoto, R. Hashizume, W.R. Wagner, Intra-myocardial biomaterial injection therapy in the treatment of heart failure: Materials, outcomes and challenges, Acta Biomater. (2011) 1-15.

[9] L. BioLineRx, Safety and Feasibility of the Injectable BL-1040 Implant. https://clinicaltrials.gov/ct2/show/NCT00557531, 2009 (accessed 2016.11.15).

[10] J. Leor, S. Tuvia, V. Guetta, F. Manczur, D. Castel, U. Willenz, O. Petnehazy, N. Landa, M.S. Feinberg, E. Konen, O. Goitein, O. Tsur-Gang, M. Shaul, L. Klapper, S. Cohen, Intracoronary injection of in situ forming alginate hydrogel reverses left ventricular remodeling after myocardial infarction in Swine, J. Am. Coll. Cardiol. (2009) 1014-1023.

[11] N. Frey, A. Linke, T. Suselbeck, J. Muller-Ehmsen, P. Vermeersch, D. Schoors, M. Rosenberg, F. Bea, S. Tuvia, J. Leor, Intracoronary delivery of injectable bioabsorbable

scaffold (IK-5001) to treat left ventricular remodeling after ST-elevation myocardial infarction: a first-in-man study, Circ. Cardiovasc. Interv. (2014) 806-812.

[12] H.S. O'Neill, L.B. Gallagher, J. O'Sullivan, W. Whyte, C. Curley, E. Dolan, A. Hameed, J. O'Dwyer, C. Payne, D. O'Reilly, E. Ruiz-Hernandez, E.T. Roche, F.J. O'Brien, S.A. Cryan, H. Kelly, B. Murphy, G.P. Duffy, Biomaterial-Enhanced Cell and Drug Delivery: Lessons Learned in the Cardiac Field and Future Perspectives, Adv. Mater. (2016) 5648-5661.

[13] B.B. LLC, IK-5001 for the Prevention of Remodeling of the Ventricle and Congestive Heart Failure After Acute Myocardial Infarction (PRESERVATION 1). https://clinicaltrials.gov/ct2/show/NCT01226563, 2010 (accessed 2016.11.30).

[14] S.V. Rao, U. Zeymer, P.S. Douglas, H. Al-Khalidi, J. Liu, C.M. Gibson, R.W. Harrison, D.S. Joseph, R. Heyrman, M.W. Krucoff, A randomized, double-blind, placebo-controlled trial to evaluate the safety and effectiveness of intracoronary application of a novel bioabsorbable cardiac matrix for the prevention of ventricular remodeling after large ST-segment elevation myocardial infarction: Rationale and design of the PRESERVATION I trial, Am. Heart J. (2015) 929-937.

[15] U. Zeymer, S.V. Rao, M.W. Krucoff, A placebo-controlled, multicenter, randomized, doubleblind trial to evaluate the safety and effectiveness of IK-5001 (Bioabsorbable Cardiac Matrix [BCM]) for the prevention of remodeling of the ventricle and congestive heart failure after acute myocardial infarction. https://www.escardio.org/static_file/Escardio/Press-media/Press%20releases/2015/Congress/PRESERVATION_Zeymer.pdf, 2015 (accessed 2016.10.30).

[16] H.N. Sabbah, M. Wang, A. Jiang, I. Ilsar, M.S. Sabbah, S. Helgerson, R. Peterson, N. Tarazona, R. Lee, Abstract 4050: Circumferential Mid-Ventricular Intramyocardial Injections of Alginate Hydrogel Improve Left Ventricular Function and Prevent Progressive Remodeling in Dogs With Chronic Heart Failure, Circulation. (2016) S912-S912.

[17] H.N. Sabbah, M. Wang, R.C. Gupta, S. Rastogi, I. Ilsar, M.S. Sabbah, S. Kohli, S. Helgerson, R.J. Lee, Augmentation of Left Ventricular Wall Thickness With Alginate Hydrogel Implants Improves Left Ventricular Function and Prevents Progressive Remodeling in Dogs With Chronic Heart Failure, JACC Heart Fail. (2013) 252-258.

[18] R.J. Lee, A. Hinson, S. Helgerson, R. Bauernschmitt, H.N. Sabbah, Polymer-based restoration of left ventricular mechanics, Cell Transplant. (2013) 529-533.

[19] L.H. Inc., A Randomized, Controlled Study to Evaluate Algisyl-LVR™ as a Method of Left Ventricular Augmentation for Heart Failure (AUGMENT-HF). https://clinicaltrials.gov/ct2/show/NCT00847964, 2009 (accessed 2016.12.05).

[20] L.C. Lee, Z. Zhihong, A. Hinson, J.M. Guccione, Reduction in left ventricular wall stress and improvement in function in failing hearts using Algisyl-LVR, J Vis Exp. (2013).

[21] L.C. Lee, S.T. Wall, D. Klepach, L. Ge, Z. Zhang, R.J. Lee, A. Hinson, J.H. Gorman, 3rd, R.C. Gorman, J.M. Guccione, Algisyl-LVR with coronary artery bypass grafting reduces left ventricular wall stress and improves function in the failing human heart, Int. J. Cardiol. (2013) 2022-2028.

[22] D.L. Mann, R.J. Lee, A.J. Coats, G. Neagoe, D. Dragomir, E. Pusineri, M. Piredda, L. Bettari, B.A. Kirwan, R. Dowling, M. Volterrani, S.D. Solomon, H.N. Sabbah, A. Hinson, S.D. Anker, One-year follow-up results from AUGMENT-HF: a multicentre randomized controlled clinical trial of the efficacy of left ventricular augmentation with Algisyl in the treatment of heart failure, Eur. J. Heart Fail. (2016) 314-325.

[23] J.M. Singelyn, J.A. DeQuach, S.B. Seif-Naraghi, R.B. Littlefield, P.J. Schup-Magoffin, K.L. Christman, Naturally derived myocardial matrix as an injectable scaffold for cardiac tissue engineering, Biomaterials. (2009) 5409-5416.

[24] I. Ventrix, A Study of VentriGel in Early and Late Post-myocardial Infarction Patients. https://clinicaltrials.gov/ct2/show/NCT02305602, 2014 (accessed 2016.11.08).

[25] S.B. Seif-Naraghi, M.A. Salvatore, P.J. Schup-Magoffin, D.P. Hu, K.L. Christman, Design and characterization of an injectable pericardial matrix gel: a potentially autologous scaffold for cardiac tissue engineering, Tissue Eng. Part A. (2010) 2017-2027.

[26] S.F. Badylak, D.O. Freytes, T.W. Gilbert, Extracellular matrix as a biological scaffold material: Structure and function, Acta Biomater. (2009) 1-13.

[27] S.F. Badylak, D.O. Freytes, T.W. Gilbert, Reprint of: Extracellular matrix as a biological scaffold material: Structure and function, Acta Biomater. (2015) S17-26.

[28] F.W. Meng, P.F. Slivka, C.L. Dearth, S.F. Badylak, Solubilized extracellular matrix from brain and urinary bladder elicits distinct functional and phenotypic responses in macrophages, Biomaterials. (2015) 131-140.

[29] J.M. Singelyn, P. Sundaramurthy, T.D. Johnson, P.J. Schup-Magoffin, D.P. Hu, D.M. Faulk, J. Wang, K.M. Mayle, K. Bartels, M. Salvatore, A.M. Kinsey, A.N. DeMaria, N. Dib, K.L. Christman, Catheter-Deliverable Hydrogel Derived From Decellularized Ventricular Extracellular Matrix Increases Endogenous Cardiomyocytes and Preserves Cardiac Function Post-Myocardial Infarction, J. Am. Coll. Cardiol. (2012) 751-763.

[30] S.B. Seif-Naraghi, J.M. Singelyn, M.A. Salvatore, K.G. Osborn, J.J. Wang, U. Sampat, O.L. Kwan, G.M. Strachan, J. Wong, P.J. Schup-Magoffin, R.L. Braden, K. Bartels, J.A. DeQuach, M. Preul, A.M. Kinsey, A.N. DeMaria, N. Dib, K.L. Christman, Safety and efficacy of an injectable extracellular matrix hydrogel for treating myocardial infarction, Sci. Transl. Med. (2013) 173ra125.

[31] T.D. Vu, S.N. Pal, L.K. Ti, E.C. Martinez, A.J. Rufaihah, L.H. Ling, C.N. Lee, A.M. Richards, T. Kofidis, An autologous platelet-rich plasma hydrogel compound restores left ventricular structure, function and ameliorates adverse remodeling in a minimally invasive

large animal myocardial restoration model: a translational approach: Vu and Pal "Myocardial Repair: PRP, Hydrogel and Supplements", Biomaterials. (2015) 27-35.

[32] S.R. Eckhouse, B.P. Purcell, J.R. McGarvey, D. Lobb, C.B. Logdon, H. Doviak, J.W. O'Neill, J.A. Shuman, C.P. Novack, K.N. Zellars, S. Pettaway, R.A. Black, A. Khakoo, T. Lee, R. Mukherjee, J.H. Gorman, R.C. Gorman, J.A. Burdick, F.G. Spinale, Local hydrogel release of recombinant TIMP-3 attenuates adverse left ventricular remodeling after experimental myocardial infarction, Sci. Transl. Med. (2014) 223ra221.

[33] S.M. Dorsey, J.R. McGarvey, H. Wang, A. Nikou, L. Arama, K.J. Koomalsingh, N. Kondo, J.H. Gorman, 3rd, J.J. Pilla, R.C. Gorman, J.F. Wenk, J.A. Burdick, MRI evaluation of injectable hyaluronic acid-based hydrogel therapy to limit ventricular remodeling after myocardial infarction, Biomaterials. (2015) 65-75.

[34] E. Tous, J.L. Ifkovits, K.J. Koomalsingh, T. Shuto, T. Soeda, N. Kondo, J.H. Gorman, 3rd, R.C. Gorman, J.A. Burdick, Influence of injectable hyaluronic acid hydrogel degradation behavior on infarction-induced ventricular remodeling, Biomacromolecules. (2011) 4127-4135.

[35] C.B. Rodell, M.E. Lee, H. Wang, S. Takebayashi, T. Takayama, T. Kawamura, J.S. Arkles, N.N. Dusaj, S.M. Dorsey, W.R. Witschey, J.J. Pilla, J.H. Gorman, 3rd, J.F. Wenk, J.A. Burdick, R.C. Gorman, Injectable Shear-Thinning Hydrogels for Minimally Invasive Delivery to Infarcted Myocardium to Limit Left Ventricular Remodeling, Circ. Cardiovasc. Interv. (2016) 1268-1276.

[36] M. Morita, C.E. Eckert, K. Matsuzaki, M. Noma, L.P. Ryan, J.A. Burdick, B.M. Jackson, J.H. Gorman, 3rd, M.S. Sacks, R.C. Gorman, Modification of infarct material properties limits adverse ventricular remodeling, Ann. Thorac. Surg. (2011) 617-624.

[37] J.R. McGarvey, N. Kondo, W.R. Witschey, M. Takebe, C. Aoki, J.A. Burdick, F.G. Spinale, J.H. Gorman, 3rd, J.J. Pilla, R.C. Gorman, Injectable microsphere gel progressively improves global ventricular function, regional contractile strain, and mitral regurgitation after myocardial infarction, Ann. Thorac. Surg. (2015) 597-603.

[38] J.R. McGarvey, S. Pettaway, J.A. Shuman, C.P. Novack, K.N. Zellars, P.D. Freels, R.L. Echols, Jr., J.A. Burdick, J.H. Gorman, 3rd, R.C. Gorman, F.G. Spinale, Targeted injection of a biocomposite material alters macrophage and fibroblast phenotype and function following myocardial infarction: relation to left ventricular remodeling, J. Pharmacol. Exp. Ther. (2014) 701-709.

[39] J.A. Dixon, R.C. Gorman, R.E. Stroud, R. Mukherjee, E.C. Meyer, N.L. Baker, M. Morita, H. Hamamoto, L.P. Ryan, J.H. Gorman, 3rd, F.G. Spinale, Targeted regional injection of biocomposite microspheres alters post-myocardial infarction remodeling and matrix proteolytic pathways, Circulation. (2011) S35-45.

[40] M.M. Bastings, S. Koudstaal, R.E. Kieltyka, Y. Nakano, A.C. Pape, D.A. Feyen, F.J. van Slochteren, P.A. Doevendans, J.P. Sluijter, E.W. Meijer, S.A. Chamuleau, P.Y. Dankers, A

fast pH-switchable and self-healing supramolecular hydrogel carrier for guided, local catheter injection in the infarcted myocardium, Adv. Healthc. Mater. (2014) 70-78.

[41] Y.D. Lin, M.Y. Chang, B. Cheng, Y.W. Liu, L.C. Lin, J.H. Chen, P.C. Hsieh, Injection of Peptide nanogels preserves postinfarct diastolic function and prolongs efficacy of cell therapy in pigs, Tissue Eng. Part A. (2015) 1662-1671.

[42] K.G. Soucy, E.F. Smith, G. Monreal, G. Rokosh, B.B. Keller, F. Yuan, R.G. Matheny, A.M. Fallon, B.C. Lewis, L.C. Sherwood, M.A. Sobieski, G.A. Giridharan, S.C. Koenig, M.S. Slaughter, Feasibility study of particulate extracellular matrix (P-ECM) and left ventricular assist device (HVAD) therapy in chronic ischemic heart failure bovine model, ASAIO J. (2015) 161-169.

[43] M.M. Swindle, A. Makin, A.J. Herron, F.J. Clubb, Jr., K.S. Frazier, Swine as models in biomedical research and toxicology testing, Vet. Pathol. (2012) 344-356.

[44] G.S. Kassab, Y.C. Fung, Topology and dimensions of pig coronary capillary network, American Journal of Physiology - Heart and Circulatory Physiology. (1994) H319-H325.

[45] K.R. Bainey, P.W. Armstrong, Ameliorating reperfusion injury in STEMI: dead or alive?, Eur. Heart J. (2014) 2504-2506.

[46] N.K. Kapur, V. Paruchuri, J.A. Urbano-Morales, E.E. Mackey, G.H. Daly, X. Qiao, N. Pandian, G. Perides, R.H. Karas, Mechanically unloading the left ventricle before coronary reperfusion reduces left ventricular wall stress and myocardial infarct size, Circulation. (2013) 328-336.

[47] C.B. Fordyce, B.J. Gersh, G.W. Stone, C.B. Granger, Novel therapeutics in myocardial infarction: targeting microvascular dysfunction and reperfusion injury, Trends Pharmacol. Sci. (2015) 605-616.

[48] K.L. Sack, N.H. Davies, J.M. Guccione, T. Franz, Personalised computational cardiology: Patient-specific modelling in cardiac mechanics and biomaterial injection therapies for myocardial infarction, Heart Fail. Rev. (2016).

[49] E.T. Kichula, H. Wang, S.M. Dorsey, S.E. Szczesny, D.M. Elliott, J.A. Burdick, J.F. Wenk, Experimental and computational investigation of altered mechanical properties in myocardium after hydrogel injection, Ann. Biomed. Eng. (2014) 1546-1556.

[50] J.F. Wenk, P. Eslami, Z. Zhang, C. Xu, E. Kuhl, J.H. Gorman Iii, J.D. Robb, M.B. Ratcliffe, R.C. Gorman, J.M. Guccione, A Novel Method for Quantifying the In-Vivo Mechanical Effect of Material Injected Into a Myocardial Infarction, Ann. Thorac. Surg. (2011) 935-941.

[51] N. Toussaint, C.T. Stoeck, T. Schaeffter, S. Kozerke, M. Sermesant, P.G. Batchelor, In vivo human cardiac fibre architecture estimation using shape-based diffusion tensor processing, Med. Image Anal. (2013) 1243-1255.

[52] L.C. Lee, S.T. Wall, M. Genet, A. Hinson, J.M. Guccione, Bioinjection treatment: effects of post-injection residual stress on left ventricular wall stress, J. Biomech. (2014) 3115-3119.

[53] J. Kortsmit, N.H. Davies, R. Miller, P. Zilla, T. Franz, Computational predictions of improved of wall mechanics and function of the infarcted left ventricle at early and late remodelling stages, Adv. Biomech. Appl. (2013) 41-55.

[54] R. Miller, N.H. Davies, J. Kortsmit, P. Zilla, T. Franz, Outcomes of myocardial infarction hydrogel injection therapy in the human left ventricle dependent on injectate distribution, Int. J. Numer. Method. Biomed. Eng. (2013) 870-884.

[55] K. Kadner, S. Dobner, T. Franz, D. Bezuidenhout, M.S. Sirry, P. Zilla, N.H. Davies, The beneficial effects of deferred delivery on the efficiency of hydrogel therapy post myocardial infarction, Biomaterials. (2012) 2060-2066.

[56] P.A. Cain, R. Ahl, E. Hedstrom, M. Ugander, A. Allansdotter-Johnsson, P. Friberg, H. Arheden, Age and gender specific normal values of left ventricular mass, volume and function for gradient echo magnetic resonance imaging: a cross sectional study, BMC Med. Imaging. (2009) 2.

[57] M. Foppa, B.B. Duncan, L.E. Rohde, Echocardiography-based left ventricular mass estimation. How should we define hypertrophy?, Cardiovasc. Ultrasound. (2005) 17.

[58] P. Wise, N.H. Davies, M.S. Sirry, J. Kortsmit, L. Dubuis, C.K. Chai, F.P. Baaijens, T. Franz, Excessive volume of hydrogel injectates may compromise the efficacy for the treatment of acute myocardial infarction, Int. J. Numer. Method. Biomed. Eng. (2016).

[59] B.I. Jugdutt, N.S. Dhalla, Cardiac Remodeling: Molecular Mechanisms, Springer, New York, 2013.

[60] N. Landa, L. Miller, M.S. Feinberg, R. Holbova, M. Shachar, I. Freeman, S. Cohen, J. Leor, Effect of injectable alginate implant on cardiac remodeling and function after recent and old infarcts in rat, Circulation. (2008) 1388-1396.

[61] T. Yoshizumi, Y. Zhu, H. Jiang, A. D'Amore, H. Sakaguchi, J. Tchao, K. Tobita, W.R. Wagner, Timing effect of intramyocardial hydrogel injection for positively impacting left ventricular remodeling after myocardial infarction, Biomaterials. (2016) 182-193.

[62] K.L. Fujimoto, Z. Ma, D.M. Nelson, R. Hashizume, J. Guan, K. Tobita, W.R. Wagner, Synthesis, characterization and therapeutic efficacy of a biodegradable, thermoresponsive hydrogel designed for application in chronic infarcted myocardium, Biomaterials. (2009) 4357-4368.

[63] S.J. Yoon, Y.H. Fang, C.H. Lim, B.S. Kim, H.S. Son, Y. Park, K. Sun, Regeneration of ischemic heart using hyaluronic acid-based injectable hydrogel, J. Biomed. Mater. Res. B Appl. Biomater. (2009) 163-171.

[64] R. Mukherjee, J.A. Zavadzkas, S.M. Saunders, J.E. McLean, L.B. Jeffords, C. Beck, R.E. Stroud, A.M. Leone, C.N. Koval, W.T. Rivers, S. Basu, A. Sheehy, G. Michal, F.G. Spinale, Targeted myocardial microinjections of a biocomposite material reduces infarct expansion in pigs, Ann. Thorac. Surg. (2008) 1268-1276.

[65] H. Wang, X. Zhang, Y. Li, Y. Ma, Y. Zhang, Z. Liu, J. Zhou, Q. Lin, Y. Wang, C. Duan, C. Wang, Improved myocardial performance in infarcted rat heart by co-injection of basic fibroblast growth factor with temperature-responsive Chitosan hydrogel, J. Heart Lung Transplant. (2010) 881-887.

[66] Z.Q. Zhao, J.D. Puskas, D. Xu, N.P. Wang, M. Mosunjac, R.A. Guyton, J. Vinten-Johansen, R. Matheny, Improvement in cardiac function with small intestine extracellular matrix is associated with recruitment of C-kit cells, myofibroblasts, and macrophages after myocardial infarction, J. Am. Coll. Cardiol. (2010) 1250-1261.

[67] J.W. Wassenaar, R. Gaetani, J.J. Garcia, R.L. Braden, C.G. Luo, D. Huang, A.N. DeMaria, J.H. Omens, K.L. Christman, Evidence for Mechanisms Underlying the Functional Benefits of a Myocardial Matrix Hydrogel for Post-MI Treatment, J. Am. Coll. Cardiol. (2016) 1074-1086.

[68] S.L. Suarez, A.A. Rane, A. Munoz, A.T. Wright, S.X. Zhang, R.L. Braden, A. Almutairi, A.D. McCulloch, K.L. Christman, Intramyocardial injection of hydrogel with high interstitial spread does not impact action potential propagation, Acta Biomater. (2015) 13-22.

[69] Y. Sun, Myocardial repair/remodelling following infarction: roles of local factors, Cardiovasc. Res. (2009) 482-490.

[70] C. Delcayre, J.S. Silvestre, A. Garnier, A. Oubenaissa, S. Cailmail, E. Tatara, B. Swynghedauw, V. Robert, Cardiac aldosterone production and ventricular remodeling, Kidney Int. (2000) 1346-1351.

[71] D.E. Dostal, K.M. Baker, The cardiac renin-angiotensin system: conceptual, or a regulator of cardiac function?, Circ. Res. (1999) 643-650.

[72] J. Tinkel, H. Hassanain, S.J. Khouri, Cardiovascular antioxidant therapy: a review of supplements, pharmacotherapies, and mechanisms, Cardiol. Rev. (2012) 77-83.

[73] M.A. Pfeffer, E. Braunwald, Ventricular remodeling after myocardial infarction. Experimental observations and clinical implications, Circulation. (1990) 1161-1172.

[74] M. Okada, T.R. Payne, H. Oshima, N. Momoi, K. Tobita, J. Huard, Differential efficacy of gels derived from small intestinal submucosa as an injectable biomaterial for myocardial infarct repair, Biomaterials. (2010) 7678-7683.

[75] M.S. Sirry, N.H. Davies, K. Kadner, L. Dubuis, M.G. Saleh, E.M. Meintjes, B.S. Spottiswoode, P. Zilla, T. Franz, Micro-structurally detailed model of a therapeutic

hydrogel injectate in a rat biventricular cardiac geometry for computational simulations, Comput. Methods Biomech. Biomed. Eng. (2015) 325-331.

[76] A.D. Rouillard, J.W. Holmes, Coupled agent-based and finite-element models for predicting scar structure following myocardial infarction, Prog. Biophys. Mol. Biol. (2014) 235-243.

[77] A.A. Rane, J.S. Chuang, A. Shah, D.P. Hu, N.D. Dalton, Y. Gu, K.L. Peterson, J.H. Omens, K.L. Christman, Increased infarct wall thickness by a bio-inert material is insufficient to prevent negative left ventricular remodeling after myocardial infarction, PLoS One. (2011) e21571.

[78] A. Mihic, Z. Cui, J. Wu, G. Vlacic, Y. Miyagi, S.H. Li, S. Lu, H.W. Sung, R.D. Weisel, R.K. Li, A Conductive Polymer Hydrogel Supports Cell Electrical Signaling and Improves Cardiac Function After Implantation into Myocardial Infarct, Circulation. (2015) 772-784.

[79] H. Cui, Y. Liu, Y. Cheng, Z. Zhang, P. Zhang, X. Chen, Y. Wei, In Vitro Study of Electroactive Tetraaniline-Containing Thermosensitive Hydrogels for Cardiac Tissue Engineering, Biomacromolecules. (2014).

[80] P. Baei, S. Jalili-Firoozinezhad, S. Rajabi-Zeleti, M. Tafazzoli-Shadpour, H. Baharvand, N. Aghdami, Electrically conductive gold nanoparticle-chitosan thermosensitive hydrogels for cardiac tissue engineering, Mater. Sci. Eng. C Mater. Biol. Appl. (2016) 131-141.

[81] N. Annabi, S.R. Shin, A. Tamayol, M. Miscuglio, M.A. Bakooshli, A. Assmann, P. Mostafalu, J.Y. Sun, S. Mithieux, L. Cheung, X.S. Tang, A.S. Weiss, A. Khademhosseini, Highly Elastic and Conductive Human-Based Protein Hybrid Hydrogels, Adv. Mater. (2016) 40-49.

[82] L.A. Reis, L.L. Chiu, J. Wu, N. Feric, C. Laschinger, A. Momen, R.K. Li, M. Radisic, Hydrogels with integrin-binding angiopoietin-1-derived peptide, QHREDGS, for treatment of acute myocardial infarction, Circ. Heart Fail. (2015) 333-341.

[83] J. Li, Y. Shu, T. Hao, Y. Wang, Y. Qian, C. Duan, H. Sun, Q. Lin, C. Wang, A chitosan-glutathione based injectable hydrogel for suppression of oxidative stress damage in cardiomyocytes, Biomaterials. (2013) 9071-9081.

[84] D.G. Rocca, B.J. Willenberg, Y. Qi, C.S. Simmons, A. Rubiano, L.F. Ferreira, T. Huo, J.W. Petersen, P.J. Ruchaya, P.S. Wate, E.A. Wise, E.M. Handberg, C.R. Cogle, C.D. Batich, B.J. Byrne, C.J. Pepine, An injectable capillary-like microstructured alginate hydrogel improves left ventricular function after myocardial infarction in rats, Int. J. Cardiol. (2016) 149-154.

[85] B.N. Brown, J.E. Valentin, A.M. Stewart-Akers, G.P. McCabe, S.F. Badylak, Macrophage phenotype and remodeling outcomes in response to biologic scaffolds with and without a cellular component, Biomaterials. (2009) 1482-1491.

[86] T.D. Johnson, J.A. Dequach, R. Gaetani, J. Ungerleider, D. Elhag, V. Nigam, A. Behfar, K.L. Christman, Human versus porcine tissue sourcing for an injectable myocardial matrix hydrogel, Biomater. Sci. (2014) 735-744.

[87] M.M. Nguyen, A.S. Carlini, M.P. Chien, S. Sonnenberg, C. Luo, R.L. Braden, K.G. Osborn, Y. Li, N.C. Gianneschi, K.L. Christman, Enzyme-Responsive Nanoparticles for Targeted Accumulation and Prolonged Retention in Heart Tissue after Myocardial Infarction, Adv. Mater. (2015) 5547-5552.

[88] L.E. Paulis, T. Geelen, M.T. Kuhlmann, B.F. Coolen, M. Schafers, K. Nicolay, G.J. Strijkers, Distribution of lipid-based nanoparticles to infarcted myocardium with potential application for MRI-monitored drug delivery, J. Control. Release. (2012) 276-285.

[89] D.J. Lundy, K.H. Chen, E.K. Toh, P.C. Hsieh, Distribution of Systemically Administered Nanoparticles Reveals a Size-Dependent Effect Immediately following Cardiac Ischaemia-Reperfusion Injury, Sci. Rep. (2016) 25613.

[90] C. Yao, X. Shi, X. Lin, L. Shen, D. Xu, Y. Feng, Increased cardiac distribution of mono-PEGylated Radix Ophiopogonis polysaccharide in both myocardial infarction and ischemia/reperfusion rats, Int. J. Nanomedicine. (2015) 409-418.

[91] T. Dvir, M. Bauer, A. Schroeder, J.H. Tsui, D.G. Anderson, R. Langer, R. Liao, D.S. Kohane, Nanoparticles targeting the infarcted heart, Nano Lett. (2011) 4411-4414.

[92] C.B. Rodell, J.W. MacArthur, S.M. Dorsey, R.J. Wade, L.L. Wang, Y.J. Woo, J.A. Burdick, Shear-Thinning Supramolecular Hydrogels with Secondary Autonomous Covalent Crosslinking to Modulate Viscoelastic Properties In Vivo, Adv. Funct. Mater. (2015) 636-644.

[93] G. Xu, X. Wang, C. Deng, X. Teng, E.J. Suuronen, Z. Shen, Z. Zhong, Injectable biodegradable hybrid hydrogels based on thiolated collagen and oligo(acryloyl carbonate)-poly(ethylene glycol)-oligo(acryloyl carbonate) copolymer for functional cardiac regeneration, Acta Biomater. (2015) 55-64.

[94] X. Bai, R. Fang, S. Zhang, X. Shi, Z. Wang, X. Chen, J. Yang, X. Hou, Y. Nie, Y. Li, W. Tian, Self-cross-linkable hydrogels composed of partially oxidized alginate and gelatin for myocardial infarction repair, J. Bioact. Compatible Polym. (2013) 126-140.

[95] C.B. Rodell, A.L. Kaminski, J.A. Burdick, Rational design of network properties in guest-host assembled and shear-thinning hyaluronic acid hydrogels, Biomacromolecules. (2013) 4125-4134.

[96] A.C. Gaffey, M.H. Chen, C.M. Venkataraman, A. Trubelja, C.B. Rodell, P.V. Dinh, G. Hung, J.W. MacArthur, R.V. Soopan, J.A. Burdick, P. Atluri, Injectable shear-thinning hydrogels used to deliver endothelial progenitor cells, enhance cell engraftment, and improve ischemic myocardium, J. Thorac. Cardiovasc. Surg. (2015) 1268-1276.

[97] S. Ren, X. Jiang, Z. Li, Y. Wen, D. Chen, X. Li, X. Zhang, R. Zhuo, H. Chu, Physical Properties of Poly(N-isopropylacrylamide) Hydrog el Promote its Effects on Cardiac Protection after Myocardial Infarction, J. Int. Med. Res. (2012) 2167-2182.

[98] Y. Zhu, H. Jiang, S.-H. Ye, T. Yoshizumi, W.R. Wagner, Tailoring the degradation rates of thermally responsive hydrogels designed for soft tissue injection by varying the autocatalytic potential, Biomaterials. (2015) 484-493.

[99] D.M. Nelson, R. Hashizume, T. Yoshizumi, A.K. Blakney, Z. Ma, W.R. Wagner, Intramyocardial injection of a synthetic hydrogel with delivery of bFGF and IGF1 in a rat model of ischemic cardiomyopathy, Biomacromolecules. (2014) 1-11.

[100] J.L. Ifkovits, E. Tous, M. Minakawa, M. Morita, J.D. Robb, K.J. Koomalsingh, J.H. Gorman, 3rd, R.C. Gorman, J.A. Burdick, Injectable hydrogel properties influence infarct expansion and extent of postinfarction left ventricular remodeling in an ovine model, Proc. Natl. Acad. Sci. U. S. A. (2010) 11507-11512.

[101] C. Williams, E. Budina, W.L. Stoppel, K.E. Sullivan, S. Emani, S.M. Emani, L.D. Black, 3rd, Cardiac extracellular matrix-fibrin hybrid scaffolds with tunable properties for cardiovascular tissue engineering, Acta Biomater. (2015) 84-95.

[102] J.M. Singelyn, K.L. Christman, Modulation of Material Properties of a Decellularized Myocardial Matrix Scaffold, Macromol. Biosci. (2011) 731-738.

[103] J.R. Pinney, K.T. Du, P. Ayala, Q. Fang, R.E. Sievers, P. Chew, L. Delrosario, R.J. Lee, T.A. Desai, Discrete microstructural cues for the attenuation of fibrosis following myocardial infarction, Biomaterials. (2014) 8820-8828.

[104] M.Y. Chang, Y.J. Yang, C.H. Chang, A.C. Tang, W.Y. Liao, F.Y. Cheng, C.S. Yeh, J.J. Lai, P.S. Stayton, P.C. Hsieh, Functionalized nanoparticles provide early cardioprotection after acute myocardial infarction, J. Control. Release. (2013) 287-294.

[105] Y. Zhu, N.A. Wood, K. Fok, T. Yoshizumi, D.W. Park, H. Jiang, D.S. Schwartzman, M.A. Zenati, T. Uchibori, W.R. Wagner, C.N. Riviere, Design of a Coupled Thermoresponsive Hydrogel and Robotic System for Postinfarct Biomaterial Injection Therapy, Ann. Thorac. Surg. (2016) 780-786.

[106] H. Hwang, J. Kwon, P.S. Oh, T.K. Lee, K.S. Na, C.M. Lee, H.S. Jeong, S.T. Lim, M.H. Sohn, H.J. Jeong, Peptide-loaded nanoparticles and radionuclide imaging for individualized treatment of myocardial ischemia, Radiology. (2014) 160-167.

[107] D. Danila, E. Johnson, P. Kee, CT imaging of myocardial scars with collagen-targeting gold nanoparticles, Nanomed. Nanotechnol. Biol. Med. 1067-1076.

[108] A. Taruttis, V. Ntziachristos, Advances in real-time multispectral optoacoustic imaging and its applications, Nature Photonics. (2015) 219-227.

[109] D.W. Park, S.H. Ye, H.B. Jiang, D. Dutta, K. Nonaka, W.R. Wagner, K. Kim, In vivo monitoring of structural and mechanical changes of tissue scaffolds by multi-modality imaging, Biomaterials. (2014) 7851-7859.

[110] A.A. Appel, M.A. Anastasio, J.C. Larson, E.M. Brey, Imaging challenges in biomaterials and tissue engineering, Biomaterials. (2013) 6615-6630.

[111] S.M. Dorsey, M. Haris, A. Singh, W.R.T. Witschey, C.B. Rodell, F. Kogan, R. Reddy, J.A. Burdick, Visualization of Injectable Hydrogels Using Chemical Exchange Saturation Transfer MRI, ACS Biomater. Sci. Eng. (2015) 227-237.

[112] M.S. Slaughter, K.G. Soucy, R.G. Matheny, B.C. Lewis, M.F. Hennick, Y. Choi, G. Monreal, M.A. Sobieski, G.A. Giridharan, S.C. Koenig, Development of an extracellular matrix delivery system for effective intramyocardial injection in ischemic tissue, ASAIO J. (2014) 730-736.

[113] Z. Ma, D.M. Nelson, Y. Hong, W.R. Wagner, Thermally responsive injectable hydrogel incorporating methacrylate-polylactide for hydrolytic lability, Biomacromolecules. (2010) 1873-1881.

[114] K.L. Fujimoto, Z. Ma, D.M. Nelson, R. Hashizume, J. Guan, K. Tobita, W.R. Wagner, Synthesis, characterization and therapeutic efficacy of a biodegradable, thermoresponsive hydrogel designed for application in chronic infarcted myocardium, Biomaterials. (2009) 4357-4368.

[115] H.K. Awada, N.R. Johnson, Y. Wang, Sequential delivery of angiogenic growth factors improves revascularization and heart function after myocardial infarction, J. Control. Release. (2015) 7-17.

[116] H.K. Awada, M.P. Hwang, Y. Wang, Towards comprehensive cardiac repair and regeneration after myocardial infarction: Aspects to consider and proteins to deliver, Biomaterials. (2016) 94-112.

[117] E.M. Sussman, M.C. Halpin, J. Muster, R.T. Moon, B.D. Ratner, Porous implants modulate healing and induce shifts in local macrophage polarization in the foreign body reaction, Ann. Biomed. Eng. (2014) 1508-1516.

[118] J.M. Anderson, A. Rodriguez, D.T. Chang, Foreign body reaction to biomaterials, Semin. Immunol. (2008) 86-100.

[119] A.J. Vegas, O. Veiseh, J.C. Doloff, M. Ma, H.H. Tam, K. Bratlie, J. Li, A.R. Bader, E. Langan, K. Olejnik, P. Fenton, J.W. Kang, J. Hollister-Locke, M.A. Bochenek, A. Chiu, S. Siebert, K. Tang, S. Jhunjhunwala, S. Aresta-Dasilva, N. Dholakia, R. Thakrar, T. Vietti, M. Chen, J. Cohen, K. Siniakowicz, M. Qi, J. McGarrigle, S. Lyle, D.M. Harlan, D.L. Greiner, J. Oberholzer, G.C. Weir, R. Langer, D.G. Anderson, Combinatorial hydrogel library enables identification of materials that mitigate the foreign body response in primates, Nat. Biotechnol. (2016) 345-352.

[120] L.S. Nair, C.T. Laurencin, Biodegradable polymers as biomaterials, Prog. Polym. Sci. (2007) 762-798.

[121] M.P. Staiger, A.M. Pietak, J. Huadmai, G. Dias, Magnesium and its alloys as orthopedic biomaterials: a review, Biomaterials. (2006) 1728-1734.

[122] F. Brandl, F. Sommer, A. Goepferich, Rational design of hydrogels for tissue engineering: impact of physical factors on cell behavior, Biomaterials. (2007) 134-146.

[123] H.J. Moon, Y. Ko du, M.H. Park, M.K. Joo, B. Jeong, Temperature-responsive compounds as in situ gelling biomedical materials, Chem. Soc. Rev. (2012) 4860-4883.

[124] N.A. Peppas, P. Bures, W. Leobandung, H. Ichikawa, Hydrogels in pharmaceutical formulations, Eur. J. Pharm. Biopharm. (2000) 27-46.

[125] C.M. Kirschner, K.S. Anseth, Hydrogels in healthcare: From static to dynamic material microenvironments, Acta Mater. (2013) 931-944.

[126] C. He, S.W. Kim, D.S. Lee, In situ gelling stimuli-sensitive block copolymer hydrogels for drug delivery, J. Control. Release. (2008) 189-207.

[127] M.K. Joo, M.H. Park, B.G. Choi, B. Jeong, Reverse thermogelling biodegradable polymer aqueous solutions, J. Mater. Chem. (2009) 5891.

[128] B.V. Slaughter, S.S. Khurshid, O.Z. Fisher, A. Khademhosseini, N.A. Peppas, Hydrogels in regenerative medicine, Adv. Mater. (2009) 3307-3329.

[129] B.S. Zolnik, D.J. Burgess, Effect of acidic pH on PLGA microsphere degradation and release, J. Control. Release. (2007) 338-344.

[130] J. Siepmann, K. Elkharraz, F. Siepmann, D. Klose, How autocatalysis accelerates drug release from PLGA-based microparticles: A quantitative treatment, Biomacromolecules. (2005) 2312-2319.

[131] K. Fu, D.W. Pack, A.M. Klibanov, R. Langer, Visual evidence of acidic environment within degrading poly(lactic-co-glycolic acid) (PLGA) microspheres, Pharm. Res. (2000) 100-106.

[132] L. Lu, C.A. Garcia, A.G. Mikos, In vitro degradation of thin poly(DL-lactic-co-glycolic acid) films, J. Biomed. Mater. Res. (1999) 236-244.

[133] C. Gong, S. Shi, P. Dong, B. Kan, M. Gou, X. Wang, X. Li, F. Luo, X. Zhao, Y. Wei, Z. Qian, Synthesis and characterization of PEG-PCL-PEG thermosensitive hydrogel, Int. J. Pharm. (2009) 89-99.

[134] C. Gong, S. Shi, L. Wu, M. Gou, Q. Yin, Q. Guo, P. Dong, F. Zhang, F. Luo, X. Zhao, Y. Wei, Z. Qian, Biodegradable in situ gel-forming controlled drug delivery system based on

thermosensitive PCL-PEG-PCL hydrogel. Part 2: sol-gel-sol transition and drug delivery behavior, Acta Biomater. (2009) 3358-3370.

[135] T. Potta, C. Chun, S.-C. Song, Controlling the degradation rate of thermoresponsive photo-cross-linked poly(organophosphazene) hydrogels with compositions of depsipeptide and PEG chain lengths, Polym. Degradation Stab. (2011) 1261-1270.

[136] Z. Cui, B.H. Lee, C. Pauken, B.L. Vernon, Manipulating degradation time in a N-isopropylacrylamide-based co-polymer with hydrolysis-dependent LCST, J. Biomater. Sci. Polym. Ed. (2010) 913-926.

[137] D.J. Overstreet, H.D. Dhruv, B.L. Vernon, Bioresponsive copolymers of poly(N-isopropylacrylamide) with enzyme-dependent lower critical solution temperatures, Biomacromolecules. (2010) 1154-1159.

[138] Y. Kumashiro, T. Ooya, N. Yui, Dextran Hydrogels Containing Poly(N-isopropylacrylamide) as Grafts and Cross-Linkers Exhibiting Enzymatic Regulation in a Specific Temperature Range, Macromol. Rapid Commun. (2004) 867-872.

[139] S. Kim, K.E. Healy, Synthesis and characterization of injectable poly(N-isopropylacrylamide-co-acrylic acid) hydrogels with proteolytically degradable cross-links, Biomacromolecules. (2003) 1214-1223.

[140] B.H. Lee, B.L. Vernon, In situ-gelling, erodible N-isopropylacrylamide copolymers, Macromol. Biosci. (2005) 629-635.

[141] B.H. Lee, B. Vernon, Copolymers of N-isopropylacrylamide, HEMA-lactate and acrylic acid with time-dependent lower critical solution temperature as a bioresorbable carrier, Polym. Int. (2005) 418-422.

[142] S.K. Vakkalanka, N.A. Peppas, Swelling behavior of temperature- and pH-sensitive block terpolymers for drug delivery, Polym. Bull. (1996) 221-225.

[143] C.S. Brazel, N.A. Peppas, Synthesis and Characterization of Thermomechanically and Chemomechanically Responsive Poly(N-Isopropylacrylamide-Co-Methacrylic Acid) Hydrogels, Macromolecules. (1995) 8016-8020.

[144] J. Zhang, N.A. Peppas, Synthesis and characterization of pH- and temperature-sensitive poly(methacrylic acid)/poly(N-isopropylacrylamide) interpenetrating polymeric networks, Macromolecules. (2000) 102-107.

[145] R. Sjöback, J. Nygren, M. Kubista, Absorption and fluorescence properties of fluorescein, Spectrochimica Acta Part A: Molecular and Biomolecular Spectroscopy. (1995) L7-L21.

[146] M. Ara, M. Watanabe, Y. Imai, Effect of blending calcium compounds on hydrolytic degradation of poly(DL-lactic acid-co-glycolic acid), Biomaterials. (2002) 2479-2483.

[147] Y. Zhang, S. Zale, L. Sawyer, H. Bernstein, Effects of metal salts on poly(DL-lactide-co-glycolide) polymer hydrolysis, J. Biomed. Mater. Res. (1997) 531-538.

[148] L. Wu, J. Ding, Effects of porosity and pore size on in vitro degradation of three-dimensional porous poly(D,L-lactide-co-glycolide) scaffolds for tissue engineering, J. Biomed. Mater. Res. A. (2005) 767-777.

[149] A.N. Ford Versypt, D.W. Pack, R.D. Braatz, Mathematical modeling of drug delivery from autocatalytically degradable PLGA microspheres--a review, J. Control. Release. (2013) 29-37.

[150] G.L. Siparsky, K.J. Voorhees, F.D. Miao, Hydrolysis of polylactic acid (PLA) and polycaprolactone (PCL) in aqueous acetonitrile solutions: Autocatalysis, J. Environ. Polymer Degradation. (1998) 31-41.

[151] H. Antheunis, J.C. van der Meer, M. de Geus, A. Heise, C.E. Koning, Autocatalytic equation describing the change in molecular weight during hydrolytic degradation of aliphatic polyesters, Biomacromolecules. (2010) 1118-1124.

[152] N. Safaei Nikouei, A. Lavasanifar, Characterization of the thermo- and pH-responsive assembly of triblock copolymers based on poly(ethylene glycol) and functionalized poly(epsilon-caprolactone), Acta Biomater. (2011) 3708-3718.

[153] X.J. Loh, S.H. Goh, J. Li, Hydrolytic degradation and protein release studies of thermogelling polyurethane copolymers consisting of poly[(R)-3-hydroxybutyrate], poly(ethylene glycol), and poly(propylene glycol), Biomaterials. (2007) 4113-4123.

[154] L. Yu, G.T. Chang, H. Zhang, J.D. Ding, Injectable block copolymer hydrogels for sustained release of a PEGylated drug, Int. J. Pharm. (2008) 95-106.

[155] M.H. Park, M.K. Joo, B.G. Choi, B. Jeong, Biodegradable Thermogels, Acc. Chem. Res. (2011) 424-433.

[156] F. Wang, Z. Li, M. Khan, K. Tamama, P. Kuppusamy, W.R. Wagner, C.K. Sen, J. Guan, Injectable, rapid gelling and highly flexible hydrogel composites as growth factor and cell carriers, Acta Biomater. (2010) 1978-1991.

[157] Z. Li, F. Wang, S. Roy, C.K. Sen, J. Guan, Injectable, highly flexible, and thermosensitive hydrogels capable of delivering superoxide dismutase, Biomacromolecules. (2009) 3306-3316.

[158] A. Galperin, T.J. Long, B.D. Ratner, Degradable, thermo-sensitive poly(N-isopropyl acrylamide)-based scaffolds with controlled porosity for tissue engineering applications, Biomacromolecules. (2010) 2583-2592.

[159] J. Patterson, J.A. Hubbell, Enhanced proteolytic degradation of molecularly engineered PEG hydrogels in response to MMP-1 and MMP-2, Biomaterials. (2010) 7836-7845.

[160] Y. Qiu, J.J. Lim, L. Scott, Jr., R.C. Adams, H.T. Bui, J.S. Temenoff, PEG-based hydrogels with tunable degradation characteristics to control delivery of marrow stromal cells for tendon overuse injuries, Acta Biomater. (2011) 959-966.

[161] S. Kim, E.H. Chung, M. Gilbert, K.E. Healy, Synthetic MMP-13 degradable ECMs based on poly(N-isopropylacrylamide-co-acrylic acid) semi-interpenetrating polymer networks. I. Degradation and cell migration, J. Biomed. Mater. Res. A. (2005) 73-88.

[162] A.M. Kloxin, A.M. Kasko, C.N. Salinas, K.S. Anseth, Photodegradable hydrogels for dynamic tuning of physical and chemical properties, Science. (2009) 59-63.

[163] J.L. Holloway, H. Ma, R. Rai, J.A. Burdick, Modulating hydrogel crosslink density and degradation to control bone morphogenetic protein delivery and in vivo bone formation, J. Control. Release. (2014) 63-70.

[164] V. Sacchi, R. Mittermayr, J. Hartinger, M.M. Martino, K.M. Lorentz, S. Wolbank, A. Hofmann, R.A. Largo, J.S. Marschall, E. Groppa, R. Gianni-Barrera, M. Ehrbar, J.A. Hubbell, H. Redl, A. Banfi, Long-lasting fibrin matrices ensure stable and functional angiogenesis by highly tunable, sustained delivery of recombinant VEGF(164), Proc. Natl. Acad. Sci. U. S. A. (2014) 6952-6957.

[165] J. Leor, S. Tuvia, V. Guetta, F. Manczur, D. Castel, U. Willenz, Ö. Petneházy, N. Landa, M.S. Feinberg, E. Konen, O. Goitein, O. Tsur-Gang, M. Shaul, L. Klapper, S. Cohen, Intracoronary Injection of In Situ Forming Alginate Hydrogel Reverses Left Ventricular Remodeling After Myocardial Infarction in Swine, J. Am. Coll. Cardiol. (2009) 1014-1023.

[166] T. Ota, N.A. Patronik, D. Schwartzman, C.N. Riviere, M.A. Zenati, Minimally invasive epicardial injections using a novel semiautonomous robotic device, Circulation. (2008) S115-S120.

[167] N.A. Patronik, T. Ota, M.A. Zenati, C.N. Riviere, A Miniature Mobile Robot for Navigation and Positioning on the Beating Heart, IEEE Trans Robot. (2009) 1109-1124.

[168] H. Hartshorne, J.R. Reynolds, A System of medicine, H.C. Lea's Son & Co., Philadelphia, 1880.

[169] J.F. Wenk, S.T. Wall, R.C. Peterson, S.L. Helgerson, H.N. Sabbah, M. Burger, N. Stander, M.B. Ratcliffe, J.M. Guccione, A method for automatically optimizing medical devices for treating heart failure: designing polymeric injection patterns, J. Biomech. Eng. (2009) 121011.

[170] G.M. Fomovsky, J.R. Macadangdang, G. Ailawadi, J.W. Holmes, Model-based design of mechanical therapies for myocardial infarction, J. Cardiovasc. Transl. Res. (2011) 82-91.

[171] N.A. Patronik, A miniature mobile robot for precise and stable access to the beating heart, Carnegie Mellon University, 2008.

[172] J.M. Singelyn, P. Sundaramurthy, T.D. Johnson, P.J. Schup-Magoffin, D.P. Hu, D.M. Faulk, J. Wang, K.M. Mayle, K. Bartels, M. Salvatore, A.M. Kinsey, A.N. Demaria, N. Dib, K.L. Christman, Catheter-deliverable hydrogel derived from decellularized ventricular extracellular matrix increases endogenous cardiomyocytes and preserves cardiac function post-myocardial infarction, J. Am. Coll. Cardiol. (2012) 751-763.

[173] H. Tsutsui, S. Kinugawa, S. Matsushima, Oxidative stress and heart failure, American Journal of Physiology - Heart and Circulatory Physiology. (2011) H2181.

[174] V. Braunersreuther, V. Jaquet, Reactive oxygen species in myocardial reperfusion injury: from physiopathology to therapeutic approaches, Curr. Pharm. Biotechnol. (2012) 97-114.

[175] Y. Sun, Oxidative stress and cardiac repair/remodeling following infarction, Am. J. Med. Sci. (2007) 197-205.

[176] R. von Harsdorf, P.F. Li, R. Dietz, Signaling pathways in reactive oxygen species-induced cardiomyocyte apoptosis, Circulation. (1999) 2934-2941.

[177] W.D. Johnson, K.L. Kayser, J.B. Brenowitz, S.F. Saedi, A randomized controlled trial of allopurinol in coronary bypass surgery, Am. Heart J. (1991) 20-24.

[178] H. Dingchao, Q. Zhiduan, H. Liye, F. Xiaodong, The Protective Effects of High-Dose Ascorbic Acid on Myocardium against Reperfusion Injury During and After Cardiopulmonary Bypass, Thorac. Cardiovasc. Surg. (1994) 276-278.

[179] J. Sochman, J. Vrbska, B. Musilova, M. Rocek, Infarct Size Limitation: acute N-acetylcysteine defense (ISLAND trial): preliminary analysis and report after the first 30 patients, Clin. Cardiol. (1996) 94-100.

[180] D. Yesilbursa, A. Serdar, T. Senturk, Z. Serdar, S. Sag, J. Cordan, Effect of N-acetylcysteine on oxidative stress and ventricular function in patients with myocardial infarction, Heart Vessels. (2006) 33-37.

[181] W. Guan, T. Osanai, T. Kamada, H. Hanada, H. Ishizaka, H. Onodera, A. Iwasa, N. Fujita, S. Kudo, T. Ohkubo, K. Okumura, Effect of allopurinol pretreatment on free radical generation after primary coronary angioplasty for acute myocardial infarction, J. Cardiovasc. Pharmacol. (2003) 699-705.

[182] J.T. Flaherty, B. Pitt, J.W. Gruber, R.R. Heuser, D.A. Rothbaum, L.R. Burwell, B.S. George, D.J. Kereiakes, D. Deitchman, N. Gustafson, et al., Recombinant human superoxide dismutase (h-SOD) fails to improve recovery of ventricular function in patients undergoing coronary angioplasty for acute myocardial infarction, Circulation. (1994) 1982-1991.

[183] D.P. Taggart, V. Young, J. Hooper, M. Kemp, R. Walesby, P. Magee, J.E. Wright, Lack of cardioprotective efficacy of allopurinol in coronary artery surgery, Br. Heart J. (1994) 177-181.

[184] A. Lassnigg, A. Punz, R. Barker, P. Keznickl, N. Manhart, E. Roth, M. Hiesmayr, Influence of intravenous vitamin E supplementation in cardiac surgery on oxidative stress: a double-blinded, randomized, controlled study, Br. J. Anaesth. (2003) 148-154.

[185] A. Coetzee, G. Roussouw, L. Macgregor, Failure of allopurinol to improve left ventricular stroke work after cardiopulmonary bypass surgery, J. Cardiothorac. Vasc. Anesth. (1996) 627-633.

[186] O. Peker, T. Peker, D. Erdogan, M. Ozaydin, S. Kapan, R. Sutcu, E. Ibrisim, Effects of intravenous N-acetylcysteine on periprocedural myocardial injury after on-pump coronary artery by-pass grafting, J. Cardiovasc. Surg. (Torino). (2008) 527-531.

[187] J. Westhuyzen, A.D. Cochrane, P.J. Tesar, T. Mau, D.B. Cross, M.P. Frenneaux, F.A. Khafagi, S.J. Fleming, Effect of preoperative supplementation with alpha-tocopherol and ascorbic acid on myocardial injury in patients undergoing cardiac operations, J. Thorac. Cardiovasc. Surg. (1997) 942-948.

[188] I. El-Hamamsy, L.M. Stevens, M. Carrier, M. Pellerin, D. Bouchard, P. Demers, R. Cartier, P. Page, L.P. Perrault, Effect of intravenous N-acetylcysteine on outcomes after coronary artery bypass surgery: a randomized, double-blind, placebo-controlled clinical trial, J. Thorac. Cardiovasc. Surg. (2007) 7-12.

[189] M. Heras, A. Chamorro, Atherosclerosis: a systemic condition that requires a global approach, Eur. Heart J. (2000) 872-873.

[190] T.L.t. Lynch, M. Sivaguru, M. Velayutham, A.J. Cardounel, M. Michels, D. Barefield, S. Govindan, C. dos Remedios, J. van der Velden, S. Sadayappan, Oxidative Stress in Dilated Cardiomyopathy Caused by MYBPC3 Mutation, Oxid. Med. Cell. Longev. (2015) 424751.

[191] E. Martinez-Sanz, D.A. Ossipov, J. Hilborn, S. Larsson, K.B. Jonsson, O.P. Varghese, Bone reservoir: Injectable hyaluronic acid hydrogel for minimal invasive bone augmentation, J. Control. Release. (2011) 232-240.

[192] D.R. Griffin, W.M. Weaver, P.O. Scumpia, D. Di Carlo, T. Segura, Accelerated wound healing by injectable microporous gel scaffolds assembled from annealed building blocks, Nat Mater. (2015) 737-744.

[193] J. Alijotas-Reig, M.T. Fernandez-Figueras, L. Puig, Late-onset inflammatory adverse reactions related to soft tissue filler injections, Clin. Rev. Allergy Immunol. (2013) 97-108.

[194] R.V. Ulijn, N. Bibi, V. Jayawarna, P.D. Thornton, S.J. Todd, R.J. Mart, A.M. Smith, J.E. Gough, Bioresponsive hydrogels, Mater. Today. (2007) 40-48.

[195] J. Zhu, R.E. Marchant, Design properties of hydrogel tissue-engineering scaffolds, Expert Rev. Med. Devices. (2011) 607-626.

[196] N. Annabi, A. Tamayol, J.A. Uquillas, M. Akbari, L.E. Bertassoni, C. Cha, G. Camci-Unal, M.R. Dokmeci, N.A. Peppas, A. Khademhosseini, 25th Anniversary Article: Rational

Design and Applications of Hydrogels in Regenerative Medicine, Adv. Mater. (2014) 85-124.

[197] S.A. Bencherif, R.W. Sands, D. Bhatta, P. Arany, C.S. Verbeke, D.A. Edwards, D.J. Mooney, Injectable preformed scaffolds with shape-memory properties, Proc. Natl. Acad. Sci. U. S. A. (2012) 19590-19595.

[198] L. Zhang, Z. Cao, T. Bai, L. Carr, J.R. Ella-Menye, C. Irvin, B.D. Ratner, S. Jiang, Zwitterionic hydrogels implanted in mice resist the foreign-body reaction, Nat. Biotechnol. (2013) 553-556.

[199] G. Broughton, II, J.E. Janis, C.E. Attinger, The Basic Science of Wound Healing, Plast. Reconstr. Surg. (2006).

[200] L. Tang, T.A. Jennings, J.W. Eaton, Mast cells mediate acute inflammatory responses to implanted biomaterials, Proc. Natl. Acad. Sci. U. S. A. (1998) 8841-8846.

[201] N.P. Rhodes, J.A. Hunt, D.F. Williams, Macrophage subpopulation differentiation by stimulation with biomaterials, J. Biomed. Mater. Res. (1997) 481-488.

[202] I.F. Charo, R.M. Ransohoff, The Many Roles of Chemokines and Chemokine Receptors in Inflammation, New Engl. J. Med. (2006) 610-621.

[203] K. Smetana, J. Vacík, D. Součková, Z. Krčová, J. Šulc, The influence of hydrogel functional groups on cell behavior, J. Biomed. Mater. Res. (1990) 463-470.

[204] P.M. Henson, The immunologic release of constituents from neutrophil leukocytes. I. The role of antibody and complement on nonphagocytosable surfaces or phagocytosable particles, J. Immunol. (1971) 1535-1546.

[205] P.M. Henson, The immunologic release of constituents from neutrophil leukocytes. II. Mechanisms of release during phagocytosis, and adherence to nonphagocytosable surfaces, J. Immunol. (1971) 1547-1557.

[206] F. Nagatoshi, K. Kazuo, Macrophages in Inflammation, Current Drug Target - Inflammation & Allergy. (2005) 281-286.

[207] R. Sridharan, A.R. Cameron, D.J. Kelly, C.J. Kearney, F.J. O'Brien, Biomaterial based modulation of macrophage polarization: a review and suggested design principles, Mater. Today. (2015) 313-325.

[208] D.O. Freytes, J. Martin, S.S. Velankar, A.S. Lee, S.F. Badylak, Preparation and rheological characterization of a gel form of the porcine urinary bladder matrix, Biomaterials. (2008) 1630-1637.

[209] L. Huleihel, G.S. Hussey, J.D. Naranjo, L. Zhang, J.L. Dziki, N.J. Turner, D.B. Stolz, S.F. Badylak, Matrix-bound nanovesicles within ECM bioscaffolds, Science Advances. (2016).

[210] B.M. Sicari, J.L. Dziki, B.F. Siu, C.J. Medberry, C.L. Dearth, S.F. Badylak, The promotion of a constructive macrophage phenotype by solubilized extracellular matrix, Biomaterials. (2014) 8605-8612.

[211] T. Garg, A.K. Goyal, Biomaterial-based scaffolds – current status and future directions, Expert Opinion on Drug Delivery. (2014) 767-789.

[212] Q.L. Loh, C. Choong, Three-dimensional scaffolds for tissue engineering applications: role of porosity and pore size, Tissue Eng Part B Rev. (2013) 485-502.

[213] F. Baino, S. Fiorilli, C. Vitale-Brovarone, Bioactive glass-based materials with hierarchical porosity for medical applications: Review of recent advances, Acta Biomater. (2016) 18-32.

[214] S.T. Koshy, T.C. Ferrante, S.A. Lewin, D.J. Mooney, Injectable, porous, and cell-responsive gelatin cryogels, Biomaterials. (2013).

[215] C.S. Verbeke, D.J. Mooney, Injectable, Pore-Forming Hydrogels for In Vivo Enrichment of Immature Dendritic Cells, Adv. Healthc. Mater. (2015) 2677-2687.

[216] J.A. Kim, J. Lim, R. Naren, H.S. Yun, E.K. Park, Effect of the biodegradation rate controlled by pore structures in magnesium phosphate ceramic scaffolds on bone tissue regeneration in vivo, Acta Biomater. (2016) 155-167.

[217] H. Janik, M. Marzec, A review: fabrication of porous polyurethane scaffolds, Mater. Sci. Eng. C Mater. Biol. Appl. (2015) 586-591.

[218] W.L. Murphy, R.G. Dennis, J.L. Kileny, D.J. Mooney, Salt fusion: An approach to improve pore interconnectivity within tissue engineering scaffolds, Tissue Eng. (2002) 43-52.

[219] Q. Hou, D.W. Grijpma, J. Feijen, Porous polymeric structures for tissue engineering prepared by a coagulation, compression moulding and salt leaching technique, Biomaterials. (2003) 1937-1947.

[220] I.T. Swinehart, S.F. Badylak, Extracellular matrix bioscaffolds in tissue remodeling and morphogenesis, Dev. Dyn. (2016) 351-360.

[221] B.N. Brown, R. Londono, S. Tottey, L. Zhang, K.A. Kukla, M.T. Wolf, K.A. Daly, J.E. Reing, S.F. Badylak, Macrophage phenotype as a predictor of constructive remodeling following the implantation of biologically derived surgical mesh materials, Acta Biomater. (2012) 978-987.

[222] D. Hachim, S.T. LoPresti, C.C. Yates, B.N. Brown, Shifts in macrophage phenotype at the biomaterial interface via IL-4 eluting coatings are associated with improved implant integration, Biomaterials. (2017) 95-107.

[223] D.M. Mosser, J.P. Edwards, Exploring the full spectrum of macrophage activation, Nat. Rev. Immunol. (2008) 958-969.

[224] T. Lawrence, G. Natoli, Transcriptional regulation of macrophage polarization: enabling diversity with identity, Nat. Rev. Immunol. (2011) 750-761.

[225] S.K. Biswas, E. Lopez-Collazo, Endotoxin tolerance: new mechanisms, molecules and clinical significance, Trends Immunol. (2009) 475-487.

[226] A.K. Blakney, M.D. Swartzlander, S.J. Bryant, The effects of substrate stiffness on the in vitro activation of macrophages and in vivo host response to poly(ethylene glycol)-based hydrogels, J. Biomed. Mater. Res. A. (2012) 1375-1386.